8-2016

An Experimental Investigation of Self-Excited Combustion Dynamics in a Single Element Lean Direct Injection (LDI) Combustor

Rohan M. Gejji
Purdue University

Graduate School Form
30 Updated 12/26/2015

PURDUE UNIVERSITY
GRADUATE SCHOOL
Thesis/Dissertation Acceptance

This is to certify that the thesis/dissertation prepared

By ROHAN M. GEJJI

Entitled

AN EXPERIMENTAL INVESTIGATION OF SELF-EXCITED COMBUSTION DYNAMICS IN A SINGLE ELEMENT LEAN DIRECT INJECTION (LDI) COMBUSTOR

For the degree of Doctor of Philosophy

Is approved by the final examining committee:

Prof. William E. Anderson
Chair

Prof. Robert P. Lucht

Prof. Stephen D. Heister

Prof. Jay P. Gore

To the best of my knowledge and as understood by the student in the Thesis/Dissertation Agreement, Publication Delay, and Certification Disclaimer (Graduate School Form 32), this thesis/dissertation adheres to the provisions of Purdue University's "Policy of Integrity in Research" and the use of copyright material.

Approved by Major Professor(s): Prof. William E. Anderson

Approved by: Prof. Wayne Chen 7/26/2016

Head of the Departmental Graduate Program Date

AN EXPERIMENTAL INVESTIGATION OF SELF-EXCITED COMBUSTION DYNAMICS IN A SINGLE ELEMENT LEAN DIRECT INJECTION (LDI) COMBUSTOR

A Dissertation

Submitted to the Faculty

of

Purdue University

by

Rohan M. Gejji

In Partial Fulfillment of the

Requirements for the Degree

of

Doctor of Philosophy

August 2016

Purdue University

West Lafayette, Indiana

To my parents

ACKNOWLEDGEMENTS

First and foremost, I thank Prof. William Anderson for giving me the opportunity to be a part of his research group and research this project. His constant guidance, insight and inspiration have been instrumental to the research presented here as well as my overall growth over the last few years. I would also like to thank Prof. Robert Lucht, Prof. Stephen Heister, Prof. Jay Gore, and Prof. Hukam Mongia for serving on my advisory committee. Their wholehearted support and guidance during my time as a graduate student at Purdue University are greatly appreciated. I would also acknowledge the help and guidance provided by Prof. Sojka for the spray measurements carried out in his lab.

I would like to thank Scott Meyer for his continued support of all my research activities, from my very first days at the lab. His guidance has been instrumental to the researcher and engineer I am today. I am very grateful for the technical support and know-how of Robert McGuire with the design and fabrication of research hardware. I would also like to acknowledge BJ Austin of InSpace LLC, for his guidance on my recent foray into rocket combustion experiments.

I am extremely grateful to Dr. Cheng Huang and Dr. Changjin Yoon for the work on the computational portion of the project, which was pivotal to the completion of the work and to the understanding of the results presented here. I would especially like to thank Dr. Chris Fugger, Dr. Carson Slabaugh and Andrew Pratt for spending countless hours helping with

test activities at all times of day, night and sometimes both. Never a dull moment, I also acknowledge my colleagues at the Zucrow High Pressure Laboratory for their camaraderie: Mike Bedard, Andrei Anghelus, Dr. Anup Sane, Dr. Indraneel Sircar, Dr. Swanand Sardeshmukh, Dr. Warren Lamont, Dr. Pratikash Panda, Dr. Mario Roa, Bob Zhang, Timo Buschhagen, Heather Wiest, David Schulz, Brandon Kan, Tristan Fuller, Evan Maynard and the rest of the extended HPL past and present student community whom I have had a chance to work with.

Finally, I would be remiss to forget the support, encouragement and patience of my parents, my brother Varun and the rest of my family throughout this rewarding endeavor.

The financial support for the project from NASA Glenn Research Center through the NASA Research Announcement (NRA) Grant NNX11AI62A is acknowledged.

TABLE OF CONTENTS

Page

Page

Page

LIST OF TABLES

LIST OF FIGURES

Figure Page

Figure Page

Figure Page

Figure Page

Figure Page

Figure Page

Figure Page

NOMENCLATURE

LPP	Lean Premixed Prevaporized
LDI	Lean Direct Injection
RQL	Rich Quench Lean burn
PVC	Precessing Vortex Core
NOx	Oxides of nitrogen
UHC	Unburned Hydrocarbons
PM	Particulate Matter
PLIF	Planar Laser Induced Fluorescence
PIV	Particle Imaging Velocimetry
LES	Large Eddy Simulations
PMT	Photomultiplier Tube
VBB	Vortex Bubble Breakdown
FT	Fischer Tropsch synthesis
SPK	Synthetic Paraffinic Kerosene
LEE	Linearized Euler Equations
LBO	Lean Blowout
PSD	Power Spectral Density
PDA	Phase Doppler Anemometry
SMD, D_{32}	Sauter Mean Diameter
CTRZ	Central Toroidal Recirculation Zone
DMD	Dynamic Mode Decomposition
SNR	Signal to Noise Ratio
FSD	Flame Surface Density

ABSTRACT

Gejji, Rohan M., Ph.D., Purdue University, August 2016. An Experimental Investigation of Self-Excited Combustion Dynamics in a Single Element Lean Direct Injection (LDI) Combustor. Major Professor: William E. Anderson, School of Aeronautics and Astronautics.

The management of combustion dynamics in gas turbine combustors has become more challenging as strict NOx/CO emission standards have led to engine operation in a narrow, lean regime. While premixed or partially premixed combustor configurations such as the Lean Premixed Pre-vaporized (LPP), Rich Quench Lean burn (RQL), and Lean Direct Injection (LDI) have shown a potential for reduced NOx emissions, they promote a coupling between acoustics, hydrodynamics and combustion that can lead to combustion instabilities. These couplings can be quite complex, and their detailed understanding is a pre-requisite to any engine development program and for the development of predictive capability for combustion instabilities through high-fidelity models.

The overarching goal of this project is to assess the capability of high-fidelity simulation to predict combustion dynamics in low-emissions gas turbine combustors. A prototypical lean-direct-inject combustor was designed in a modular configuration so that a suitable geometry could be found by test. The combustor comprised a variable length air plenum and combustion chamber, air swirler, and fuel nozzle located inside a subsonic venturi. The venturi cross section and the fuel nozzle were consistent with previous studies.

Test pressure was 1 MPa and variables included geometry and acoustic resonance, inlet temperatures, equivalence ratio, and type of liquid fuel. High-frequency pressure measurements in a well-instrumented metal chamber yielded frequencies and mode shapes as a function of inlet air temperature, equivalence ratio, fuel nozzle placement, and combustor acoustic resonances. The parametric survey was a significant effort, with over 105 tests on eight geometric configurations. A good dataset was obtained that could be used for both operating-point-dependent quantitative comparisons, and testing the ability of the simulation to predict more global trends.

Results showed a very strong dependence of instability amplitude on the geometric configuration of the combustor, i.e., its acoustic resonance characteristics, with measured pressure fluctuation amplitudes ranged from 5 kPa (0.5% of mean pressure) to 200 kPa (~20% of mean pressure) depending on combustor geometry. The stability behavior also showed a consistent and pronounced dependence on equivalence ratio and inlet air temperature. Instability amplitude increased with higher equivalence ratio and with lower inlet air temperature. A pronounced effect of fuel nozzle location on the combustion dynamics was also observed. Combustion instabilities with the fuel nozzle at the throat of the venturi throat were stronger than in the configuration with fuel nozzle 2.6 mm upstream of the nozzle.

A second set of dynamics data was based on high-response-rate laser-based combustion diagnostics using an optically accessible combustor section. High-frequency measurements of OH*-chemiluminescence and OH-PLIF and velocity fields using PIV were obtained at a relatively stable, low equivalence ratio case and a less stable case at

higher ϕ. PIV measurements were performed at 5 kHz for non-reacting flow but glare from the cylindrical quartz chamber limited the field of view to a small region in the combustor.

Quantitative and qualitative comparisons were made for five different combinations of geometry and operating condition that yielded discriminating stability behavior in the experiment with simulations that were carried out concurrently. Comparisons were made on the basis of trends and pressure mode data as well as with OH-PLIF measurements for the baseline geometry at ϕ=0.44 and 0.6 equivalence ratios. Overall, the ability of the simulation to match experimental data and trends was encouraging. Dynamic Mode Decomposition (DMD) analysis was performed on two sets of computations - a global 2-step chemistry mechanism and an 18-step chemistry mechanism - and the OH-PLIF images to allow comparison of dynamic patterns of heat release and OH distribution in the combustion zone. The DMD analysis was able to identify similar dominant unstable modes in the combustor.

Recommendations for future work are based on the continued requirement for quantitative and spatio-temporally resolved data for direct comparison with computational efforts to develop predictive capabilities for combustion instabilities at relevant operating conditions. Discriminating instability behavior for the prototypical combustor demonstrated in this study is critical for any robust validation effort Unit physics based scaling of the current effort to multi-element combustors along with improvement in diagnostic techniques and analysis efforts are recommended for advancement in understanding of the complex physics in the multi-phase, three dimensional and turbulent combustion processes in the LDI combustor.

CHAPTER 1. INTRODUCTION

1.1 Motivation

The concurrent need to reduce the human impact on the environment and the predominant dependence on the combustion of hydrocarbon fuels to fulfill our energy needs has necessitated increased efficiency and reduced emissions from combustion devices. Civil aviation makes a relatively small, but increasing contribution to emissions including carbon dioxide (CO_2), carbon monoxide (CO), unburned hydrocarbons (UHCs), oxides of nitrogen ($NO_{x)}$, sulfur oxides (SO_x), particulate matter (PM) such as soot, ash, metal fumes, various aerosols as well as noise. The predicted annual growth of aviation of approximately 5% for the next 25 years with a four-fold increase in aviation fuel consumption by 2050 compared to 1992 has exerted immense pressure on gas turbine engine manufacturers to reduce emissions [1]. For aviation gas turbines, from a local air quality as well as global climate perspective, a significant focus has been placed on NO_x reduction technologies.

The primary NO_x in combustion systems is nitric oxide (NO) which is formed through the Zeldovich (thermal) and prompt combustion mechanisms. Thermal NO production is sensitive to temperature and is highest at temperatures in excess of 1800 K [2-4]. Prompt NO mechanism or the Fenimore mechanism [5, 6] is the dominant NO formation process

in the flame zone. Intermediate radical formation like HCN, CN or N_2O leads to the formation of NO. The NO yields through this mechanism have been shown to be favored near stoichiometric operating conditions where the flame temperatures are at their maximum. All low dry NOx technologies are hence aimed at operating at overall low equivalence ratios, thus reducing, both temporally and spatially, the existence of stoichiometric, high temperature zones in the combustor that promote NOx formation. Premixed and partially premixed configurations such as Lean Premixed Pre-vaporized (LPP), Rich Quench Lean burn (RQL), and Lean Direct Injection (LDI) techniques have shown great promise in this regard.

The success of dry low- NOx LPP and LDI techniques depend critically on the fuel-air vaporizing-mixing stage and the flame holding stage. Lean combustion tends to make these combustors susceptible to combustion instabilities induced by promoting coupling between acoustics, hydrodynamics and combustion. Combustion instabilities manifest in the combustor as strong pressure fluctuations and can affect an engine's life due to enhanced heat transfer, lower combustion efficiency, increase NOx emissions, generate noise pollution and lead to instrumentation and structural failures [7]. The current work is focused on the study of combustion instabilities in a single-element LDI combustor.

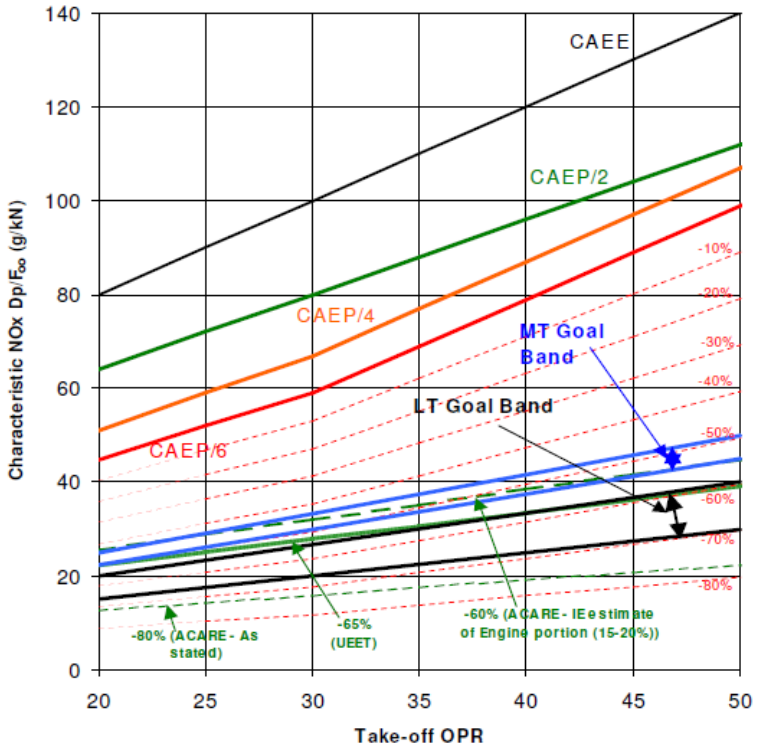

Figure 1.1. Mid-term and long-term emissions set by ICAO-CAEP. The overall reduction in characteristic NOx emission along with a ride in take-off operating pressure ratio (OPR) highlights the low-emission capabilities and reduction in flash-back events associated with high OPR. [1]

1.2 Combustion Instability

Lord Rayleigh [8] first stated the criterion for combustion instability while describing the maintenance of the vibration of heat in the following words:

"If heat be periodically communicated to, and abstracted from, a mass of air vibrating (for example) in a cylinder bounded by a piston, the effect produced will depend on the phase of the vibration at which the transfer of heat takes place. If heat be given to the air at the moment of greatest condensation, the vibration is encouraged. On the other hand, if heat

be given at the moment of greatest rarefaction, or abstracted at the moment of greatest condensation, the vibration is discouraged".

This is known as the Rayleigh criterion which governs the amplification or dampening of combustion instabilities through the constructive or destructive coupling between combustion chamber acoustics with heat release from the flame. It can be summarized in the following expression [9-11],

$$\int_V \int_T p'(x,t)q'(x,t)dtdV \geq \int_V \int_T \sum_i L_i(x,t)dtdV \qquad (1.1)$$

where, $p'(x,t)$, $q'(x,t)$, V, T, and L_i are chamber pressure fluctuations, heat release fluctuations, volume of the combustion chamber, the period of the oscillations, and the ith acoustic energy loss process which may include viscous dissipation and thermal losses from the chamber, respectively. When the pressure and heat release fluctuations are in phase, the instability is positively fed by the flame acoustic coupling. For most high-power turbulent flames, the pressure and heat release fluctuations are intimately tied to velocity fluctuations introduced by the dynamic flow processes including fuel injection, vortex shedding, and swirl. The relation for the sustenance of combustion instabilities is hence tied to not only the positive coupling between chamber acoustics and heat release, but its reinforcement by the velocity fluctuations at critical locations in the combustor.

Dry low NOx gas turbine combustors are designed to operate at lean operational regimes close to the lean blowout limits of the combustor. Under these conditions, chemical kinetics

and the flame location and surface is sensitive to even small changes in local equivalence ratio, fuel or air flow rate, fuel spray pattern and consequently its interaction with the chamber acoustics. This makes the combustor more susceptible to combustion instabilities. Presence of multiple subtle mechanisms that can interact or effect combustion instabilities in gas turbine combustor makes it challenging to identify root-cause physical mechanisms.

To further understanding of the root-cause physical mechanisms and to develop predictive capability of computational models, it is necessary to design and perform experiments that produce self-excited thermoacoustic oscillations and are amenable to high fidelity laser measurements of the inherently unstable, high turbulent flow-field in the combustor. The interplay between experimental measurements and numerical computations will accelerate modeling development by ensuring that the model simplifications and assumptions are based on solid physical foundations, making the computations predictive and robust.

1.3 Objectives

The overarching goal of this project is to assess the capability of high-fidelity simulation to predict combustion dynamics in low-emission gas turbine combustors. To meet that goal, a model configuration of a lean-direct-injection (LDI) combustor was designed and then tested by simulation and experiment. To ensure the same physics were represented in the experiment and the simulation, strict requirements were placed on self-excitation, boundary conditions, and measurement accuracy. The experimental component of the project forms the basis of this dissertation. This task is divided into three principal components:

- Development of two sets of prototypical single element high pressure (1 MPa) LDI combustors with strict requirements on self-excitation, boundary conditions, and measurement accuracy, with and without optical accessibility, to produce longitudinal mode self-excited combustion instabilities (target frequency ~400 Hz; target amplitude ~1-3% peak-to-peak pressure fluctuations of mean chamber pressure).

- To parametrically survey and to provide a comprehensive description of the effects of combustor geometry, inlet air temperature, global equivalence ratio, fuel nozzle location and fuel composition on the combustion dynamics behavior of the LDI combustor.

- Demonstration of laser-based measurements, with high temporal and spatial resolution, to reveal the flame-acoustic-hydrodynamic interactions in the LDI combustor. Application of analysis tool sets for the extraction of turbulent reacting flow physics from the high resolution measurements and comparison with concurrent numerical simulations.

1.4 Scope of the Document

Chapter 2 is devoted to the review of literature related to prior studies of relevance to the dissertation. Recent work on low dry-NOx emission gas turbine combustion concepts, especially LDI is reviewed. The significant development risk to new combustor development due to combustion instabilities, the mechanisms that drive it with a focus on swirl stabilized flame configurations is reviewed. Diagnostic tools to measure, with high

spatio-temporal resolution, the pressure, flame heat release and flow-field are described briefly. The chapter places an emphasis on work related to LDI combustion. The relevance of past studies to the present work and missing pieces of information, especially related to multi-phase, high pressure combustors presenting self-excited combustion instabilities over a wide spectral range (~0.3-7 kHz) is discussed.

Chapter 3 provides the design methodology for the single element LDI combustor used in the current work. A brief description of the acoustic analysis based on Linearized Euler Equation (LEE) solver along with an estimation of hydrodynamic features used to design the chamber are described. Test apparatus for both phases of the experimental work, phase 1 well-instrumented modular metal chamber combustor and phase 2 optically accessible chamber, are described in detail. A summary of how a typical test is performed in the LDI combustor is presented at the end of the chapter.

Chapter 4 details the results from a parametric investigation of its combustion dynamics behavior as a function of combustor geometry, inlet air temperature and global equivalence ratio are presented. The parametric survey was a significant effort, with over 100 tests on eight configurations. The survey measurements showed a very strong dependence of instability amplitude on the geometric configuration of the combustor, i.e., its acoustic resonance characteristics. Measured pressure fluctuation amplitudes ranged from 5 kPa (0.5% of mean pressure) for a 3/8-wave air plenum, ½-wave combustion chamber configuration to 200 kPa (~20% of mean pressure) for a ¼-wave air plenum, ¼-wave combustor configuration. Except for the most stable cases at low equivalence ratio, the dominant unstable mode was consistently around 1400 Hz regardless of geometry. The

stability behavior showed a consistent and pronounced dependence on equivalence ratio and inlet air temperature. Instability amplitude increased with higher equivalence ratio and with lower inlet air temperature. A band of high frequency modes around 6 kHz were also observed for most configurations and operating conditions. At certain conditions the acoustic power amplitudes of these higher frequency modes were comparable to the longitudinal modes around 1400 Hz.

Chapter 4 also describes spray measurements using a phase Doppler particle analyzer (PDPA) was used to measure the drop size distribution and droplet velocities for an unconfined spray at atmospheric pressure. The measurements were performed with and without a co-flow of air around the fuel nozzle. Drop sizes of 15-70 μm, axial droplet velocities up to 15 m/s and a spray cone angle of 68-70° were measured.

Chapter 5 describes optical measurements carried out in the LDI combustor. Planar Laser Induced Fluorescence (OH-PLIF) measurements at 10 kHz were performed at the central cross-section of the combustor for equivalence ratios ranging from 0.44 to 0.6 at an inlet air temperature of 800 K. A gradient-based edge detection routine was used to extract the flame-front location from the OH-PLIF images. Planar flame surface density calculated using the extracted flame-front shows a compact flame (Lf ~ 25 mm) atϕ=0.6 and a more diffuse flame (Lf ~ 35 mm) at ϕ=0.44. Dynamic Mode Decomposition (DMD) analysis of the flame front shows a strong flame response at the 4L and 8L acoustic mode frequencies for ϕ=0.6 and at the 3L frequency for ϕ=0.44, while a response at the other acoustic mode frequencies is not captured. The OH-PLIF results at ϕ=0.55 show similar trends as that at ϕ=0.6. The strongest flame response is observed at the 4L and 8L acoustic mode

frequencies but the overall flame response is spatially more distributed compared to the ϕ=0.6 test case. Particle Imaging Velocimetry (PIV) measurements were performed at 5 kHz for non-reacting flow but glare from the cylindrical quartz chamber limited the field of view to a small region in the combustor.

Chapter 6 provides a summary of the completed work presented in the thesis document. Significant conclusions based on both, the parametric survey of combustion dynamics behavior of the LDI combustor and, the more detailed examination of the instabilities in the combustor using results from the OH-PLIF measurements are presented. Recommendations for future work based on the conclusions of the present work and leveraging continued developments lasers and high-speed cameras, providing ability for higher spatial and temporal resolution are described. Focus of the future work is also placed on development of techniques to enable use of limited experimental data for comparison with detailed high-fidelity simulations.

CHAPTER 2. LITERATURE REVIEW

Low emission gas turbine combustors have received an increased interest in the last several years due to the environmental impact of atmospheric pollution. Several ultra-low NOx emission combustor designs and concepts have been proposed, including but not limited to lean premixed pre-vaporized (LPP), rich burn- quick quench- lean burn (RQL), and lean direct injection (LDI). These concepts are centered on lean operation for thermal NOx reduction through premixed and partially premixed flames. [12-14]. While these concepts have shown reduced NOx emissions, they seem to promote a coupling between acoustics, hydrodynamics and combustion that can lead to combustion instabilities. These combustion dynamics can be quite complex, and a detailed understanding requires reliable simulations of the combustion flow-field.

The current chapter reviews the current state of research in low emission gas turbine combustion with a focus on combustion instabilities. The LDI related research is highlighted first with a focus on spray-acoustic interactions and vortex-flame interactions in the later part of the chapter. A brief literature review of optical diagnostic methods with application to high pressure combustors is presented at the end of the chapter.

2.1 Low Dry-NOx Gas Turbine Combustion Concepts:

High compression ratios and high turbine inlet temperatures have resulted in increased overall efficiency of gas turbines in the last several years. This improvement though is offset by the requirement for environmentally [15] benign low emissions, imposed by international regulations and an increased awareness of the environmental impact of emissions. High pressure and temperatures have also reduced the emissions of unburned hydrocarbons (UHCs) and carbon monoxide through higher combustion efficiencies and faster fuel oxidation. On the downside, however, high combustion temperatures increase the NOx emissions. To effectively reduce NOx emissions, from the point of view of liquid-fueled gas turbines, Lean Pre-mixed Pre-vaporized (LPP), Rich-burn/Quick-quench/Lean-burn (RQL) and Lean Direct Injection (LDI) combustor design concepts have been studied [16, 17]. Some methods of NOx reduction in gas turbines are listed below [4, 18]:

- Secondary injection of water-in-oil emulsification with fuel/water/steam to decrease the heterogeneity and temperature of the fuel-air mixture thus reducing the NOx emissions. This method carries the side-effect of reduction in the thermodynamic efficiency of the combustion process.

- Selective catalytic reduction, such as injection of ammonia in the exhaust gas stream to break down the NOx to N_2 and H_2O is effective in reducing the NOx emissions but its applicability is restricted to stationary land-based use.

- Rich Burn- Quick-Lean Burn (RQL) is a staged combustion technique for low NOx combustion. While the reduction in NOx emissions achieved by RQL is not as low as

lean premixed pre-vaporized (LPP) technique, the combustor is has advantages of being very stable.

- Lean premixed pre-vaporized (LPP) provides a premixed fuel –air mixture into the combustor ensuring operation at low equivalence ratios and lower NOx emissions. Several authors agree [19] that LPP based combustors have the highest promise to achieve lowest NOx emissions, have high durability and superior performance. Proper fuel-air vaporizing and mixing stage and the flame-holding stage are most critical to the performance of the LPP combustor. Susceptibility to flashback and auto-ignition are some of the drawbacks of LPP combustors. These drawbacks are expected to get further aggravated with the long term ICAO-CAEP requirements for higher operating operation ratios along with reduced NOx emissions.

- Lean Direct Injection (LDI) is a concept in which the fuel is directly injected into the reaction zone [20]. Studies conducted to compare LPP and LDI concepts [19] have shown show similar NOx levels and higher overall efficiencies under similar operating conditions. Similar to the LPP combustor, proper fuel-air vaporizing and mixing stage and the flame-holding stage are most critical to the performance of the LDI combustors as well. A lot of research therefore has been performed with the objective of ensuring ensure effective atomization leading to abrupt vaporization and uniform vapor-air mixing to avoid high temperature pockets in the combustor.

2.2 Lean Direct Inject Low Dry-NOx combustion:

The lean direct injection (LDI) concept was developed in the 1980s to assist in meeting the dual requirements of low-NOx production and high performance [12-14, 20, 21]. The concept was developed to facilitate rapid, stable, and uniform combustion under lean operation, resulting in lower combustor peak flame temperatures and reducing primary emission contributions from the thermal NOx mechanism.

The multi-point LDI (MP–LDI) [22] concept incorporates a large number of smaller fuel injectors in place of a conventional, single injector. The reduced scale promotes rapid mixing of fuel and oxidizer, and the conditions at the flame front approach those in a premixed, pre-vaporized flame. Multiple injectors can be integrated into modules to allow for a variety of fuel staging possibilities appropriate for a landing and take-off (LTO) engine cycle as defined by ICAO. It is designed to rapidly mix fuel and air so that stable combustion occurs within a short distance. Swirl is imparted to the air to generate recirculation zones that anchor the flame(s) near the fuel injection sites. Figure 2.1 shows a schematic diagram of a MP-LDI combustor. NOx emission measurements performed by Tacina et al [23] for a 25 and 49 element combustor operating at up to 2.8 MPa demonstrated rapid mixing and burning, as little as 15 mm from the injector dome. The NOx emissions measurements were found to be lower for a 25 and 49 element combustor (NOx emission index of 9) compared with a 36 element combustor, concluding that a higher number of elements was not a critical parameter for the LDI concept. The NOx emission index relates the NOx generation to the inlet air temperature, injector pressure drop, equivalence ratio, and inlet pressure.

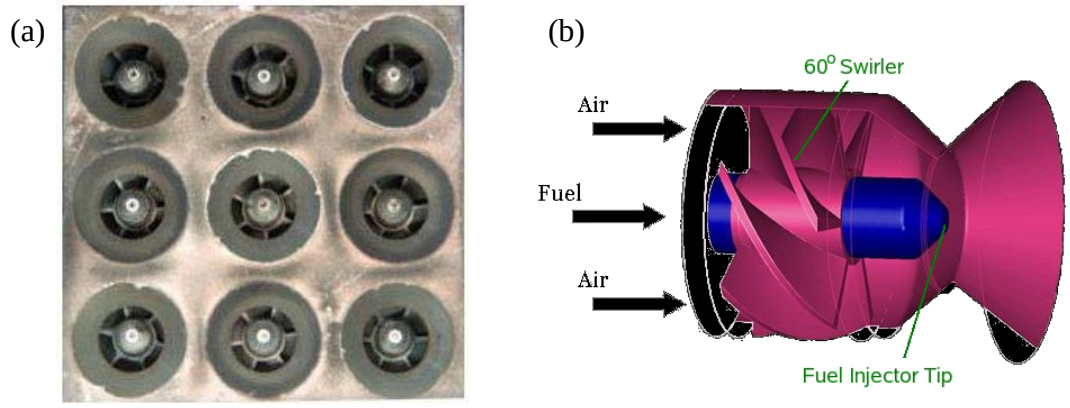

Figure 2.1. (a) Schematic diagram of a MP-LDI combustor. (b) Schematic drawing showing the relative spatial positioning of the air swirler, fuel nozzle, and venturi for each injector element [24-28].

Several studies conducted over the past two decades, including those at Purdue University, have been focused on the characterization of the flow-field and measurement of NOx emissions in realistic LDI configurations. Thariyan et al. [25-29] conducted dual pump CARS and OH-PLIF measurements in a single element top-hat configuration LDI combustor at 1 MPa and inlet air temperatures up to 725 K. Cooper et al. [19] performed LIF measurements of NO in a single element LDI spray flame using heptane as the fuel. They found a pressure scaling corresponding to $P^{0.74}$ with the NO measurements in the flame. Gore [30] compared the LDI flame structure and NO production and emission to that of partially premixed flames. A methane- air atmospheric pressure flame was used for this study. A dependence of optimum partial premixing of the flame to NO emission index was found.

Dewanji et al [31, 32] conducted LES simulations of both a single and a nine-element LDI combustor at atmospheric pressure for an inlet air temperature of 776 K and equivalence ratios of 0.41 and 0.7. Formation of vortex structures in the gas phase such as the vortex

breakdown bubble (VBB) and the precessing vortex core (PVC) were found to be critical to fuel distribution and consequently the location of the flame front in the combustor. Yi et al [33-35] studied a Jet-A fueled combustor at moderately higher pressure (0.3 MPa) and found pressure fluctuations amplitudes as high as 8% of the mean chamber pressure with longitudinal mode frequencies of 371 Hz (1L), 699 Hz, and 1400 Hz. Dependencies of equivalence ratio, incoming air flow rate and air temperature were reported with higher equivalence ratio and lower air flow rate and temperature being more unstable. Meadows et al [36, 37] investigated passive control of combustion instabilities in a single element LDI combustor operating at atmospheric pressure and used porous inserts to dampen instability amplitudes by reducing the mixture fraction inhomogeneity in the combustion chamber.

2.3 Spray-Acoustic Coupling:

The introduction of liquid fuel as a hollow cone, poly-disperse spray results in stratification of fuel, leading to change in the flame structure caused by the inhomogeneity in mixture fraction. The spatio-temporal uneven and unsteady response of fuel and air to incident acoustic waves can also alter the swirling flame characteristics. De la Cruz Garcia [38] reported self-excited combustion instabilities in an atmospheric pressure kerosene flame that were closely related to the fluctuations of the spray motion and droplet evaporation. Some studies at atmospheric and moderate pressures have been reported [38-40] with non-premixed and partially premixed flames in liquid fueled combustors, but more work on high pressure unstable spray flames is necessary to investigate of these mechanisms.

Several studies have been performed to characterize the coupling between sprays and acoustic fields in the LDI combustor and other low-emission combustor configurations. Anderson et al. [41-44] used a forcing mechanism (speakerphones) to introduce instabilities to a spray that was injected into the ambient quiescent atmosphere. The spray properties were measured using planar laser induced fluorescence (PLIF). The forced acoustic signal was correlated to the mass flow fluctuations emanating from the spray to characterize a relation between spray and the acoustics. The experimental arrangement used has been shown in Figure 2.2 below.

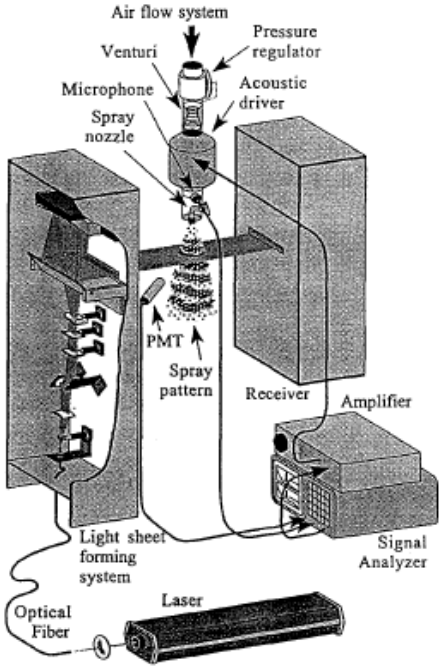

Figure 2.2. Experimental arrangement for PLIF measurements in an acoustically coupled spray [42]

To quantify the degree of interaction between the pulsed air flow (forcing function) and the fuel spray (output), the coherence between the acoustic pressure signal and

photomultiplier (PMT) signal signals was measured for a variety of flow conditions. A high coherence indicates a linear transfer function between the mass –flow fluctuations (PMT voltage fluctuation) and the pressure fluctuations.

Chisty [45, 46] studied the thermoacoustic instability and the transition of the combustor to unstable regimes via phase-locked chemiluminescence imaging and measurement and phase-locked acoustic characterization. It was found that the onset of the thermo-acoustic instability is a function of the energy gain of the system, while the sustenance of instability is due to the in-phase relationship between combustor acoustics and unsteady heat release driven by acoustic oscillations. The presence of non-linearities in the system between combustor acoustic and heat release and also between combustor acoustics and air through-flow were found to be present.

Several experimental studies conducted at the University of Cincinnati have reported detailed drop-size distributions for the LDI configurations with varying swirler geometry and fuel injector locations [47-50] As of now, very few studies were found in the open literature where self-excited combustion-spray instabilities have been studied. This is important because forcing the acoustic instabilities may not represent accurately the same complex mechanisms that are found in combustors that are driven unstable using external sources like microphones.

2.4 Swirl- Thermoacoustic Interactions

Swirl flows with vortex breakdown are widely used in combustion systems for flame stabilization. Lean Direct Injection (LDI) combustion devices have a high swirl number

and heated air flow that is accelerated through a subsonic converging diverging venturi. This swirling flow can develop rotating helical hydrodynamic modes in the combustor. At certain operating conditions and combustor configurations these helical modes can interact with thermoacoustic modes of the combustor leading to amplification of combustion instabilities in the combustor. A precessing vortex core (PVC) is one way in which these swirling modes can manifest. These are more prevalent in cold flows and their existence in reactive flow is often questioned. The role of PVC in anchoring the flame is established though its influence on combustion instability is far less well known [51]. Swirl-acoustic interactions have been described in quite a few prior experimental and computational studies for both premixed and partially premixed flames and has been an area of detailed study over the past few years [51-71].

Syred [72] reviewed occurrence of precessing vortex core (PVC) and other hydrodynamic instabilities associated with swirl combustion that allow for coupling between acoustics and combustion. He observed that the occurrence of the PVC and its amplitude were strong function of mode of fuel entry, equivalence ratio and level of confinement. Except for low equivalence ratios, PVC was generally seen to be suppressed.

Candel et al. [56, 62, 73, 74] presented a review of swirl flame dynamics mechanism. They showed that interaction of an incident acoustic wave on a swirler led to generation of a vorticity wave that is convected by the mean flow. Interaction of the PVC with acoustic perturbations in the combustor giving rise to non-linear interaction modes was identified using experiments using a premixed methane air flame. The interaction modes were seen

to be presented at a frequency that was the difference between the PVC mode and the acoustic mode frequency.

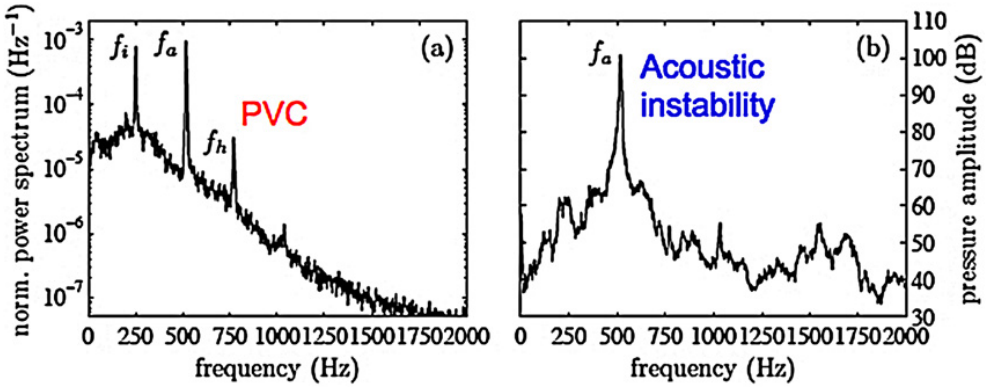

Figure 2.3. Spectral density measurements of chemiluminescence and pressure measurements from a premixed-methane flame $\phi = 0.69$ $U_b = 9.9$ ms-1. f_i, f_a and f_h denote interaction, acoustic and PVC mode frequency [62]

Stohr and co-workers [51, 54, 61, 69] conducted several studies to understand the vortex-flame interactions in a model gas turbine combustor. A non-premixed methane air flame at varying values of thermal power, which were varied to establish different Damkohler numbers in the flame, was used in this study. PIV and OH-PLIF measurements were used to study the flow and flame characteristics. They reported that the flames were stabilized in the shear layer of the inner recirculation zone where the PVC was located. PVC was found to be the dominant unsteady flow structure leading to convection-enhanced mixing in the flame.

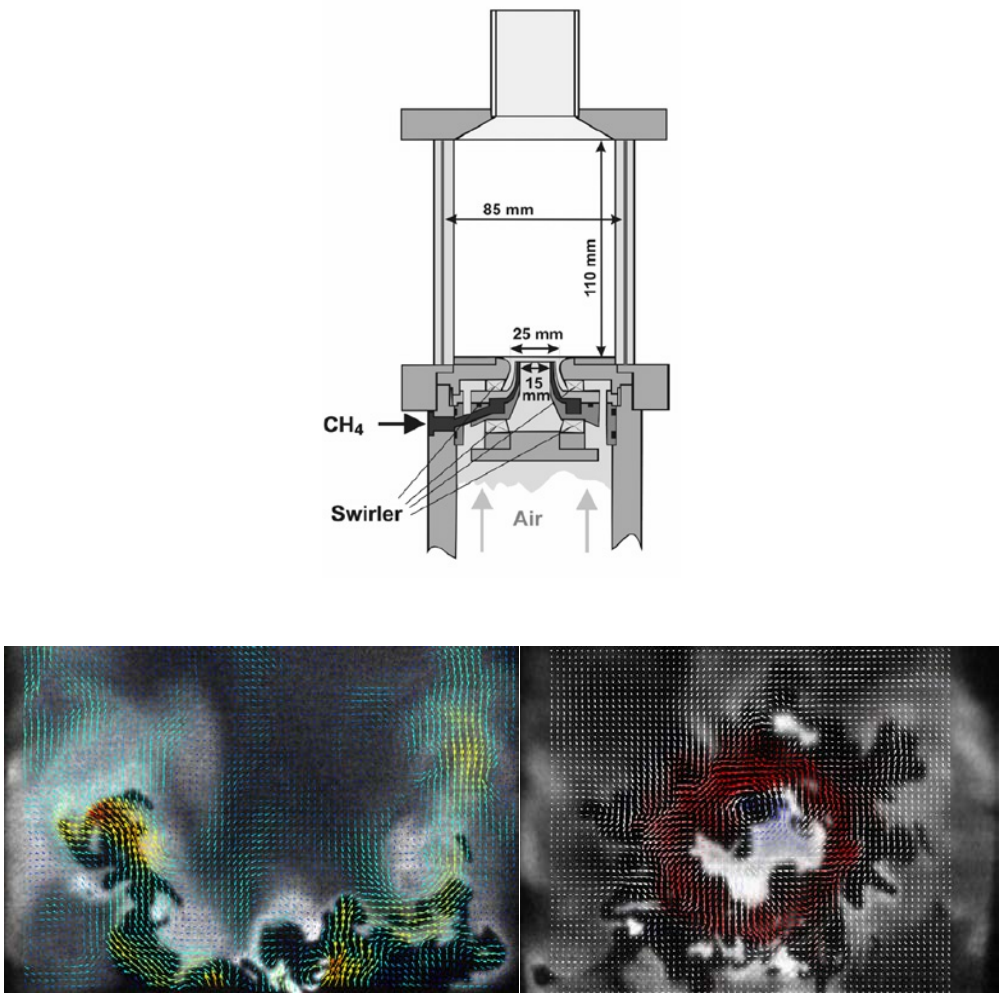

Figure 2.4. Side view of model gas turbine burner used by Stohr et al.[51] Simultaneous OH-PLIF and PIV measurements obtained in the combustor showing measurements in the vertical cross-section and at two horizontal sections (y= 5 mm and y= 10 mm)

Santavicca and co-workers [33-35, 75] have conducted several experiments using both single and multi-element unstable LDI combustors. Experiments were conducted using Jet-A up to pressures of 0.3 MPa. CH*-chemiluminescence and dynamic pressure measurements were obtained for multiple inlet air temperatures and equivalence ratios. The doughnut shaped flame located outside the PVC was observed. The flame structure was found to be similar to that with premixed flames. Depending on operating conditions half

wave and full wave modes of the combustion chamber were seen to be excited with maximum pressure fluctuations on the order of 8% (peak to peak) of the mean chamber pressure.

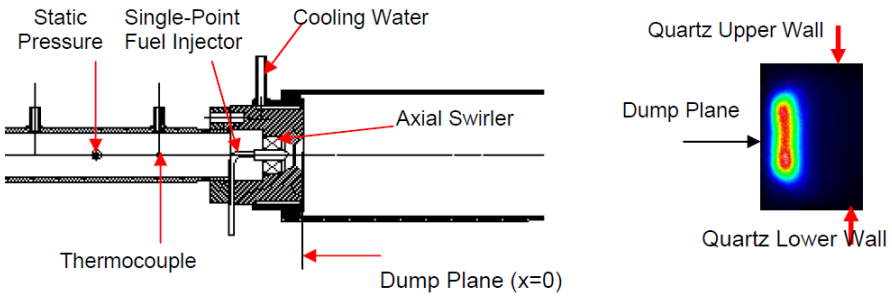

Figure 2.5. Schematic diagram of the LDI combustor used in the study by Santavicca et al. [35]

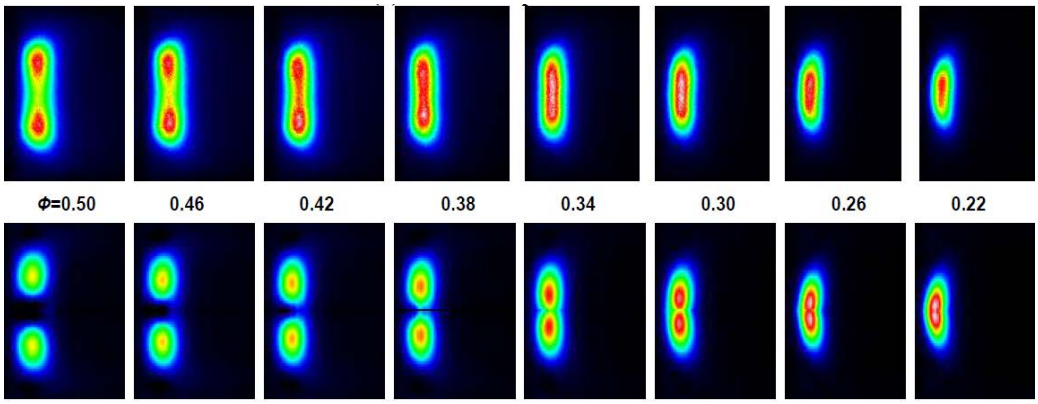

Figure 2.6. Line of sight and 2D ICCD images of CH*-chemiluminescence of the LDI flame at an air mass flow rate of 22.2 g/s and an air inlet temperature of 773 K [35]

Poinsot and co-workers [67, 76, 77] have conducted several computational studies using LES to look at combustion instabilities in swirling flames. The occurrence of the PVC mode and its effect on chamber acoustics was studied during non-reacting as well as reacting flow conditions. The PVC mode was seen to dominate in the cold flow but get damped once the flame was set-up. On the other hand, the acoustic modes of the chamber

were excited on combustion. The study conducted by Hermeth et al. [67] showed a bi-stable existence of the swirling flame- attached to the burner with no existence of PVC or a detached flame with a strong PVC mode coupled with chamber acoustics based on the chamber configuration and activation of the computational model.

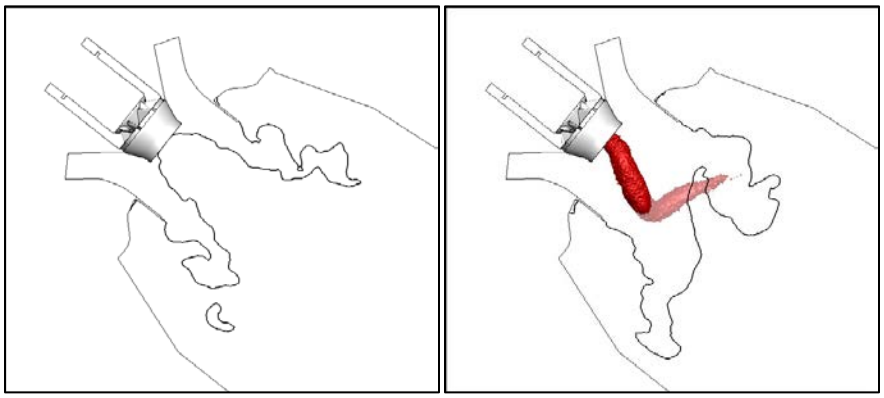

Figure.2.7: Temperature iso-line (T/Tmean = 1.30 and pressure iso-surface visualizing the PVC structure for attached (left image) and detached (right image) flame. The PVC is strong for the detached flame while it disappears for the attached flame. [67]

Patel et al. [78, 79] conducted large eddy simulations (LES) of a liquid fueled single element LDI combustor to investigate spray-turbulence-flame interactions. A similar swirler-venturi-injector configuration to the one used in the present work was used in this work. The interaction of the spray with the PVC and the role of a vortex breakdown bubble (VBB) in flame holding were discussed. Existence of a non-premixed flame front in the central portion of the flow field and premixed burning mode further away was identified in the computations based on the Takeno flame index [80].

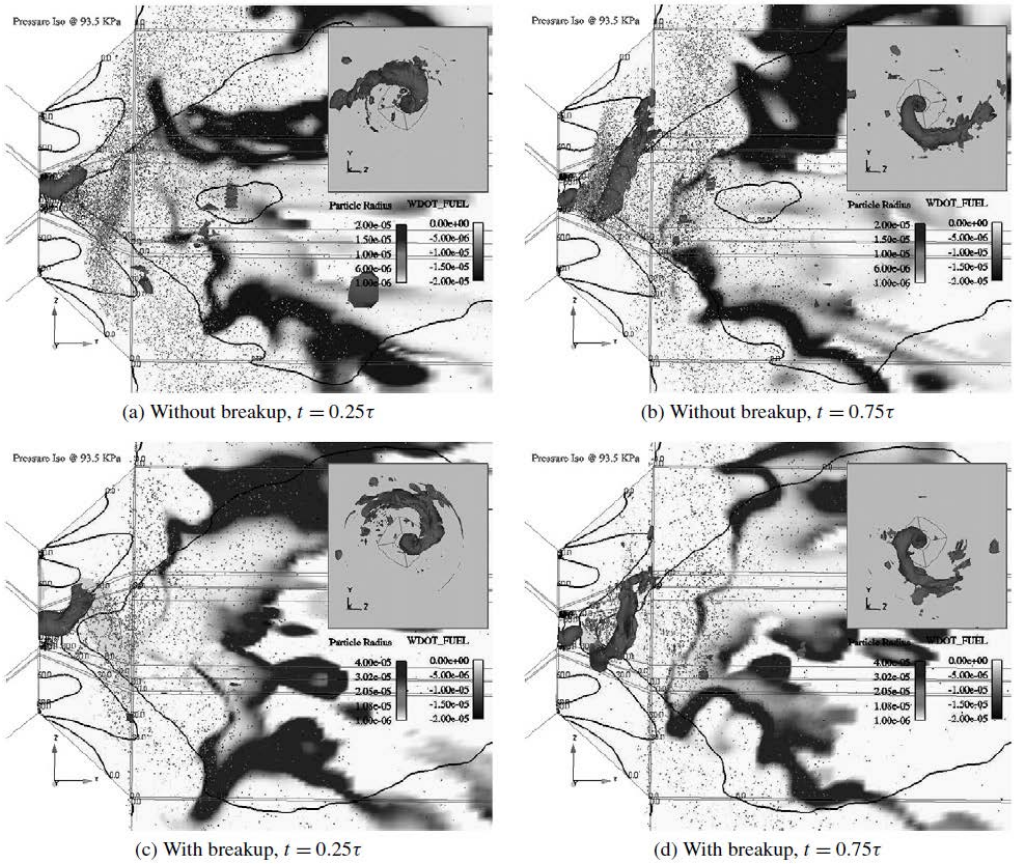

Figure.2.8: Visualization of instantaneous droplets, fuel reaction rate (dark colored) and the PVC for simulations with and without a spray break-up model (Patel and Menon 2008)

2.5 Optical Diagnostic Techniques and Interpretation of Data

Laser-based measurement techniques provide the only non-intrusive means of collecting quantitative data in a turbulent reacting flowfield. For obvious reasons, the application of these techniques is quite challenging under the flame conditions seen in most modern combustors. The first requirement, maintaining optical access, requires extensive design efforts to ensure that the windows withstand the extremely high temperatures and pressures, which can be greater than 2000 K and 5 MPa, respectively. Only a select few

research groups in the world have achieved these testing capabilities and the availability of the data produced remains quite limited. This is due to the high cost associated with large-scale experiments in addition to the physical challenges of performing useful measurements in such environments. Several diagnostic techniques for understanding flow physics and the flame behavior in gas turbines combustors, atmospheric flames and other combustion devices are widely prevalent in literature. Taking into account the techniques that have been applied to the current work, a summary of the application of chemiluminescence, planar laser induced fluorescence (PLIF) and particle imaging velocimetry (PIV) techniques and the analysis of the data obtained from them is described below. Previous studies with a focus of gas turbine combustion are reviewed.

Chemiluminescence emission of excited radicals such as CH* or OH* from flames are widely used for heat release visualization from flames. CH* and OH* both are indicator of the flame front, but chemiluminescence emission of these species is assumed to offer a view only of the global heat release from the flame. A broadband emission from CO_2* from the flame that lies across the CH* and OH* lines also affects the signal measured from the flame. Chemiluminescence provides line-of-sight integrated information so any 3-D distribution of the heat release is not obtained. Moeck et al [81] used chemiluminescence from a single camera with a side view of the combustion chamber for tomographic reconstruction of heat release perturbations induced by helical modes in turbulent swirl flames. Techniques like scaled Abel inversion, algebraic reconstruction technique (ART), filtered back projection and Chebychev-Zernike expansion were used to reconstruct the dominant PVC mode in the combustor.

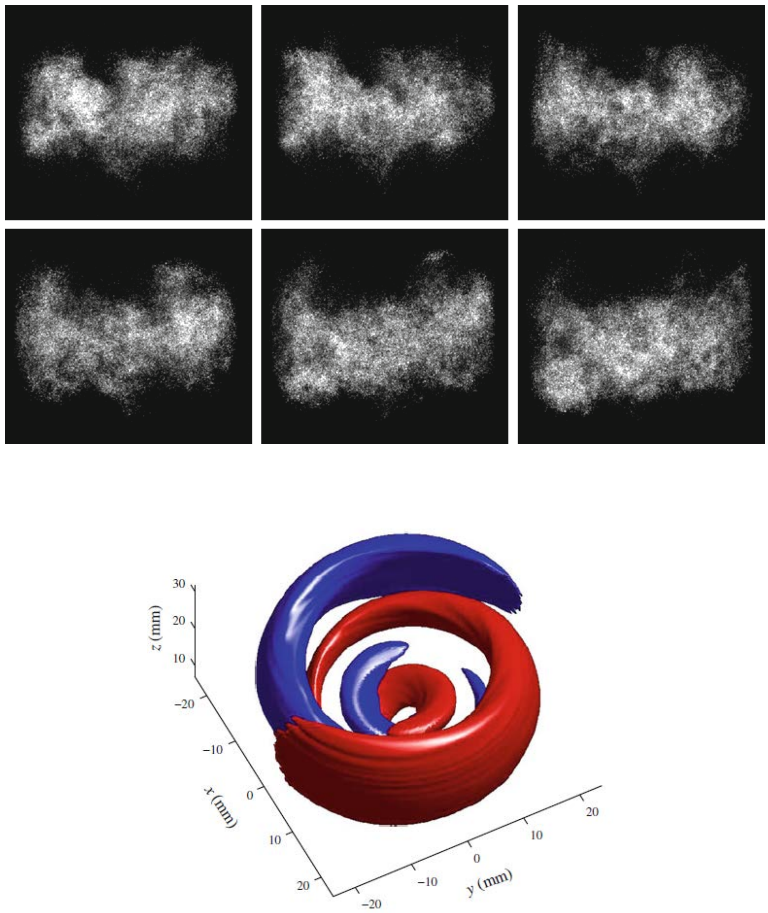

Figure.2.9: CH* chemiluminescence raw images of the flame over a single cycle of the PVC mode in the combustor (left) and iso-contours depicting tomographic 3D reconstruction of the heat release fluctuation using the Chebychev-Zernike algorithm (right)) [81]

Laser Induced Fluorescence (LIF) is a technique in which spatially, temporally and spectrally controlled light is used to excite molecules from their ground state to a higher energy state. As the molecules return to their ground state they emit spontaneous radiation (fluorescence) that provides sensitive spatially and temporally resolved measurements [82]. Planar LIF (PLIF) provides a two dimensional spatially resolved map of the excited combustion radical concentration, typically OH, to provide high fidelity information of the

flame front. The technique still remains qualitative in nature as far as radical concentrations are concerned.

Particle Image Velocimetry (PIV) provides a quantitative measurement of instantaneous velocity across a planar flow field through tracking of the motion of seeded particles in the flow over a known time separation. The quantitative nature of the measurement that allows direct comparison with simulation results makes it promising for experiments designed for the generation of validation data. Several studies over the past many years have used PIV measurements for flow characterization [83]. More recently, planar, stereo and tomo-PIV measurements at 5-10 kHz have provided important insight into complex turbulent flow fields in combustors [64, 84, 85].

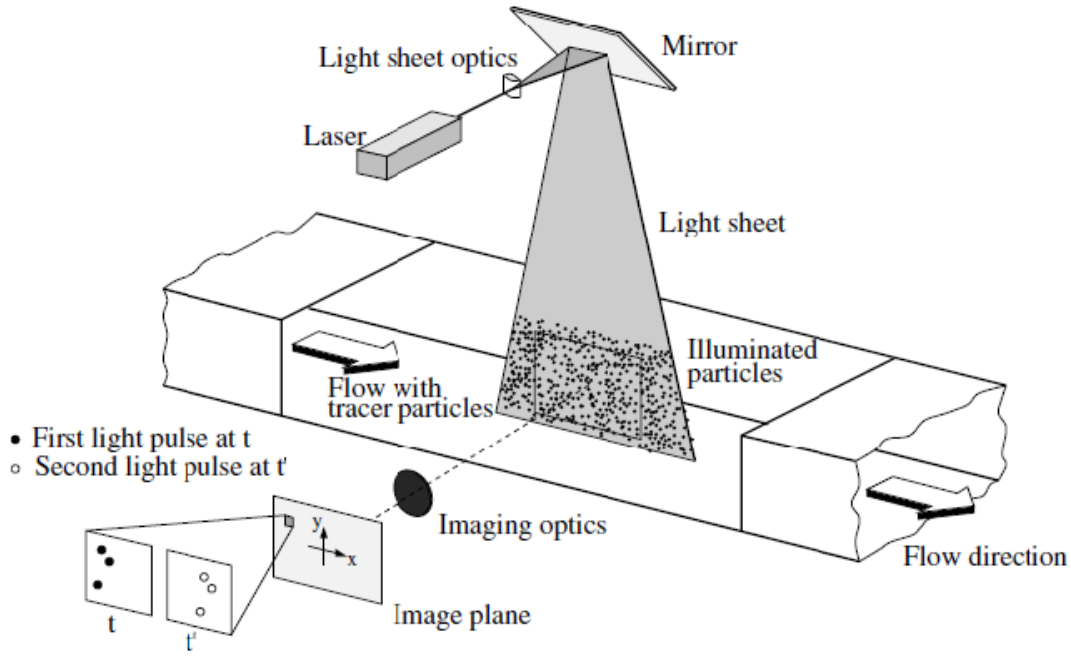

Figure.2.10: Schematic diagram of a typical PIV experiment [83]

Simultaneous application of the PLIF and PIV technique performed a multi-kHz repetition rates offers advantages provided by both techniques to understand the flow field interactions with the flame front in the combustor. Some recent studies have been completed at elevated pressures using 3-5 kHz simultaneous OH-PLIF and PIV in methane air flames at DLR, Stuttgart. Results obtained from these studies were able to provide high fidelity quantitative information about vortex-flame-thermoacoustic interactions in highly turbulent flow fields. Figure below provides an illustration of the results obtained.

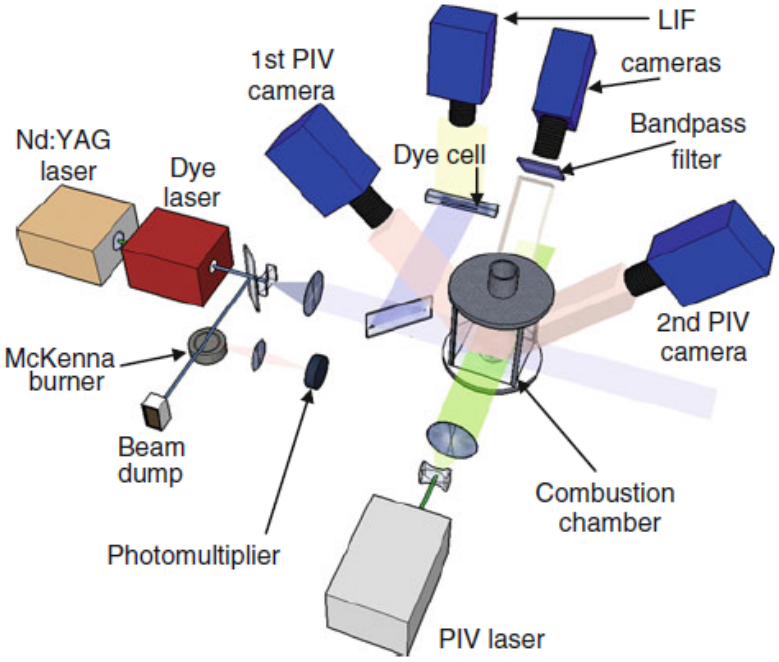

Figure.2.11: Set-up for simultaneous PLIF-PIV experiment [64]

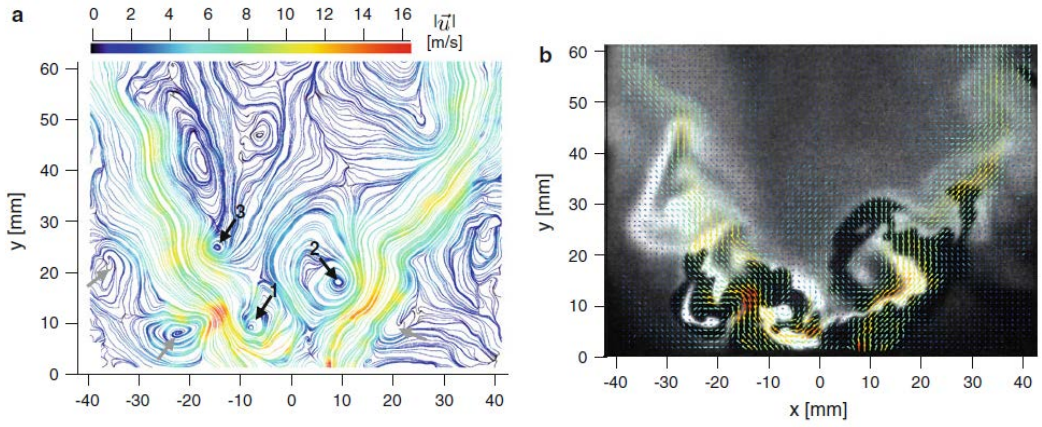

Figure.2.12: Simultaneous PIV and OH-PLIF measurement: a) streamline plot of velocity field and b) vector plot with corresponding distribution of OH [64]

2.6 Summary

To reiterate, the success of the LDI configuration as a stable, low emission gas turbine concept is critically dependent on rapid fuel-air and mixing and a compact combustion zone under lean operating conditions. The swirling air flow and uniform fuel spray atomization along with the swirler-venturi-injector geometry are critical to this. On the other hand, these very processes can couple with the chamber acoustics and make the combustor to combustion instabilities. The incidence of acoustic waves on the swirling, especially, leads to the formation of vorticity waves, that promotes mixing, but on the other hand can promote formation of the PVC and VBB instabilities. Significant progress, including highly resolved measurements and lower order approximations such as flame transfer functions and flame describing functions have been studied over the last few years. The majority of the work, however has been restricted to premixed and partially premixed configurations with gaseous fuels and low chamber pressures. Introduction of liquid fuel,

especially at high amplitude combustion instabilities that exceed the pressure drop across the injector in typical gas turbine combustors can significantly drive the spray break-up, vaporization dynamics and can lead to significant alteration in the local mixture fraction in the combustor. The presence of high frequency dynamics, rarely reported in gas turbine combustion experiments can be driven by these non-linear high amplitude dynamics. The acoustic time-scales of a few hundred hertz are typically in the same margin as these dynamic processes and can significantly enhance the chances of self-excited instabilities.

The objective of the current work is to provide a comprehensive description of the effects of combustor geometry, inlet air temperature, global equivalence ratio, fuel nozzle location and fuel composition on combustion dynamics to test and validate predictions made by high-fidelity predictions of combustion dynamics. In a parallel effort, computational studies performed on the same geometry and operating conditions used in this study [86-91] show the significance of the swirl acoustic interactions that result in a vortex breakdown bubble (VBB) that plays a significant part in the flame holding and stabilization processes that dictate the combustion response to the combustor acoustics. These experimental results have also been previously used to test various atomization models. The computations highlight the influence of the spray break-up and fuel-air preparation in the subsonic venturi on the complex coupling processes between chamber acoustics, heat release, and hydrodynamics. Rapid spray break-up and droplet evaporation, and uniform fuel-air mixing is seen in stable configurations at the low near LBO equivalence ratios similar to premixed gaseous flames. Unstable configurations at high equivalence ratios show higher degree of fluctuation in the spray break-up driven by chamber acoustics.

The design of the experimental arrangement and instrumentation is described in the next chapter followed by a discussion of results from detailed high frequency pressure measurements in the combustor showing discriminating effects of combustor geometry, inlet air temperature, global equivalence ratio, fuel nozzle location and the fuel used are described thereafter. Conclusions based on the parametric study are presented followed by determination of a baseline configuration to which high fidelity laser based diagnostics were applied. High-frequency measurements of OH*-chemiluminescence and OH-PLIF and velocity fields using PIV obtained at a relatively stable, low equivalence ratio case and a less stable case at higher equivalence ratios.

CHAPTER 3. EXPERIMENTAL ARRANGEMENT

3.1 Introduction and Test Facility

The single element LDI combustor design is based on axial mode combustion dynamics with a fundamental (1L) frequency between 300-400 Hz. The combustor operates at a mean chamber pressure of 1 MPa, and uses kerosene fuel (Jet-A or FT-SPK) and heated air up to a temperature of 800 K. The combustor is designed to provide high fidelity measurements of combustion dynamics, allows the application of laser based optical diagnostics (optically accessible version) and provides well defined acoustic and flow boundary conditions to allow modeling of the combustor physics for validation. The chamber design is modular and parametrically evaluated variables included geometry and acoustic resonance, inlet temperatures, equivalence ratio, and type of liquid fuel. The parametric survey conducted as a function of these variables has been a significant effort, with over 100 tests at distinct operation conditions on eight geometric configurations. The experiment is located at the High Pressure Laboratory (HPL) at M. J. Zucrow Laboratories. The lab facilities provide regulated high pressure and high flow capabilities for air, nitrogen, liquid fuels, natural gases and a host of other fuels, oxidizers and inert gases that can be independently regulated and measured [92-94]. A summary of lab capabilities at

HPL is tabulated below in Table 3.1. The fluid systems used for the LDI experiment are highlighted in the table in italics.

Table 3.1 Zucrow High Pressure Laboratory facility fluid system capabilities

Operational Parameters	Maximum Operation (Steady State)
Heated air supply 1	5 kg/s at 6 MPa and 1100 K (7 kg/s at 725 K)
Heated air supply 2	3.6 kg/s at 4.1 MPa and 810 K
Heated air supply 3	*0.25 kg/s at 4.1 MPa and 810 K*
Unheated air	0.45 kg/s (steady) with 9000 kg storage at 15 MPa
Oxygen	2 kg/s and 8 kg/s at 15 MPa
Bottled oxidizers	2 circuits at 1 kg/s and 15 MPa
Nitrogen	*0.05 kg/s (steady) with 9000 kg storage at 40 MPa*
Bottled inert gases	2 circuits at 1 kg/s and 15 MPa
Bulk fuel	*Natural gas, hydrogen, and liquid fuels to support >10 MW (steady)*
Bottled fuels	4 circuits at 1 kg/s and 15 MPa
Water	5 kg/s at 8.3 MPa (pump discharge) with 0.35 m^3 reserve

An electric heat exchanger, operating at full capacity, heats 0.25 kg/s air at 40 bar to 950 K provides the air supply to the combustor. The flow is regulated upstream of the heater

using a pressure regulator and mass flow rate is calculated across a choked venturi of known throat diameter and discharge coefficient. The toroidal sonic venturi design per ASME MFC-7M is used. An inert gas supply is used for experiment purges, pneumatic controls, and other system needs. Liquid nitrogen boil-off is pumped to 40 MPa at a rate of 0.05 kg/s for continuous operation, while over 9000 kg of gaseous nitrogen is stored at 40 MPa for higher rates of consumption. For liquid-fueled experiments, two certified flame-shield fuel containments are available for testing standard aviation fuels as well as other alternative blends. Fuel is supplied to the test stand through two separate legs for independent control of fuel split in research injectors. The system is operated at up to 10 MPa line pressure and the mass flow through each channel is controlled by two electronically actuated metering valves. The mass flow rates of both supplies are measured with Coriolis flow meters. One of the two circuits is used to supply Jet-A or FTK synthetic fuel to the LDI experiment depending on the experiment. Facility low pressure cooling water is supplied at 0.5 MPa for use in cooling the piezoresistive high frequency pressure transducers used in the experiment.

3.2 Experiment Design

The single element LDI combustor design is based on axial mode combustion dynamics with a fundamental frequency of 400 Hz. A schematic of the LDI combustor is first presented in Figure 3.1 below. Combustion instability amplitudes less than 0.5-1% of the mean chamber pressure were desired so that they are a fraction of the pressure drop across the subsonic venturi of the LDI element.

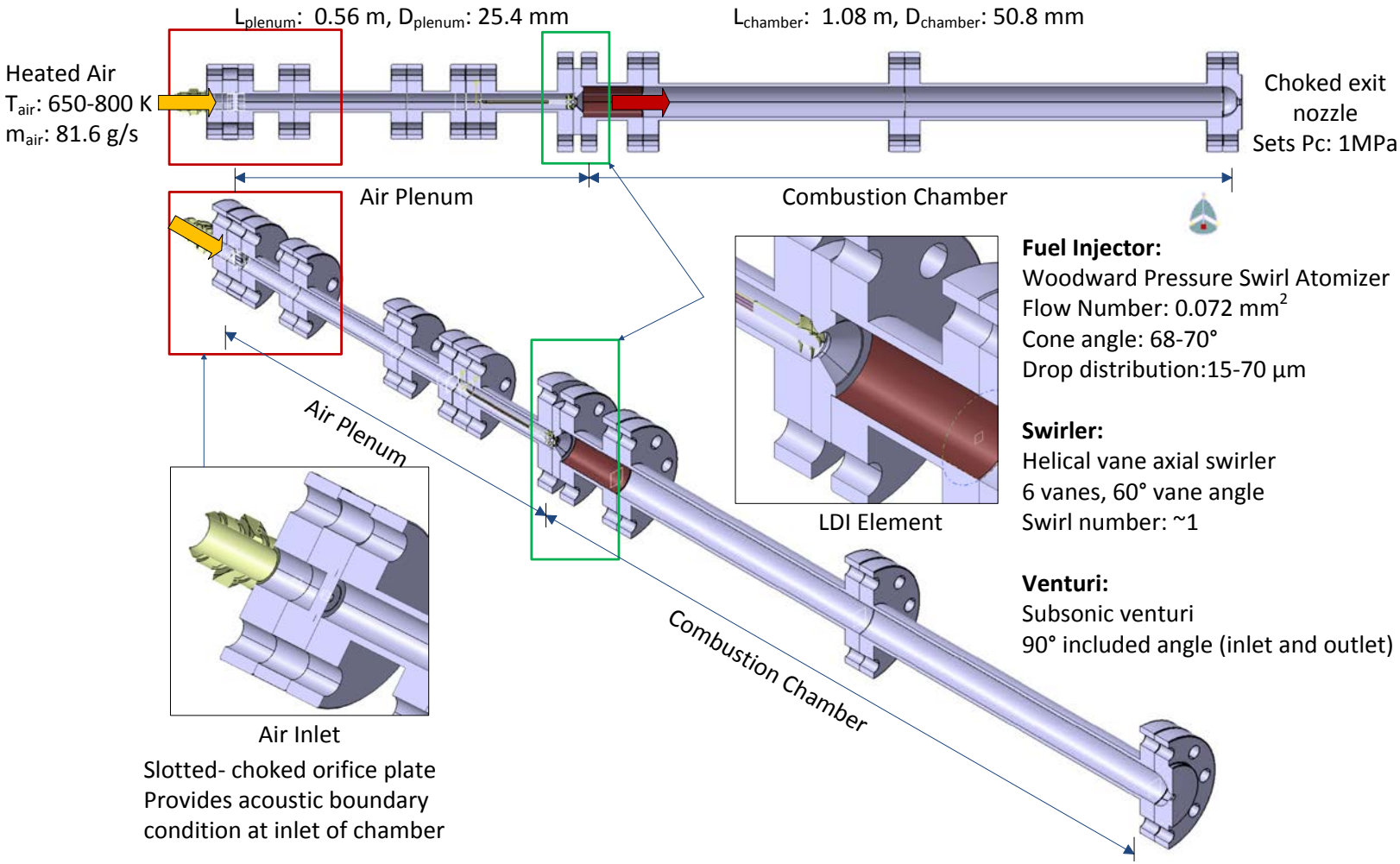

Figure 3.1: Schematic diagram of the LDI combustor

A brief summary of the design envelope and the nominal operation parameters have been listed in Table.3.2 below. The major dimensions of the combustor were determined with an analytical model that uses the nominal operation conditions tabulated below in Table.3.2 to calculate the mode-shapes in the combustor. A brief description of the analytical model and its results are given below.

Table.3.2 Summary of design envelope and nominal operation parameters

Fuel	-	Jet-A/ FT-SPK
Oxidizer	-	Air
Inlet Air Temperature	(K)	650-800
Equivalence Ratio	-	0.35-0.70
Target fundamental Mode (1L) Frequency	(Hz)	400
Inlet Boundary Condition	-	Constant mass inflow from a choked orifice
Exit Boundary Condition	-	Choked nozzle
Diameter of combustor	(mm)	50.8 mm (2.0 inches)
Diameter of air plenum section	(mm)	25.4 mm (1.0 inch)

3.2.1 Acoustic Analysis using Linearized Euler Equation (LEE) Solver

Combustion instabilities occur through a feedback mechanism between flow-field fluctuations (u'), heat release fluctuations (q') and acoustic pressure oscillations (P') in the combustor. To sustain self-excited instabilities, the pressure and velocity fluctuation

amplitudes at the location of fuel injection and at the combustion zone and their phase relationship with heat release from the flame are critical. An analytical one dimensional model based on Linearized Euler Equations (LEE) [95-97] was used to size the major dimensions of the LDI combustor.

The LEE model accounts for mean flow effects and entropy wave effects in the combustor. It also allows definition of multiple domains in the combustor to help define it with better resolution. Combustor geometry, flow properties are inputs to the model. Chemical equilibrium results obtained using the NASA CEA code [98] were used to specify combustion product properties. To calculate the chamber combustor modes, the heat of combustion (185 kW) was assumed to be released uniformly over a length of 50.8 mm (2”) from the fuel injection plane. The LEE analysis results were used to define the major dimensions of the combustor. Representative plots for the ½ wave and ¼ wave configurations of the air plenum section and the combustion chamber section are shown below.

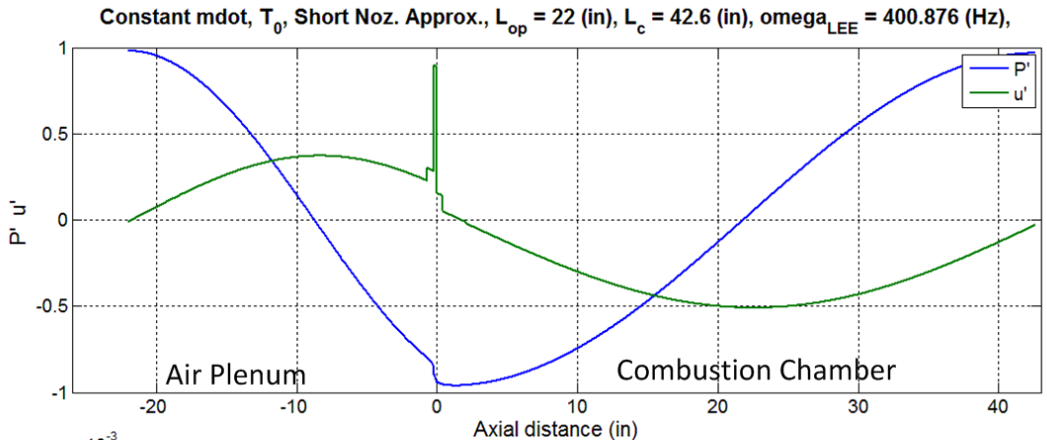

Figure 3.2. Normalized pressure and velocity fluctuations in the LDI combustor for the 1/2 wave mode of the air plenum and the combustion chamber calculated by LEE

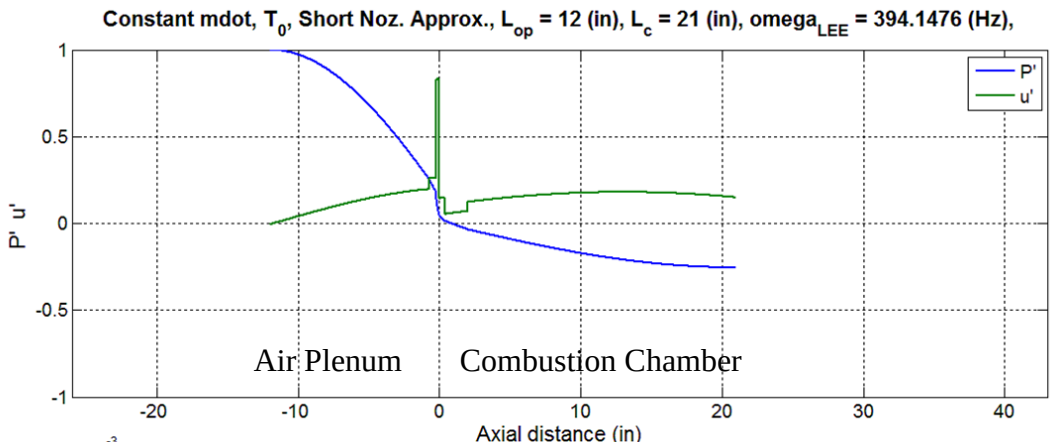

Figure 3.3. Normalized pressure and velocity fluctuations in the LDI combustor for the 1/4 wave mode of the air plenum and the combustion chamber calculated by LEE

Figure 3.2 shows the pressure (p') and velocity (u') fluctuations in the air plenum and the combustion chamber for a ½ wave configuration. The p' and u' values have been normalized by their mean values in the combustor. The zero location on the abscissa corresponds to the location of the fuel injector exit in the combustor. As shown in the figure, a pressure antinode and a velocity node exists at the location close to the fuel injection. This indicates that the velocity fluctuations are small enough that they may not interact strongly with the strong pressure fluctuations. The exactly opposite case is evident from the ¼ wave case shown in Figure 3.3. A pressure node and a velocity antinode exist at the inlet to the combustion chamber. This indicates a small amplitude fluctuation in pressure is available to interact with the strong velocity fluctuations.

Based on the above conclusions from LEE for the ¼ wave and the ½ wave configurations of the combustor, it is necessary to design the combustor in a way that dimensions of both the air plenum and the combustion chamber can be easily changed. A modular design based

on a number of sections of varying lengths is chosen. Sections can be added or removed to obtain ½ wave, ¼ wave, and in-between configurations. A schematic diagram of the LDI combustor has been shown below in Figure 3.4. The combustor is mainly divided into the air inlet section, air plenum, swirler-venturi-injector assembly, combustion chamber, and the exit nozzle.

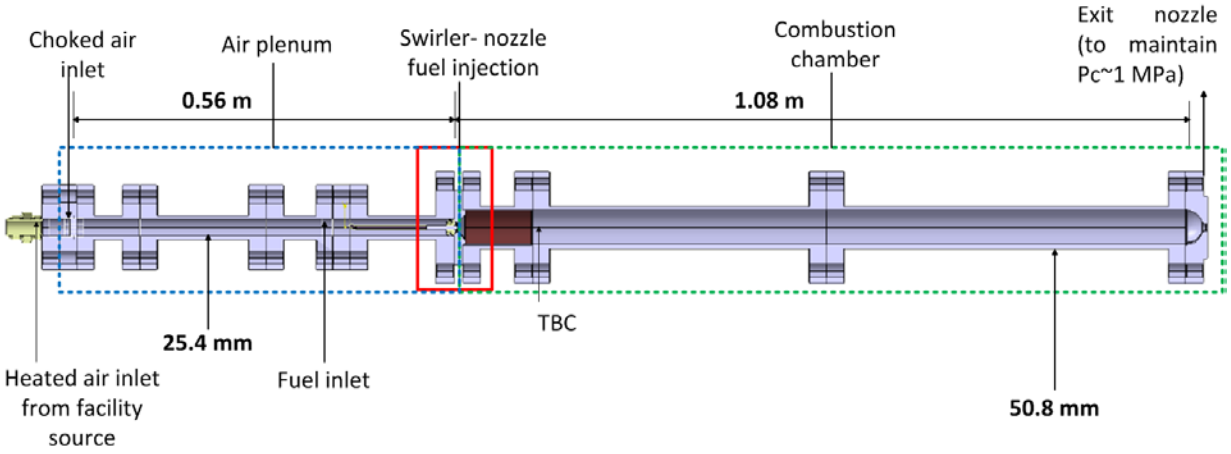

Figure 3.4. Schematic diagram of the LDI combustor

3.2.2 Combustor Design:

The design of the LDI fed combustor is based on a modular approach described above. The combustor is broken down into several elements that can be easily and quickly changed to change the configuration of the combustor. The main sections of the combustor are- the oxidizer inlet section, the air plenum, the swirler-venturi-injector assembly, the combustion chamber, and the exit nozzle. A brief description of each of these elements has been given in the following section. To meet the stated objectives of the experiment, all the sections of the combustor are equipped with ports for low frequency (up to 2 kHz) pressure transducers, high frequency (180 kHz) pressure transducers, and k-type thermocouples.

The combustor has a carbon steel construction designed to withstand steady state temperatures up to 900 K at a chamber pressure of up to 3 MPa. The experiments are typically short in duration (≤ 1min) and the chamber body acts as a heat sink for this time. The chamber is not actively cooled to avoid effects of change in wall boundary condition or addition of coolant to the flow on the chamber acoustics.

A summary of the parametric changes in the combustor in terms of its geometry and operating conditions is tabulated in Table 3.3 and illustrated in Figure 3.557. The check marks in the second and third column of the table indicate that the particular geometry combination with corresponding air plenum configuration was tested. Cross mark indicates that the geometry was not tested. The resonance for the air plenum and combustion chamber uses as a reference a 1L (first longitudinal) mode with a frequency of 350 Hz.

Table 3.3. Summary of combustor configurations and operating conditions

Geometric Parameters			Operational parameters	
Air plenum	Combustion chamber			
	1/4 wave (short combustor)	1/2 wave (long combustor)	ϕ	Tair (K)
1/4 wave	✓	✓	0.7- 0.37	650
3/8 wave	×	✓		700
1/2 wave	✓	✓		750
Full wave	×	✓		800

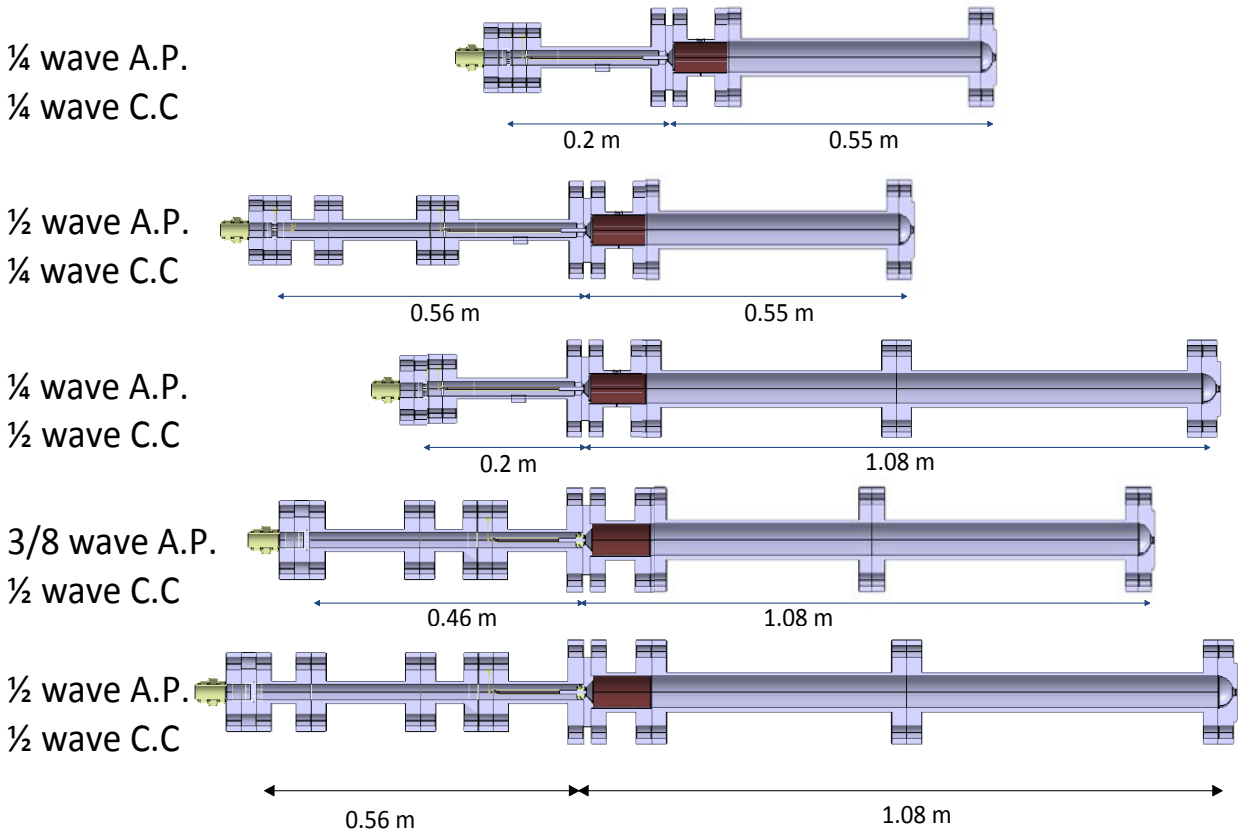

Figure 3.5. LDI combustor geometries highlighting modular design of the combustor

Figure 3.5 above shows the different combustor configurations that the LDI combustor has been tested with. The changes in lengths of the air plenum and the combustion chamber were obtained by adding or removing flanges sections of the combustor. Along with changes in combustor length, two fuel injector locations have been used for the tests. Two fuel injector locations, one at the throat of the venturi and one 2.6 mm upstream of the venturi throat, have been used.

3.2.2.1 Oxidizer Inlet Section

The oxidizer (air) inlet section has been designed in a 1” pipe 600 lb. class blind flange. The inlet is in the form of a choked orifice designed to provide a constant mass flow rate of air to the combustor. The nominal air flow rate for the experiments is 0.0816 kg/s at a temperature of 750 K. The air is provided from an electrical air heater capable of providing air at temperatures up to 922 K (1200°F). The constant flow rate through the orifices is maintained by accurately regulating the inlet air pressure. The air inlet section itself has been designed in two configurations- multiple circular orifices and slotted orifices. The slotted inlet section has also been analyzed computationally. The computational results have been attached in a separate section. Figure 3.6 below shows the two inlet section configurations. The schematic sketches of the air inlet section are shown below in Figure 19.

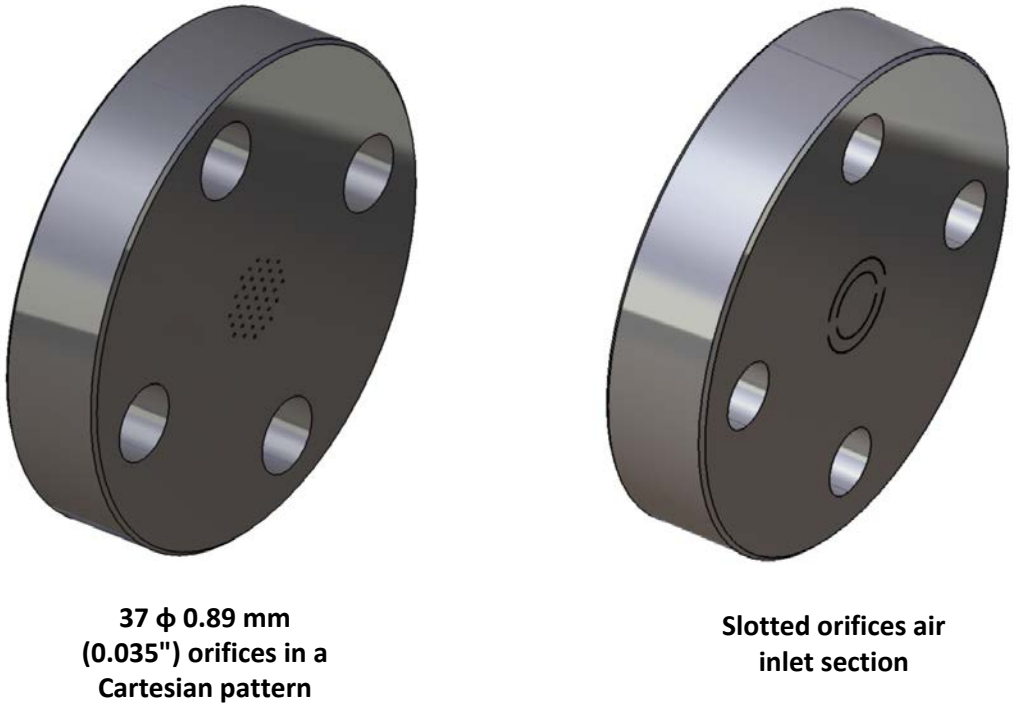

Figure 3.6. Inlet air section configurations: circular holes in a Cartesian pattern (left) and slotted choked orifices for ease of modeling (right). Both parts are machined in a 1” (25.4 mm) 600-lb blind pipe flange

3.2.2.2 Swirler-Venturi-Injector Assembly

The swirler-venturi-injector assembly is located at the exit of the air-plenum section. Two different swirler designs are available- one with a tip vane angle of 45° and the with a tip vane angle of 60°. Both the swirlers have six helically formed vanes. The fuel injector is a pressure swirl atomizer with a flow number of 0.072 mm^2 and spray cone angle of 70°. The fuel injector slips into the swirler as shown in the figure below. The exit of the swirler is located at the throat of a subsonic converging-diverging (C-D) venturi. The venturi has both, converging and diverging cone angle of 90°. The exit of the C-D venturi opens into

the combustion chamber. Figure 3.7-3.8 shows images of the C-D nozzle, swirler and the fuel injector-swirler assemblies.

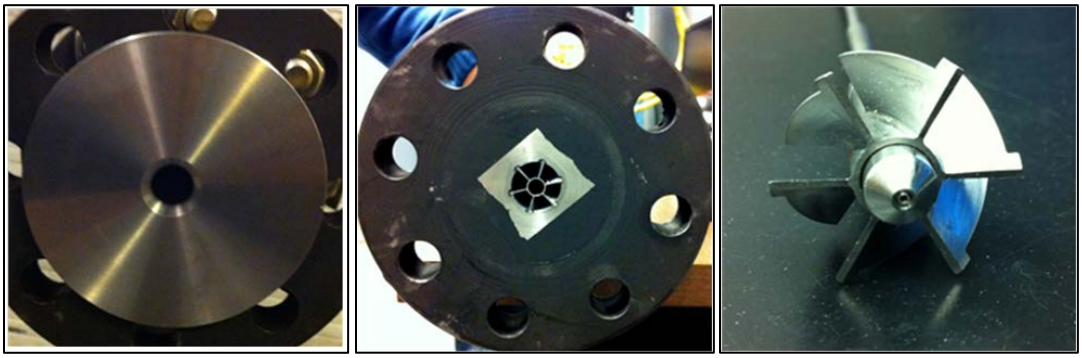

Figure 3.7. Images of the Swirler-Venturi-Injector assembly on the combustor

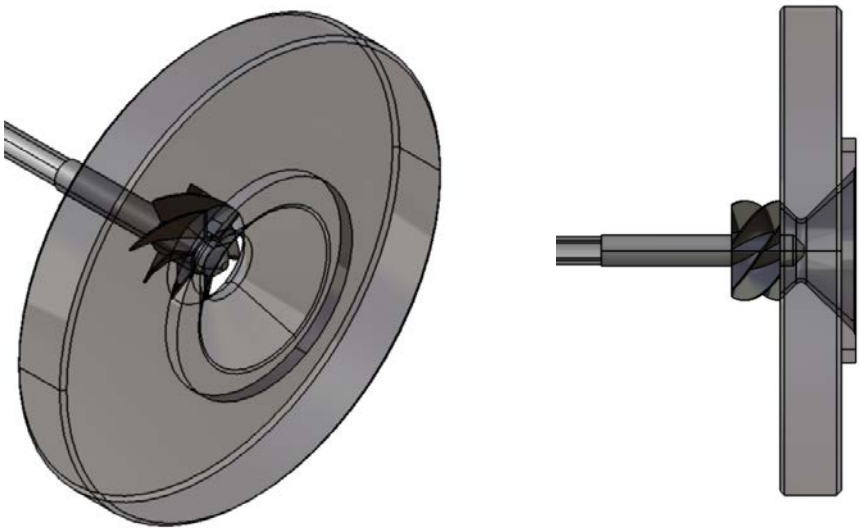

Figure 3.8. Schematic of the Swirler Venturi Injector Assembly

3.2.2.3 Air Plenum and Combustion Chamber

The air plenum shown on the left hand side of the image is made using a Schedule 80 25.4 mm pipe (1” pipe). The flanges that connect the various sections of the air plenum are 600 lb. class flanges. The total length of the air plenum is obtained from the LEE analysis and is 0.56 m (22”).The combustion chamber is made into three sections using Schedule 80 50.8 mm (2”) diameter pipe and connected using 600 lb. class flanges. The overall length of the combustion chamber is 1.08 m (42.6”). The first section of the combustion chamber is coated with a thermal barrier coating on the inner diameter. Thermal barrier coating (TBC) is used to avoid heat loss through the walls of combustor and to better simulate adiabatic boundary condition applied during computations. Use of TBC (thickness: 0.51 mm; R_a: 7.62×10^{-03} - 10.2×10^{-03} µm) will limit this change in wall boundary conditions. The TBC coating has a MoCrAl base and is made out of Yttrium stabilized Zirconia. The TBC section also houses a Champion Model AA134S-1 fuel injector which is located approximately 60 mm downstream of the fuel injector exit. Figure 3.9 below shows the installation of the combustor in the laboratory (without instrumentation installed). The combustor is mounted on a support stand made out structural box tubing.

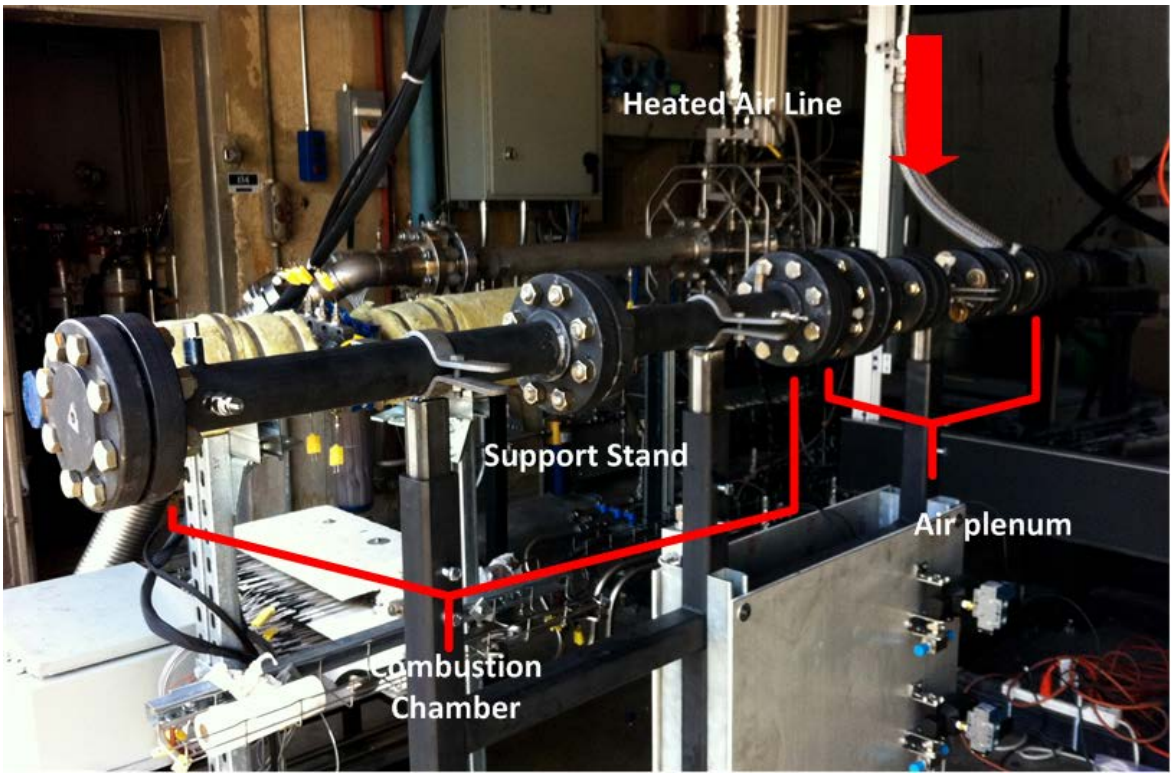

Figure 3.9. Image of the LDI combustor installation

The exit nozzle is machined into a 600 lb. class 2” (50.8 mm) pipe blind flange. The exit nozzle is choked at its throat. The throat diameter allows back pressure control of the combustion chamber to 1 MPa. The choked exit also defines the acoustic boundary condition at the exit of the LDI combustor.

3.2.2.4 Data Acquisition and Instrumentation

Safety considerations are a premium with testing with high thermal power flames and consequently all testing operations are contained in an isolated test cell and controlled from a remote location using a National Instruments (NI) LabView Virtual Instrument (.vi). The .vi has been developed and implemented for live control of the experiment and data

acquisition (this system runs at up 2 kHz). Experiment set-points, such as equivalence ratio and normalized injector pressure drop, are calculated in real time for live tuning of experimental conditions.

Sonic nozzles and cavitating venturis are used throughout the system to control and meter mass flow rates. This configuration permits very accurate control of mass flow rate by controlling the upstream pressure set-point with a closed-loop feedback controlled electronic regulator (Tescom ER-3000). In liquid systems, driven by positive displacement pumps, a back-pressure relief valve is used to control the system pressure through return loop [32, 33]. Coriolis flow meters (Micro Motion Elite CMF series) are used to measure the mass flow rates of liquid fuels. System pressures are measured using high-level output amplified pressure transducers (GE Sensing UNIK). System and experiment temperatures are measured using shielded Type-K thermocouples.

For the accurate measurement of pressure fluctuations in the combustor, a scan rate of 2 kHz is insufficient. The GE sensing transducers show an aliased frequency component for higher frequency modes superimposed on the 1 kHz spectrum. High frequency pressure data is recorded with an independent data acquisition system (recording at 180 kHz). The high frequency data acquisition system features anti-aliasing signal conditioning and a dedicated analog-to-digital converter for each channel to support simultaneous measurements from up to sixteen instruments. Piezoresistive Kulite WCT-312-35/70/100 BARA and piezoelectric PCB S112A22/ JS112A23 high frequency transducers with a sensitivity of 50-100 mV/psi are used at discrete locations on the combustor. Data from these transducers is collected at a scan rate of 100 kHz. Based on the geometric

configuration and operating condition, frequency component in the measured signal is analyzed up to 12 kHz. The transducers are mounted recessed from the combustor inner wall to avoid high thermal loading on the sensor element. The recess cavity is designed as a Helmholtz resonator with a resonant frequency that is much higher (~14 kHz) than frequencies of interest in the experiment. The transducers are located at six axial locations, three in the air plenum and three in the combustion chamber. Two transducers are located at each axial location in the combustion chamber diametrically opposite to each other for identification of modes that are not purely longitudinal in nature. Data are collected from these transducers at 100 KHz. Figure 3.10 depicts the pressure instrumentation in the combustor for the ⅜ wave air plenum and ½ wave combustion chamber configuration of the combustor (accounting for variation in sound speeds).

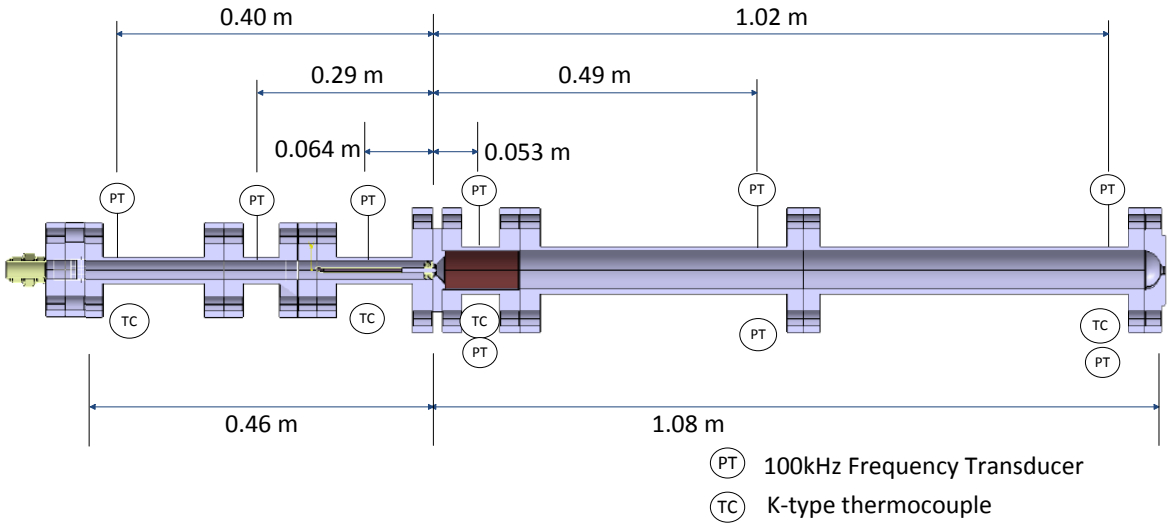

Figure 3.10: Location of pressure and temperature instrumentation on the combustor

The overall layout of the experiment in the laboratory is shown in the process and instrumentation (P&ID) in Figure 3.11 below.

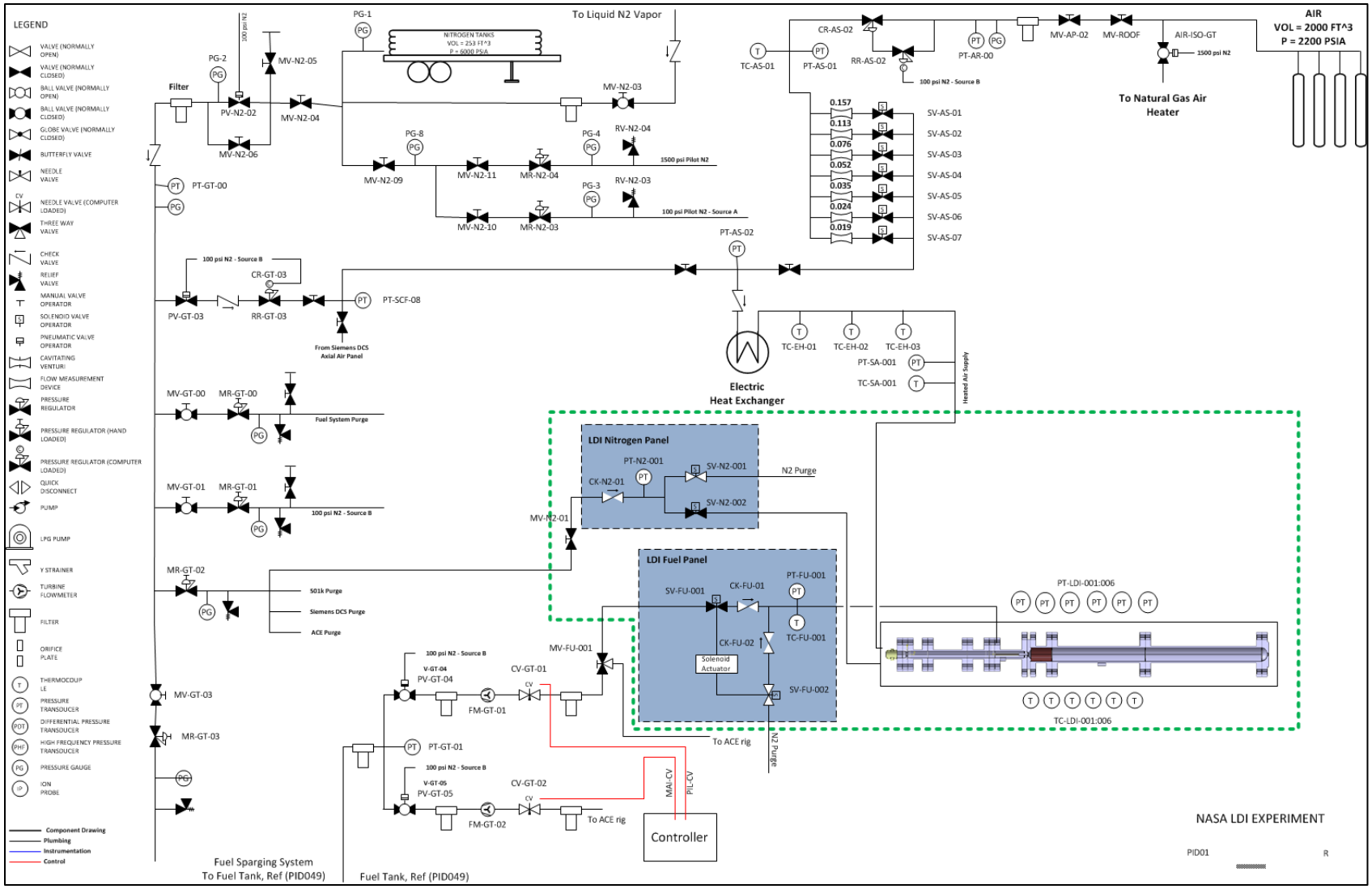

Figure 3.11. Process and instrumentation diagram for the LDI experiment

3.2.2.5 Phase 2: Optical Chamber Design

An optically accessible section of the combustor was designed to allow high repetition rate laser based diagnostic measurements, both OH PLIF and PIV at 10 kHz. Results from the simulations indicated that the active combustion was isolated to a small region in the diverging section of the venturi and immediately downstream of the combustor dump-plane. Based on this information, the optical section was designed to obtain a field of view of ~100 mm x 50 mm starting at the combustor dump plane. The flame length for all operating conditions of the combustor is approximately one chamber diameter so the field of view was sufficient to measure the flame with PLIF as well as the important flow structures with PIV. The subsonic venturi section of the combustor however was not optically accessible.

The optical chamber section was designed with a double windowed design where the inner thin quartz tube (2.5 mm thick) contains the flame. The outer quartz window is thicker (12.7 mm thick) and the cavity between the window and the tube is pressurized using 800 K hot air to maintain a cavity pressure slightly higher than the combustion chamber pressure. This double windowed configuration with a pressurized cavity minimizes the pressure and temperature gradient across the inner thin quartz tube and allows operation with a thin cylindrical tube. A thin tube will minimize optical distortion of the image due to the cylindrical surface. The entire construction of the optical chamber was made using Hastelloy-X that provides excellent strength at high temperatures. All the static seals for the assembled parts of the optical chamber were made using 1/16” thick Grafoil (99% carbon) sheets. The chamber provides optical access on four sides, of which one is used to

bring the laser sheets for OH-PLIF and PIV into the chamber, one for laser ignition and two for imaging. Schematic diagrams of the optical chamber are shown in Figures 3.12 and 3.13.

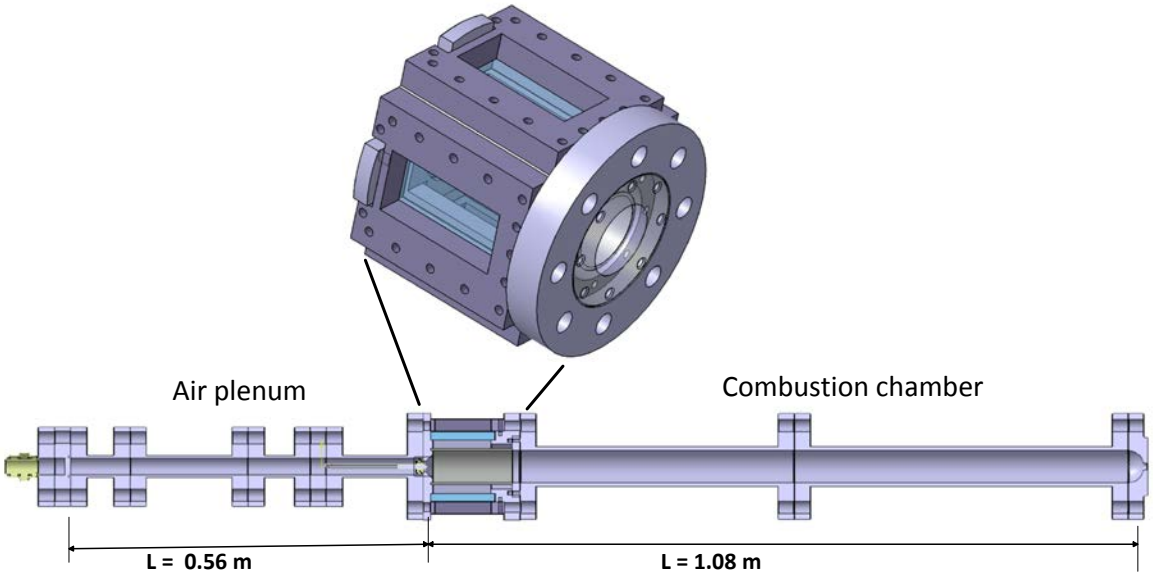

Figure 3.12: Location of the optical section on the LDI combustor

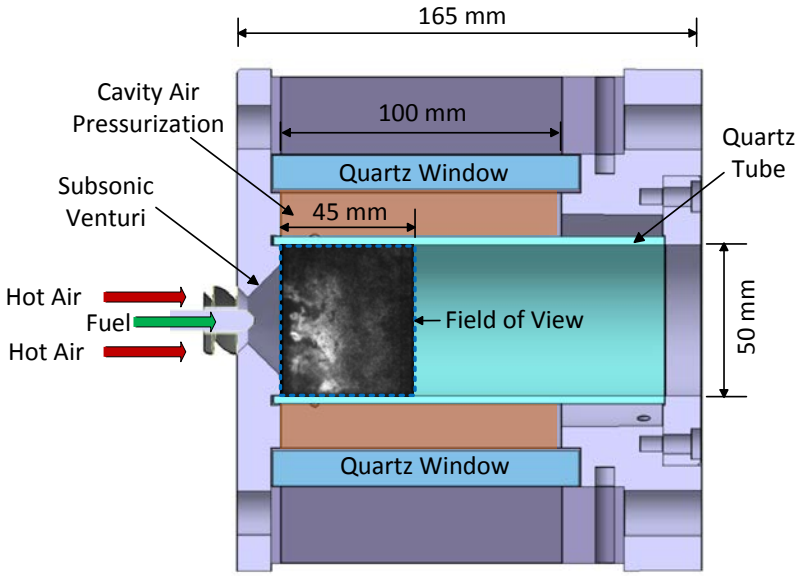

Figure 3.13: Schematic diagram of the optically accessible section of the LDI combustor

3.2.2.6 Planar Laser Induced Fluorescence Measurement (PLIF) Set-up

OH-Planar laser-induced fluorescence (OH-PLIF) is used to measure the spatial distribution of the OH-radical in reacting flows along a two-dimensional plane. In laser induced fluorescence the absorption of a temporally- and spectrally-resolved plane of light helps excite the targeted molecules in its path to an excited state through an allowed transition. The spontaneous decay of the molecules from the excited state manifold to a lower energy manifold leads to the production of the fluorescence signal that is measured. Strong intermolecular collisions can cause molecules to decay from the excited energy level back to the ground state without emission of a photon through the process of quenching. In the linear regime, the fluorescence signal is linearly proportional to the number density of the targeted species in the ground state, the rate of stimulated absorption, and the ratio of the rate of spontaneous emission from the excited state manifold to the ground state manifold to the total rate population decay from the excited state [82].

In high pressure flames, there are several effects that can lead to difficulty in performing useful PLIF measurements. The number densities of the targeted species will be greater in high-pressure flames, leading to increased signal levels. However high number densities can also lead to significant absorption and attenuation of the excitation laser sheet as it propagates through the medium [99-102]. Re-absorption of the fluorescence signal as it propagates from the probe volume, through the flame, to the detection system is a well-known effect that can also become more pronounced under high-pressure conditions [100]. Increased occurrences of collisional processes act as damping effects which broaden the

frequency width of the resonance susceptibility, reducing the peak strength of the coupling between the transition and the incident laser field.

Another measurement limitation is related to the noise characteristics of the HS-CMOS/IRO detection systems, which can be very difficult to accurately quantify [103]. In this work, the detector noise was estimated using a series of homogeneous white-field images acquired at comparable levels of signal and gain. The single-pixel noise value was established as the standard deviation of the offset-corrected white-field signal, capturing the broadband, uncorrelated sensor noise. The mean SNR for the flames was 7.55 and 6.28 for the flames at equivalence ratios of 0.6 and 0.44 respectively.

The OH-PLIF laser system used for the experiment was similar to the one used by Slabaugh et al. [104, 105] and comprised a high-repetition rate, Q-switched, DPSS Nd: YAG pump laser (Edgewave INNOSLAB IS200-2-L) and a dye laser designed for efficient operation at low pulse energies and high average power (Sirah Credo). The frequency-doubled output from the pump laser provided 7.8 mJ/pulse at 10 kHz (78 W average power) with a-9.2 ns pulse duration. Using Rhodamine 590 Perchlorate dye (dissolved in ethanol), the 566.3986-nm fundamental wavelength was frequency doubled to 283.2 nm to excite the Q1 (8) line of the $A\ ^2\sum^+ (v' = 1) \leftarrow X^2 (v'' = 0)$ transition. The average laser pulse energy at 283.2 nm was 0.68 mJ/pulse for 10 kHz operation (6.8 W average power). The first surface reflection from an uncoated fused silica window directed a small amount of the total beam energy through a Bunsen flame. The resulting LIF signal generated was collected with a photomultiplier tube and the average signal monitored with an SRS BOXCAR integrator and an oscilloscope.

The PLIF excitation sheet was formed using two cylindrical lenses ($f_{PLIF,\,1} = -25$mm, $f_{PLIF,\,2} = 300$mm) in a cylindrical telescope arrangement, resulting in a collimated sheet height of approximately 30 mm. A third cylindrical lens ($f_{PLIF,\,3} = 600$mm) was used to focus the sheet to the beam waist at the combustor centerline. The sheet width was measured by traversing a narrow slit through the sheet waist and measuring the transmitted power with a photodiode. On the combustor centerline, the sheet thickness was measured to be approximately 500 μm (FWHM). The calculated Rayleigh range for sheet waist was approximately 35 mm; therefore, it was assumed that there was minimal variation in the laser fluence across the span of the combustor. The peak laser fluence was 9×10^7 W/mm^2. The OH-PLIF signal was collected using a 100-mm focal length, *f*/2.8 objective lens (Cerco Sodern Type-2178). A multi-channel plate intensifier (LaVision HS-IRO) was used to amplify the signal, which was imaged by a high-speed CMOS camera (Phantom v411). The intensifier gate width was run at the minimum value possible (100 ns) to minimize background noise from flame luminosity. An optical band-pass filter (Semrock 320/40) was used to transmit the fluorescence from the $A\,^2\sum^+ (v' = 1) \rightarrow X^2 (v'' = 1)$ and $A\,^2\sum^+ (v' = 0) \rightarrow X^2 (v'' = 0)$ bands occurring over the 305–320 nm range of wavelengths. The effective filter width was sufficient to block the entire wavelength range of the intensifier photocathode sensitivity, removing elastic scattering of the laser beam from the seed particles and further reducing background flame luminosity. The filter had a transmission efficiency of >98 % over the selected bandwidth and an ultra-steep transmission cutoff (<1 nm). The maximum array size for the OH-PLIF CMOS camera, operating at a 10 kHz frame rate, was 543 × 585 pixels. For the field of view indicated in Figure 26, this resulted in an image resolution of 97.4 μm/pixel in the raw data images.

3.2.2.7 Particle Imaging Velocimetry (PIV) Set-up

A dual-cavity, diode-pumped, solid state Nd:YAG laser (Edgewave IS811-DE) provided 532 nm light at 4 mJ/pulse with a repetition rate 5 kHz for the PIV measurements. The beam was expanded to approximately 30 mm in height using two cylindrical lenses ($f_{PIV,\,1}$ = -25mm, $f_{PIV,\,2}$ = 300mm) in a cylindrical telescope arrangement. A third cylindrical lens ($f_{PIV,\,3}$ = 750mm) was used to focus the collimated sheet just outside of the combustor to minimize particle dropout that could occur near the beam waist. The sheet width was measured by traversing a narrow slit through the sheet waist and measuring the transmitted power with a photodiode. The inter-pulse separation time was optimized to either 2 or 4 μs based on the test condition to achieve mean particle field displacements of approximately half of the final interrogation window size. To cover the maximum dynamic range of the instantaneous velocity field an inter-frame time separation of 8 μs was chosen. A fluidized bed was used to seed TiO2 particles (250 nm nominal mean diameter) into the air plenum, approximately, five air-plenum diameters upstream of the swirler. The air-seed particle flow was heated prior to injection into the combustor to maintain air temperature at the 800 K test case. The images of the flow-field were collected through a 105 mm focal length, f/2.8 objective (Nikkor AF-S Micro) and recorded with a high-speed CMOS camera (Photron SA-4). 7000 double-frame image frames were collected per test run. Image calibrations, scaling, and particle cross-correlations were performed using the multi-pass adaptive window offset cross-correlation algorithm in the LaVision commercial software (DaVis 8.1.6). Results presented in this work were processed using a final window size of 32 x 32 pixels with 50% overlap.

A schematic diagram of PLIF and PIV optical set-up is shown in Figure 3.14 . The PLIF and PIV sheets are overlaid on each other during simultaneous measurements and individual systems are used when only PLIF or PIV measurements are performed.

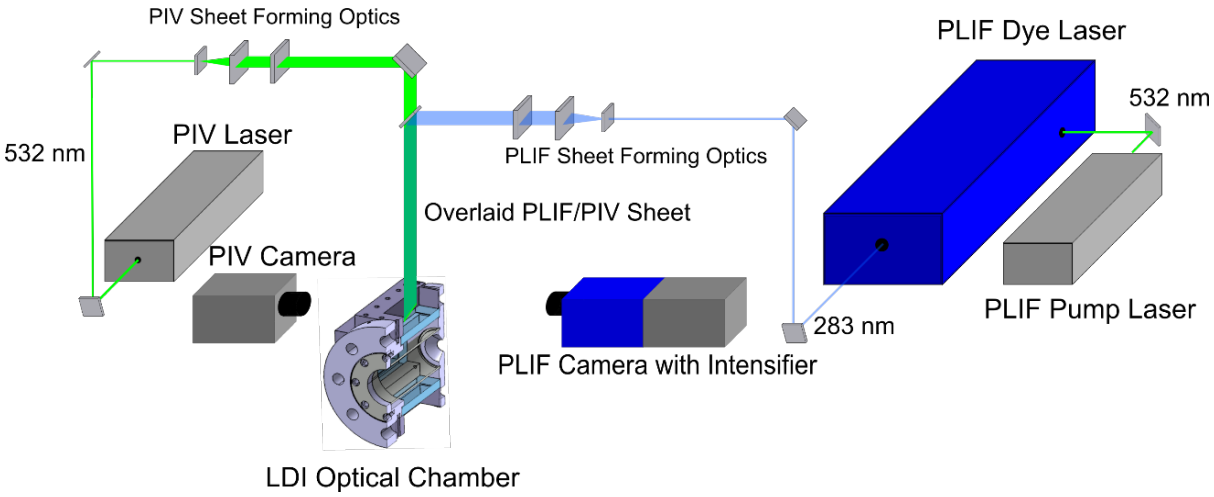

Figure 3.14. Optics and imaging set-up for the OH-PLIF and PIV measurements. Figure adapted from Slabaugh et al [104]

The field of view for the PIV measurements was severely restricted due to challenges with glare from the cylindrical quartz window used in the LDI combustor. The reflection of the 532 nm laser sheet of the curved surface was found to be near unavoidable, especially due to slight movement of the combustor during installation post calibration measurements. Half the surface of the tube was sand-blasted to obtain a near opaque face, to diffuse the reflection sheet that led to a glare with promising results, but not good enough to allow measurements of the full chamber field of view. An image of the window with the coating and a comparison of the smoke used for focusing the camera on the laser sheet are shown in Figures 3.15 and 3.16 below to highlight the improvement.

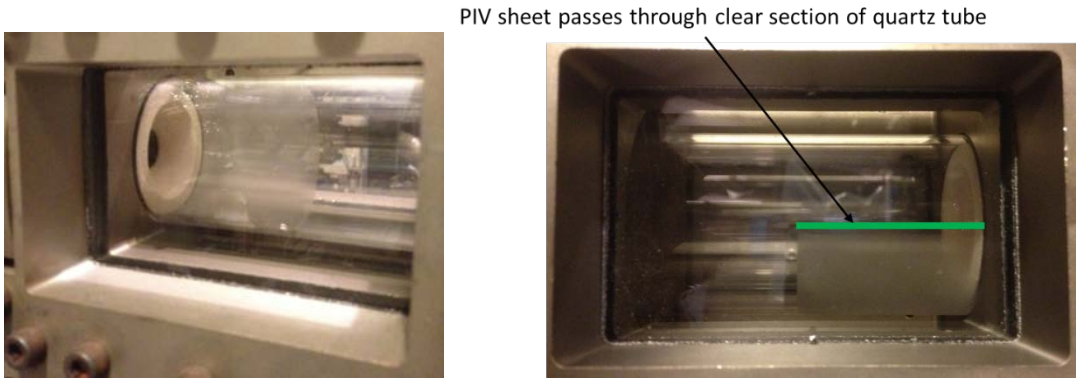

Figure 3.15. Quartz tube modification by sand-blasting one half of the tube mitigate challenges with glare from the PIV laser sheet

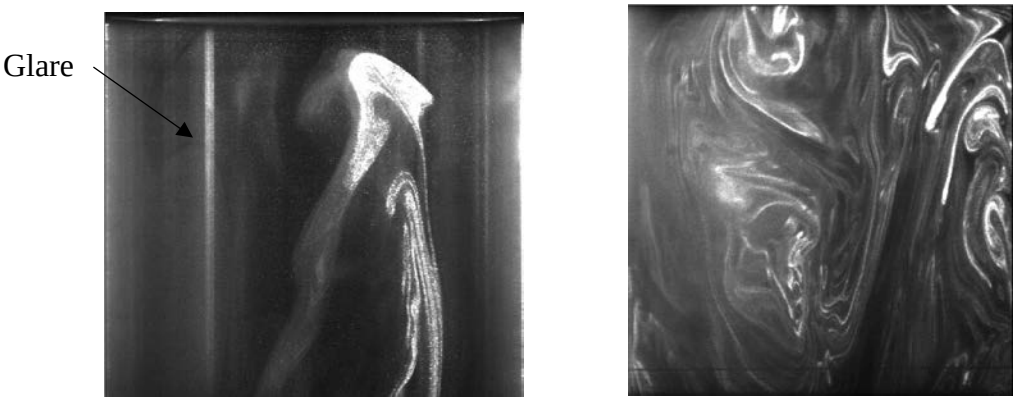

Figure 3.16. Smoke calibration images to highlight reduction in glare of quartz tube by making half the surface opaque

3.3 Summary

A high pressure single element LDI combustor capable of generating sustained self-excited axial mode combustion instabilities has been developed. The chamber operates at 1 MPa has a modular design that allows variation in geometry and acoustic resonance, inlet air temperature, equivalence ratio, injector location, and type of liquid fuel. The combustion experiment allows application of advanced optical diagnostics to the study of combustion instabilities. The combustor has been operated over a wide parameter space and a significant dataset has been generated, with over 105 tests on eight geometric

configurations. Optical diagnostics included OH-PLIF, OH* and CH* chemiluminescence, and PIV has also been applied to correlate the flame heat release with the acoustic resonance in the chamber.

CHAPTER 4. PARAMETRIC INVESTIGATION OF COMBUSTION INSTABILITIES IN A SINGLE-ELEMENT LEAN DIRECT INJECTION (LDI) COMBUSTOR

4.1 Introduction

This chapter provides a comprehensive description of the effects of combustor geometry, inlet air temperature, global equivalence ratio, fuel nozzle location and fuel composition on combustion dynamics. The well–instrumented combustor (see Fig. 3.1) was used to obtain high frequency pressure data to test and validate predictions made by high-fidelity simulations of combustion dynamics. In a parallel computational effort, large eddy simulations of this combustor [88, 89] were performed to show how swirl-acoustic interactions are realized in the subsonic venturi that result in a vortex breakdown bubble (VBB). The VBB plays a major role in the flame holding and stabilization processes that dictate the combustion response to the combustor acoustics.

These experimental results have also been previously used to test various atomization models [86, 87]. The computations highlight the influence of the spray break-up and fuel-air preparation in the subsonic venturi on the complex coupling processes between chamber acoustics, heat release, and hydrodynamics. Rapid spray break-up and droplet evaporation, and uniform fuel-air mixing is seen in stable configurations at near LBO equivalence ratios

similar to premixed gaseous flames. Unstable configurations at higher equivalence ratios show a higher degree of fluctuation in the spray break-up. The fluctuations are driven by chamber acoustics.

The design of the experimental arrangement and instrumentation is described in the first section of the chapter. Results from detailed high frequency pressure measurements in the combustor showing discriminating effects of combustor geometry, inlet air temperature, global equivalence ratio, fuel nozzle location and the fuel used are described thereafter. Results from tests in the optically-accessible chamber are presented in the next chapter. Conclusions based on the parametric study are presented at the end of the paper.

The pressure measurements show that the instabilities increase with equivalence ratio and are higher at lower inlet air temperatures. Except at the lowest levels of instability, in a certain geometric configuration and at equivalence ratios near 0.36, the dominant unstable mode consistently lies in the 1200-1600 Hz frequency range. The peak to peak pressure fluctuation amplitude (P') varies significantly with configuration, from 0.5-4% P'/Pc at a detuned combustor configuration, to as high a 20% P'/Pc in the short combustor configuration (see Fig. 3.5). A pronounced effect of fuel nozzle location on the combustion dynamics is observed, with the instabilities higher when the fuel-nozzle is at the throat of the converging-diverging venturi section of the LDI element and lower when it is upstream. A band of high frequency modes in the 5-7 kHz range are observed for most combustor configurations and operating conditions. The power spectra amplitude of this band can be comparable to the dominant longitudinal modes in the combustor. Discriminating behavior

in terms of the acoustic energy spectra is shown with changes in geometric and operational parameters to provide a quantitative data-set to test computational models.

4.2 Test Operation

A typical test takes approximately 30 s, during which time the combustor geometry, fuel nozzle location, air mass flow rate and the inlet air temperature are held constant. The test is started by introducing the fuel into the combustor and achieving at a high equivalence ratio. The flow rate of fuel is then reduced in steps of 3-5 s through the test duration to attain a range of equivalence ratios. Chamber pressure and global equivalence ratio measurements obtained during a representative test are shown in Figure 4.1. The gas temperature measured in the air plenum and 40 mm upstream of the combustor exit nozzle is shown in Figure 4.2. The test was performed at an 800 K inlet air temperature with a ⅜ wave air plenum and ½ wave combustion chamber configuration.

Ignition was obtained at the beginning of the test at ~11.1 s using a spark igniter (Champion AA134S-1) at a high equivalence ratio (ϕ~0.7) and the fuel flow rate is stepped down to lean blow-out of the flame (ϕ~0.36). At each step, the equivalence ratio is held constant for a time period of 3-5 s before the fuel flow rate is reduced to the next lower value. At lean blow-out large pressure fluctuations are observed at a very low frequency of 20-30 Hz. The pressure fluctuations that start immediately after ignition rise with an approximately exponential profile to a near limit-cycle amplitude. The temperature profile follows the equivalence ratio profile closely during the test as expected.

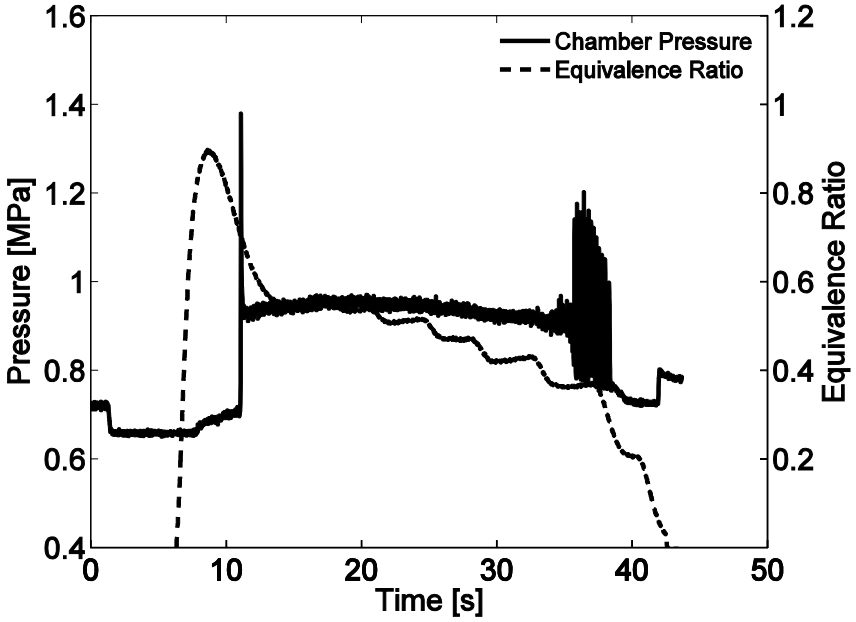

Figure 4.1: Combustion chamber pressure and global equivalence ratio during a typical LDI test

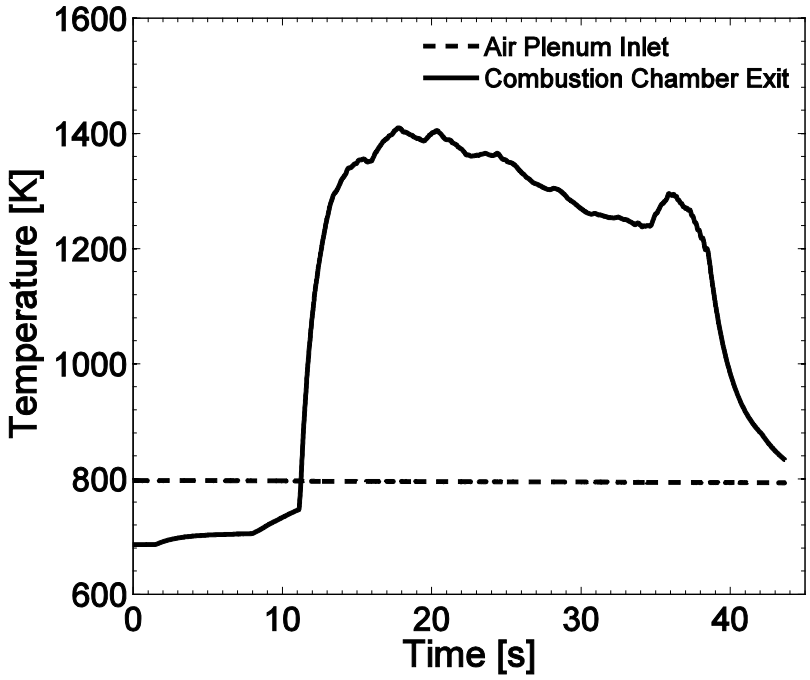

Figure 4.2: Air plenum and combustion chamber gas phase temperature during the course of a typical LDI test

4.3 Effect of Geometry on the Combustion Dynamics:

The primary method to vary the level of instability attained in the combustor was to vary the LDI combustor geometry, namely the lengths of the air plenum and the combustion chamber (see Fig. 3.5). These changes in the relative lengths of the plenum and combustor, and their absolute values, have strong effects on how the acoustic modes interact with the hydrodynamic modes and heat release modes, ultimately determining the pressure signals measured in the chamber. Figure 4.3 shows a compilation of results for all geometrical configurations of the combustor. Each data-point corresponds to pressure fluctuation amplitude obtained from band-pass filtered pressure data at dominant modes identified from power spectral density analysis for each test case.

The instability amplitudes have a significant variation with combustor configuration ranging from pressure fluctuation amplitudes of 5-80 kPa (0.5-8% P'/Pc) for the 3/8 wave air plenum- 1/2 wave combustion chamber configuration to as high as 200 kPa (~20% P'/Pc) for the 1/4 wave air plenum-1/4 wave combustion chamber configuration. Irrespective of the combustor configuration, the highest amplitudes of instability are observed at around 1200-1500 Hz suggesting that the fluid mechanics that control combustion respond strongly to pressure and velocity oscillations in this frequency range. The 3/8 wave air plenum and 1/2 wave combustion chamber was chosen as the baseline geometry for the study as it presented instabilities in the target amplitude ranges (~1%) at low equivalence ratios. Hereafter, this configuration is referred to as the baseline configuration (BL).

Concurrent simulations of the model combustor [89-91] indicated the presence of a VBB with a distinct response near 1400 Hz and a potential for strong interactions between the swirling flow and combustor thermos-acoustics. The harmonics of this frequency are also of high amplitude, peaking at an amplitude of 200 kPa (~20% P'/Pc) at 2.8 kHz for the ¼ wave A.P. - ¼ wave C.C. configuration. Another observation is the presence of high amplitude modes in the 6-8 kHz frequency range observed in all configurations at higher equivalence ratios ($\phi > 0.5$).

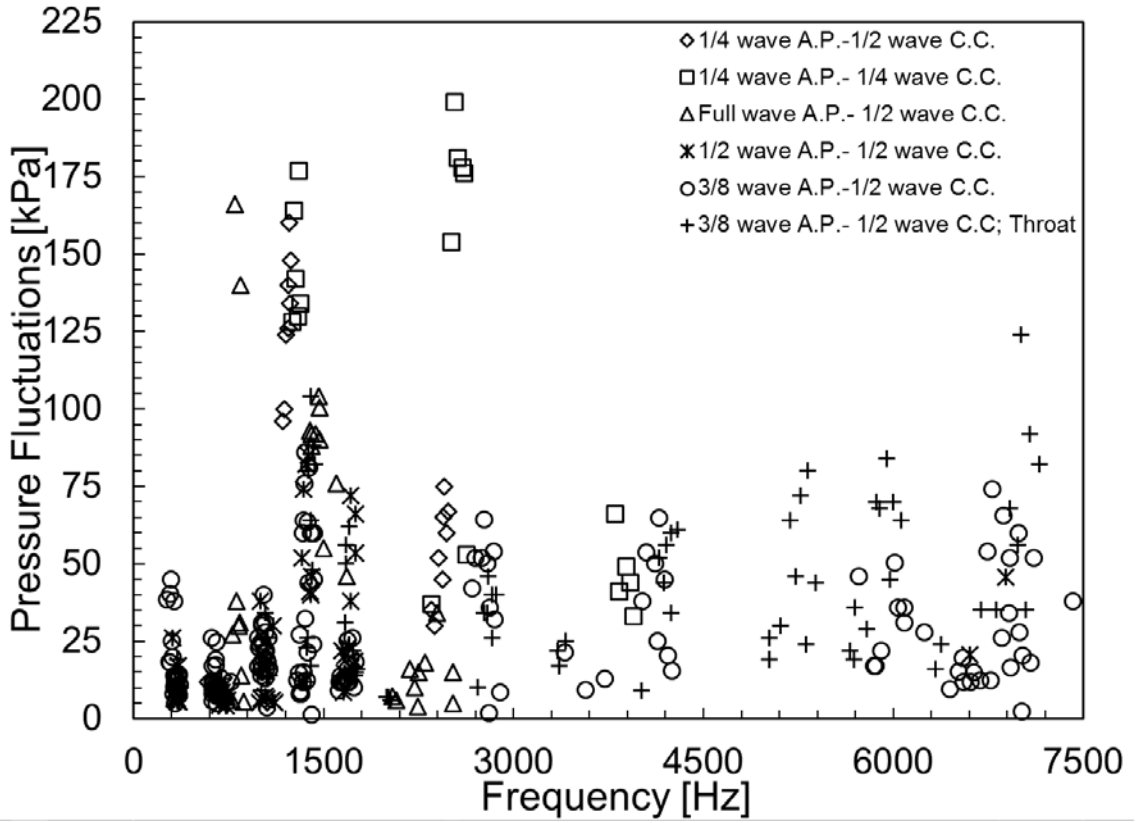

Figure 4.3: Summary of pressure fluctuation amplitudes as a function of frequency for all test configurations

To illustrate the large variation in behavior with geometry, a comparison in the pressure signals obtained between the highly unstable ¼ wave air plenum- ¼ wave combustion

chamber configuration and the moderately unstable 3/8 wave air plenum- ½ wave combustion chamber configuration is shown in Figure 4.4 below. The comparison is made using high-pass filtered pressure data and the power spectral density plots for tests run at an equivalence ratio of 0.6 and at an air temperature of 800 K. The data are high-pass filtered at 70 Hz using a Butterworth filter of 2^{nd} order to remove any electrical artifacts at 60 Hz. From the PSD plots, it can be seen that the many modes in the long-chamber configuration (b) coalesce into fewer, much stronger modes in the shorter chamber. The ~1400 Hz mode dominates both spectra; it is the 2L (full-wave) mode for the shorter combustor and the 4L mode for the longer combustor. The oscillation amplitude in the shorter combustor configuration is approximately twice that of the longer combustor configuration.

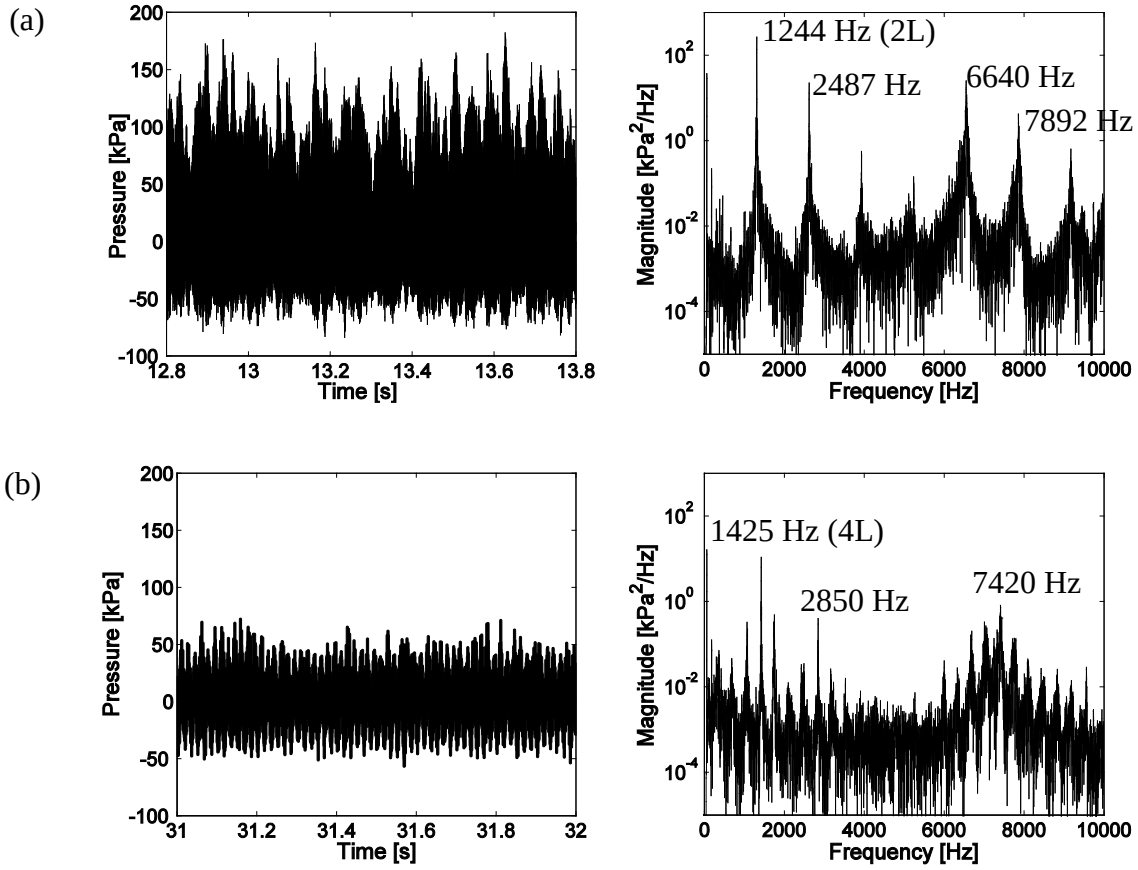

Figure 4.4: High-pass filtered pressure data and power spectral density for (a) ¼-wave air plenum, ¼-wave combustion chamber and (b) 3/8 wave air plenum, ½-wave combustion chamber configurations (ϕ~0.60, Tair=800 K). The modes around 1400 Hz (2L in ¼-wave and 4L in 3/8-wave) are dominant.

Pressure data obtained at different locations in the combustor were used to identify the pressure mode-shapes in the combustor. The measured mode-shapes were compared with those calculated using a linearized Euler equation (LEE) solver. The LEE calculation is based on a 1-D formulation and in its current application assumed a uniformly distributed hear release across the first 50 mm length of the combustion chamber and no heat transfer to the combustor walls. These simple approximations are believed to explain the disagreement between calculated mode-shapes and experimental results. The mode shapes calculated based on the experimental data agree fairly well with the LEE analysis. The

agreement validates the definition of the longitudinal pressure mode shapes and helps rank the dominant modes.

Representative plots of the mode-shape comparison for the baseline configuration, 3/8 wave air plenum, ½ wave combustion chamber are shown in Figure 4.5. The tests were performed at an inlet air temperature of 800 K and with the fuel injector 2.6 mm upstream of the venturi throat. The pressure data from two transducers located diametrically opposite to each other 0.053 m (2.1”) downstream of the venturi throat were used to calculate the phase difference between the pressure signals. For the 1L- 4L modes, the signals were in phase (±10^{o}) indicating that these modes are predominantly longitudinal. For the higher frequency modes in the 6-8 kHz range, the pressure signals were not in phase (140-160°) with each other indicating a transverse mode or tangential mode.

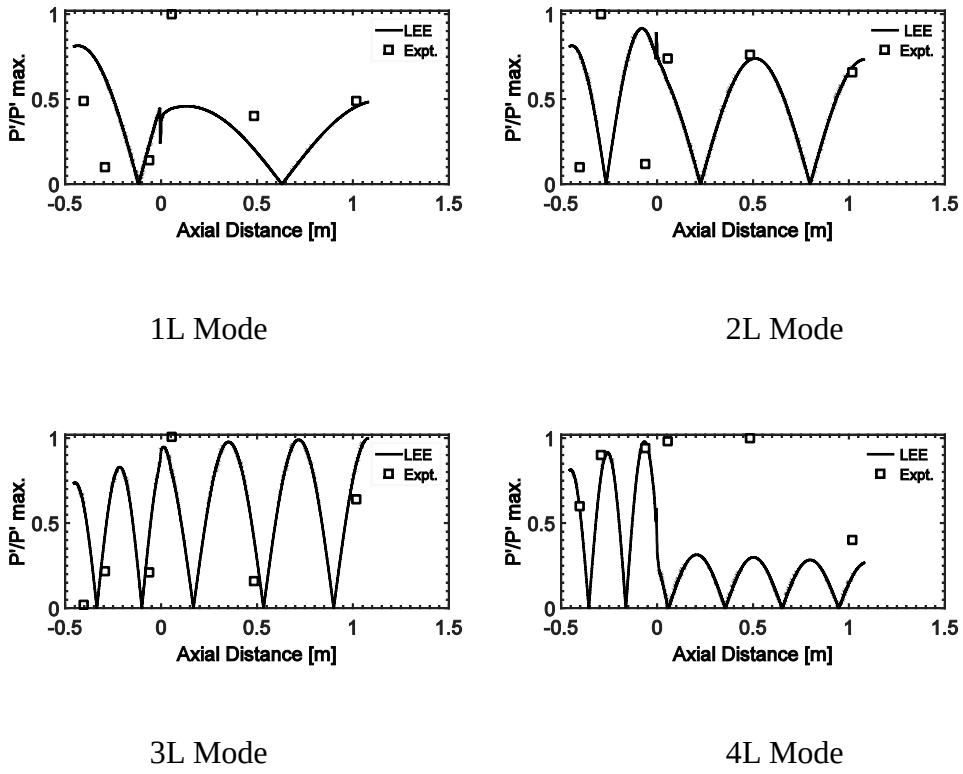

Figure 4.5: 1L- 4L mode-shape reconstruction using band-passed pressure data at multiple locations in the combustor for the baseline configuration

4.4 Effect of Operating Conditions:

4.4.1 Inlet Air Temperature

The inlet air temperature was varied in steps of 50 K from 650 K to 800 K for all the combustor configurations. For the same equivalence ratio, and air and fuel mass flow rates, the overall instability levels are typically lower at higher inlet air temperatures. Higher droplet evaporation rate at higher inlet temperatures can effect rapid and more uniform fuel-air mixing leading to a more distributed and steady flame. On the other hand, lower inlet air temperatures result in larger droplets travelling further downstream in the chamber and forming partially premixed pockets of high equivalence ratio mixtures. The maximum

instability levels are observed at an air temperature of 700 K. Figure 4.6 shows pressure fluctuation amplitudes for the 3/8 wave air plenum-1/2 wave combustion chamber as a function of the inlet air temperature for the first five longitudinal modes in the combustors. The raw pressure signal is band-pass filtered using the 2nd order Butterworth filter to obtain amplitudes at individual pressure modes. For this configuration, the 4L mode is dominant at ϕ>0.45 and the 1L mode is dominant at ϕ<0.45. The 4L mode is stronger at lower inlet air temperatures (maximum at 700 K) as shown in Figure 4.6 below whereas the trend is reversed for the 1L mode where the amplitudes are higher at higher temperatures (maximum at 750 K). The higher frequency modes (not presented in Figure 4.6 for clarity) show similar trends as the 4L mode with changes in the inlet air temperature.

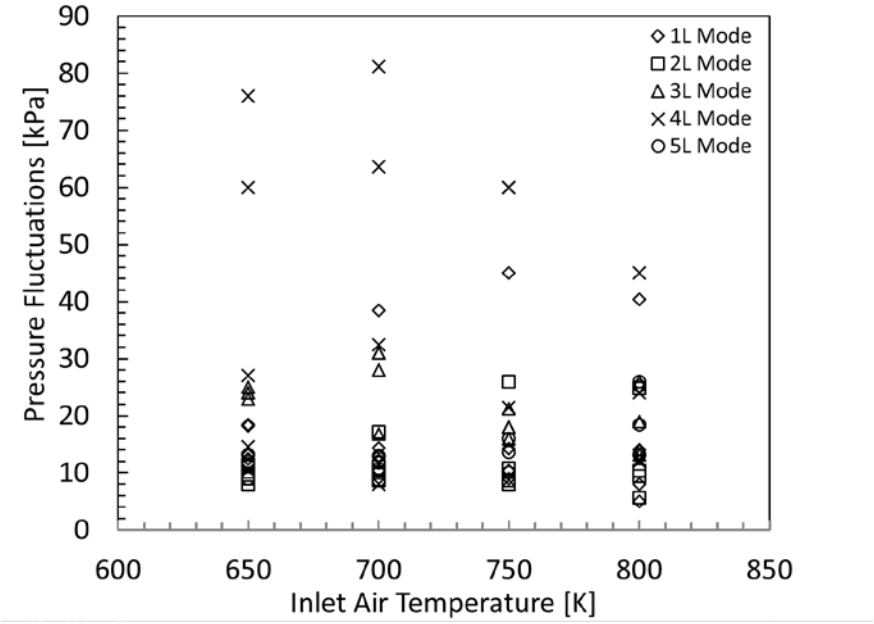

Figure 4.6: Peak to peak pressure fluctuations in the combustor as a function of inlet air temperature for the baseline configuration

4.4.2 Equivalence Ratio

Global equivalence ratio (based on fuel and air mass flow rates) in the combustor was varied during every test and data extracted at multiple time instances. Figure 4.7 shows the influence of equivalence ratio on the combustion instability in the combustor for the baseline 3/8 wave air plenum, ½-wave combustion chamber configuration. The overall instability amplitude increases with the equivalence ratio. The 4L mode is dominant at higher equivalence ratios ($\phi >$ 0.45) while the 1L and 2L modes are stronger at low equivalence ratios. Whereas at low equivalence ratios the energy is relatively evenly distributed in the first five longitudinal modes, the 4L mode dominates the spectra at equivalence ratio greater than 0.5.

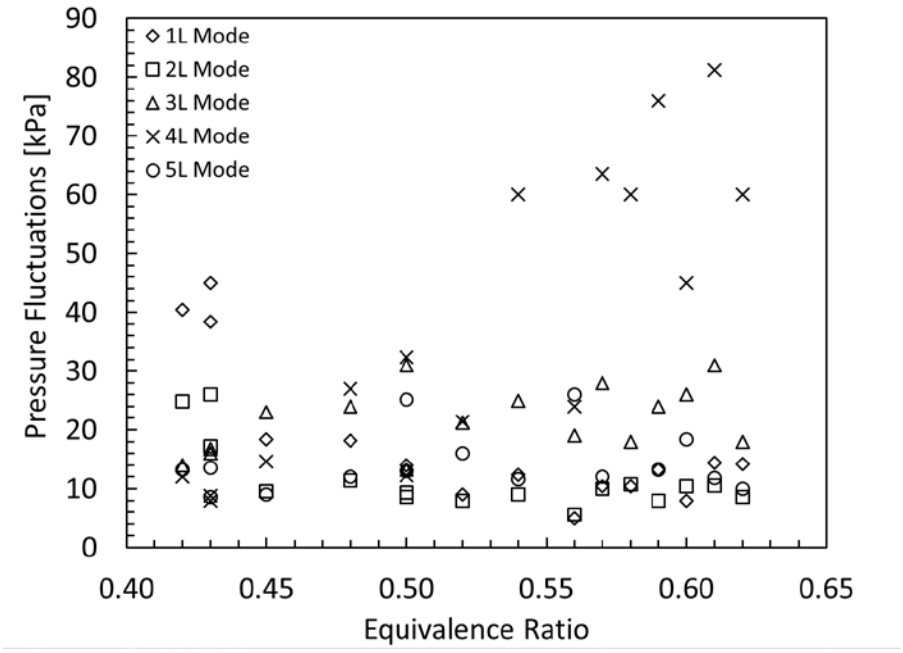

Figure 4.7: Peak to peak pressure fluctuations in the combustor as a function of global equivalence ratio for baseline configuration

4.4.3 Effect of Fuel Nozzle Location

The effect of the fuel injector location with respect to the throat of the converging-diverging venturi was measured. For the baseline configuration, the fuel nozzle at the throat was more unstable than the configuration with fuel nozzle upstream of the throat. Representative test results at an air temperature of 800 K and two equivalence ratios, 0.6 (case (a)) and 0.42 (case (b)), are used to highlight the important differences in the instabilities.

4.4.3.1 Air Inlet Temperature: 800 K, Equivalence Ratio: 0.60

Figure 4.8 compares high-pass filtered pressure data and power spectral density of the pressure data for the case (a) with the fuel injector 2.6 mm upstream of the venturi throat and (b) the fuel injector at the throat for an equivalence ratio of 0.6. The 4L mode is the dominant mode for both the fuel nozzle locations. The case with the fuel nozzle at the throat has a peak-to-peak amplitude of 82 kPa (~8% P'/P_c) while the case with the fuel nozzle upstream has an amplitude of 45 kPa at the 4L mode (~4.5% P'/P_c). Strong modes with amplitudes as high as the dominant longitudinal mode are observed in the 6-8 kHz range for both cases. The higher frequency modes have larger amplitudes (max. P'= 82 kPa) when the fuel nozzle is at the throat than when the nozzle is upstream (max. P'= 50 kPa). The 1L mode pressure fluctuations are ≤1% of mean chamber pressure.

It is speculated that a small shift of the spray injection location may result in nonlinear changes in the spray and consequently on the flame behavior. Since the velocity is greatest at the throat, any acoustics based oscillations may have a greater effect on the spray break-up. Of course the flow recirculation patterns behind the fuel nozzle may also be important.

Apparently, these differences significantly affect the distribution of fuel and possibly the hydrodynamics, and consequently the instability amplitudes and dominant pressure modes.

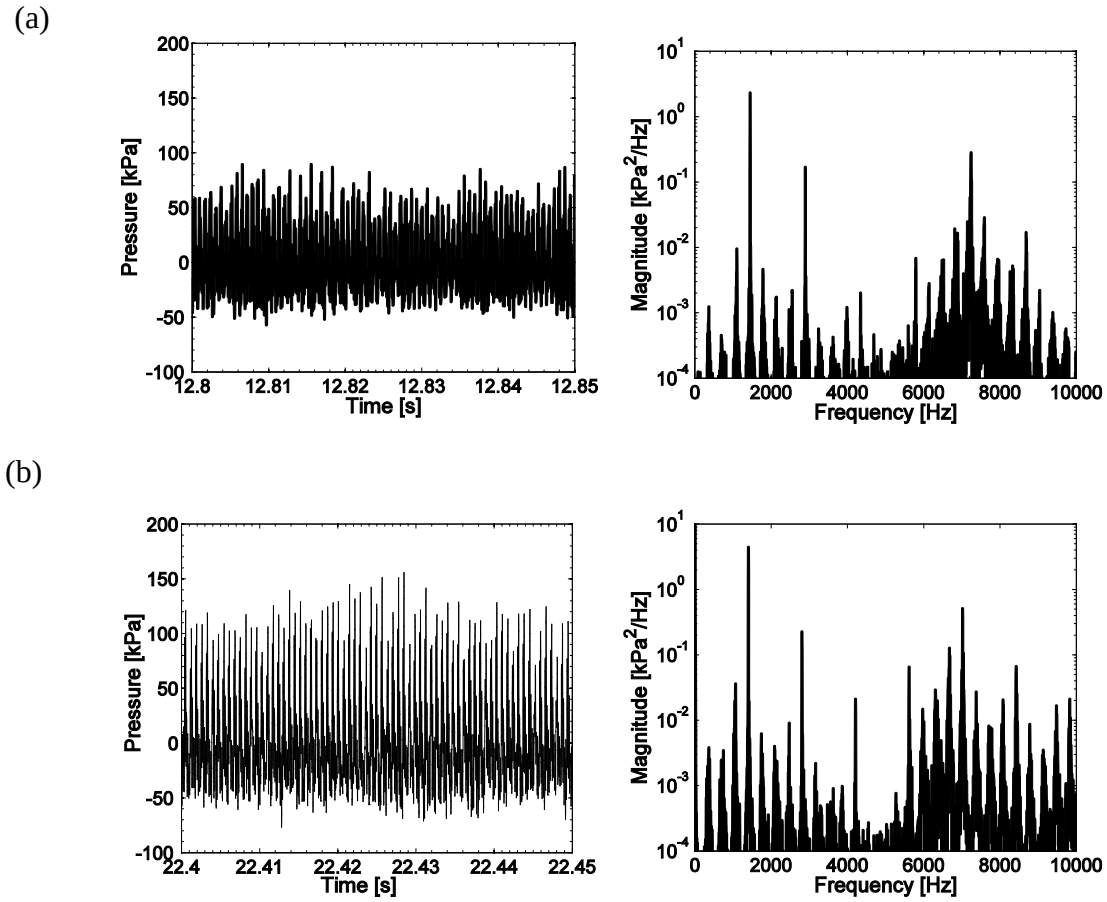

Figure 4.8: High pass filtered pressure data and power spectral density (PSD) for an equivalence ratio of 0.6 and inlet air temperature of 800 K when the fuel injector is (a) 2.6 mm upstream of the venturi throat and, (b) at the venturi throat.

4.4.3.2 Air Inlet Temperature: 800 K, Equivalence Ratio: 0.42

Figure 4.9 shows the comparison of high-pass filtered pressure data and power spectral density for the case (a) with the fuel injector 2.6 mm upstream of the venturi throat and (b) the fuel injector at the throat at an equivalence ratio of 0.42. A notable difference is seen

when the fuel injector is upstream of the venturi throat with pressure fluctuation amplitude of 40 kPa at the 1L frequency of 325 Hz. The 5L mode (1675 Hz) is the strongest mode in the combustor with pressure fluctuation amplitude of 56 kPa when the injector is located at the throat of the venturi. Based on overall pressure amplitudes, the configuration with the fuel injector at the throat is more unstable than the configuration with the injector upstream of the throat. The energy spectra for both these cases are spread across the first few modes in the combustor. This is significantly different from the behavior at higher equivalence ratios where a dominant 4L mode is observed. This absence of a strong single dominant mode suggests the presence of multiple subtle physical mechanisms participating in driving/damping the instabilities [90].

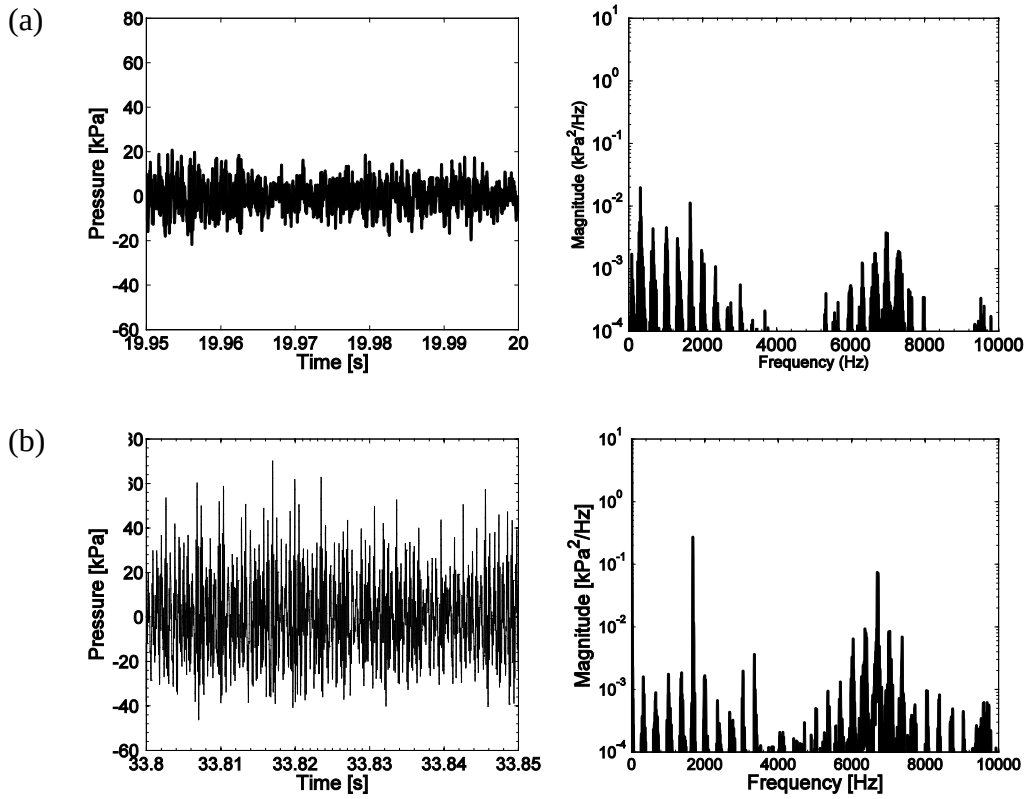

Figure 4.9: High pass filtered pressure data and power spectral density (PSD) for an equivalence ratio of 0.42 and inlet air temperature of 800 K when the fuel injector is (a) 2.6 mm upstream of the venturi throat and, (b) at the venturi throat.

4.4.4 Modulation of the Pressure Signal

A strong 4L mode is observed at a frequency of ~1400 Hz in the baseline configuration for equivalence ratios exceeding 0.45. Below this equivalence ratio, the energy is more distributed across the 1L-5L modes with significantly lower overall pressure oscillation amplitudes. For the high amplitudes (4L mode) at higher equivalence ratios, the pressure signal shows a limit cycle behavior where it reaches a stationary high amplitude. On the other hand, at lower equivalence ratios and lower pressure oscillation amplitudes, a

significant modulation of the high frequency pressure signal is observed. When short time slices are selected for analysis within these modulating periods, modes switch between the 1L-5L but remain fairly low in amplitude. This behavior is shown in Figures 4.10 and 4.11 using band-passed pressure data and power spectral density plots for the baseline configuration.

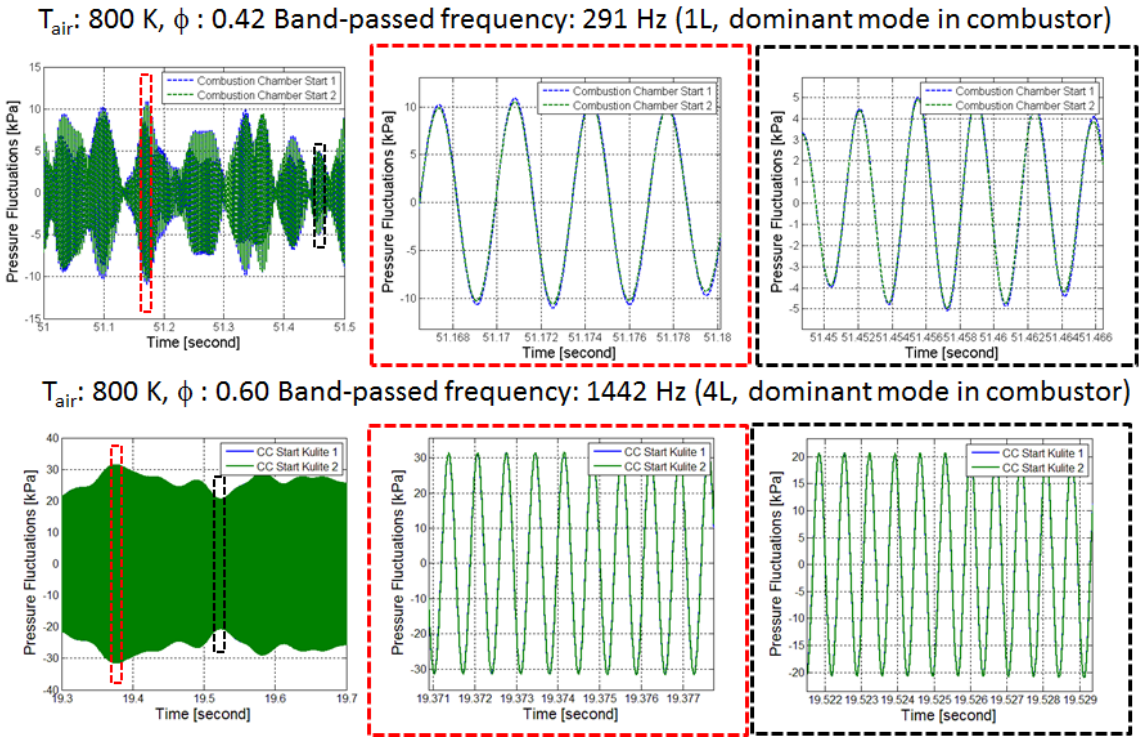

Figure 4.10: Modulation of pressure signal at low and high pressure fluctuation amplitudes in the LDI combustor for BL configuration. Note the change of scale

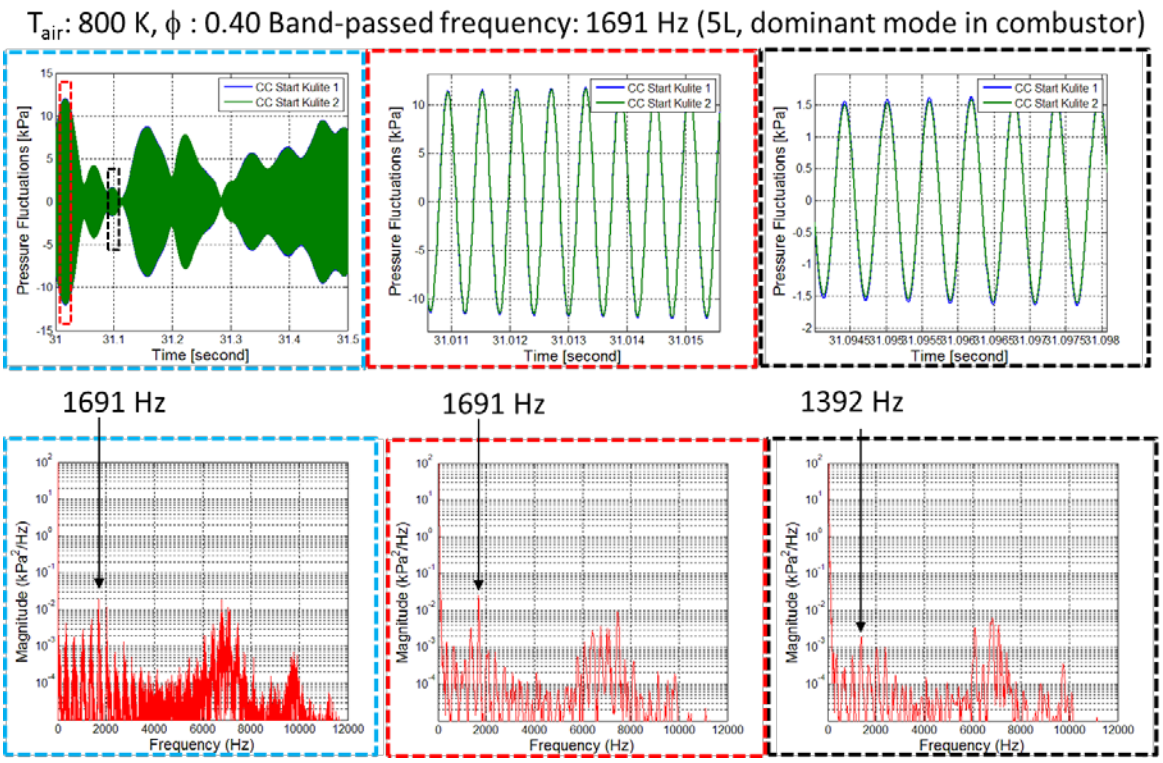

Figure 4.11. Modulation of pressure signal during the course of the test and mode-switching depending on the pressure amplitude time-slice selected. Note the change of scale.

4.4.5 Switching of Dominant Modes

During a typical test, the equivalence ratio is varied from a high value of ~0.7 to lean blow-out, and the instability levels vary significantly over the sweeps. Along with the changes in overall fluctuation amplitude, the value at each dominant mode also varies during the test. Figure 4.12 shows the variation in pressure fluctuation amplitudes for the 1L mode (325 Hz), 4L mode (1420 Hz) and the high frequency mode at 7100 Hz using band-passed data. The pressure data are band-passed filtered with a band-width of ±50 Hz and normalized using the maximum P’ value at the particular mode frequency- 15 kPa at 1L

mode, 95 kPa at 4L mode, and 80 kPa at 7100 Hz. A wide band-width is used to account for changes in the frequency with change in equivalence ratio during the test.

At ϕ >0.65, the 4L mode is clearly dominant with a steady limit cycle that is ±5% of the mean chamber pressure. Between ϕ=0.65 and 0.60, the amplitude of the 4L mode declines whereas the amplitude of modes at 7100 Hz grow until it is of similar amplitude as the 4L mode. The 4L mode amplitude decreases with ϕ and its amplitude is <1% of the chamber pressure near lean blow-out equivalence ratios. The strong correlation of the 4L mode amplitude with equivalence ratio is indicative of the preference of the combustion response to that frequency. The 1L mode is low for ϕ >0.46, below which it grows to become the dominant mode. The increase in the 1L mode amplitude coincides with the reduction in amplitudes of the 4L mode and the 7100 Hz mode.

The distinctive behavior of the dominant combustor modes as a function of equivalence ratio are due to changes in the flame shape, hydrodynamics and the interactions between them. Results from the simulations show that the physical mechanisms that drive each mode are highly dependent on the equivalence ratio, which determine drop-size and fuel distribution [88, 90].

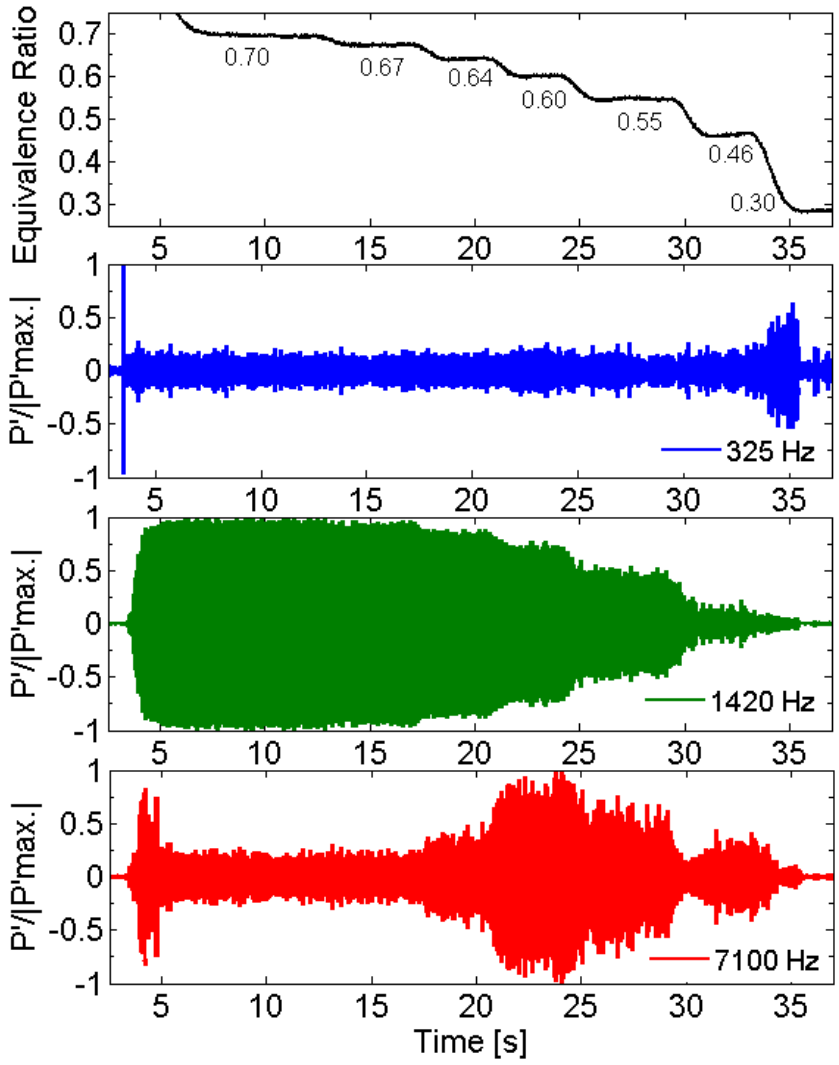

Figure 4.12: Equivalence ratio and band-passed pressure data (±50 Hz band-width) at the 1L, 4L and the 7 kHz frequencies for test performed at 800 K in the baseline configuration (fuel nozzle at throat)

4.4.6 Effect of Fuel Composition

The LDI combustor was operated using two fuels, Jet-A and a Fischer-Tropsch synthesis based synthetic paraffinic kerosene (FT-SPK) procured from Petro-SA. Table 4.1 compares the major properties of the fuels that were used in the tests. The major difference between the two fuels is the negligible amount of aromatics present in the FT-SPK fuel.

The lack of aromatics in the fuel was preferred in the tests where OH-PLIF measurements were performed, so the fuel fluorescence at wavelengths similar to OH-fluorescence was avoided.

Table 4.1: Comparison of physical properties between Jet-A and FT-SPK fuels

Property	Phillips 66 Jet A	PetroSA PS 150
Density [kg/m^3] (at 293 K)	775-840	765
Kinematic Viscosity [cm^2/s]	0.015-0.025	0.016
Flash Point [K]	310-338	340
Vapor Pressure [kPa] (at 293 K)	0.0533	0.06
Auto-ignition Temperature [K]	483	500
Aromatic Content	18%-20%(25% max)	0.006%(0.05% max)

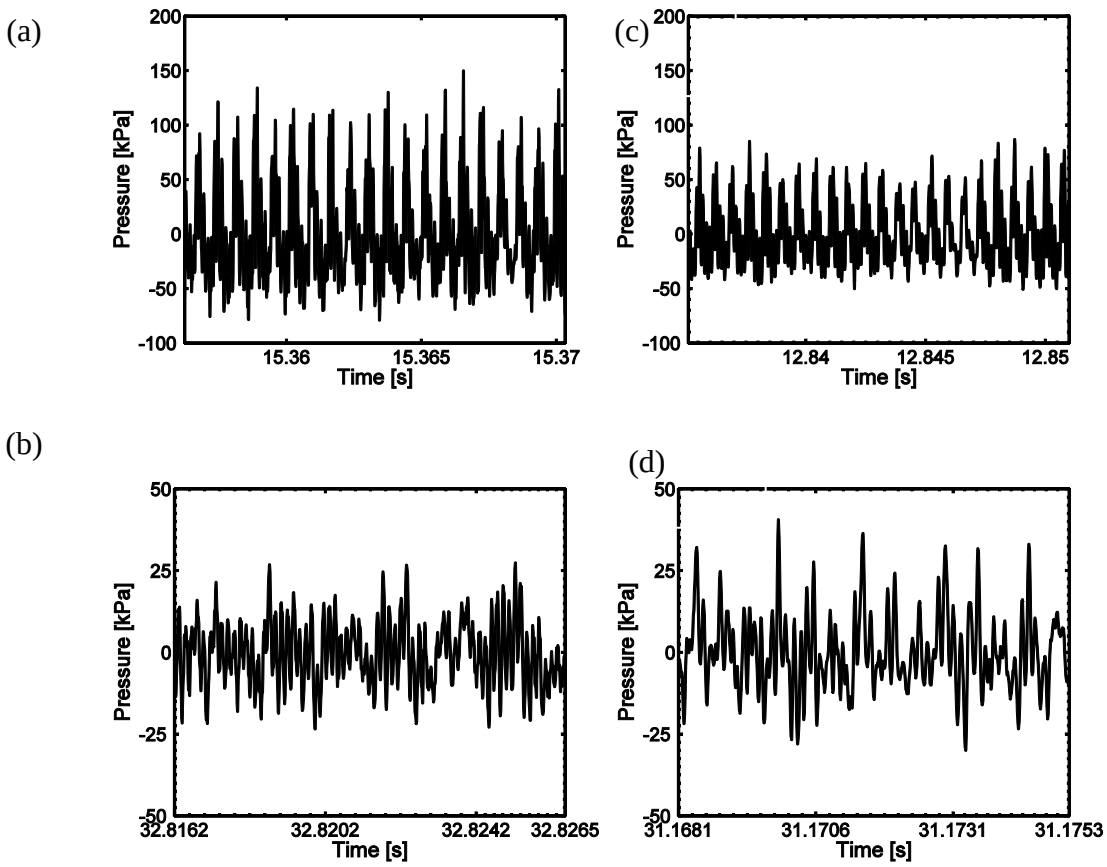

Figure 4.13: High-pass pressure data for tests performed using FT-SPK at Tair = 800 K ((a) ϕ=0.6 and (b) ϕ=0.37) and using Jet-A ((c) ϕ=0.6 and (d) ϕ=0.37) as the fuels in the 3/8 wave air plenum - 1/2 wave combustion chamber configuration.

The combustion dynamics behavior for the two fuels show distinct differences as the air temperature and equivalence ratio is changed. Instability results with FT-SPK fuel show more stable behavior of the LDI element at lower equivalence ratios ($\phi < 0.45$) and more unstable behavior at higher equivalence ratios ($0.46<\phi<0.66$) than corresponding tests performed using Jet-A. The dominant modes at different equivalence ratios regimes remain similar for the fuels. The 4L mode and its harmonics are dominant at higher equivalence ratios. The modes in the 7 kHz range remain as strong as the dominant longitudinal modes. For the lower equivalence ratio range near lean blow-out ($\phi < 0.45$) the energy is distributed

in the 1L-5L modes and the amplitudes are significantly lower than at a higher equivalence ratio.

Figure 4.13 shows a comparison of the high-pass filtered pressure data for FT-SPK (figures (a) and (b) on the left) and Jet-A (figures (c) and (d) on the right). The tests were performed in a 3/8 wave air plenum-1/2 wave combustion chamber configuration with the fuel nozzle 2.6 mm upstream of the venturi throat. The amplitudes with FT-SPK are higher at higher equivalence ratio of 0.6 than Jet-A while they are lower near lean blow-out at ϕ=0.37. A similar trend is observed for other inlet air temperatures as well. This short study highlights the necessity of detailed study of the effect of fuel composition, especially for liquid fuels, on combustion instabilities in combustors.

4.5 Spray Characterization

Efficient atomization of the fuel spray and its mixing and vaporization in the heated air stream is an essential to the success of the LDI low NOx concept. Modeling of the spray forms an integral part of the concurrent computational effort to this experimental work. In addition to combustion experiments, a cold-flow test campaign was run to obtain the modeling constants for this computational work.

4.5.1 Experimental Arrangement

A pressure swirl atomizer (0.072 mm^2) obtained from Woodward has been used for the spray characterization tests. Phase Doppler Anemometry (PDA) and high speed videos are used to characterize drop sizes, velocities, and spray cone angle. For the spray, the fuel flow rate was maintained at the same values as the combustion experiments for equivalence

ratios of 0.4, 0.5, and 0.6. The spray tests were performed at atmospheric pressure with and without a co-flow of air around the fuel injector. The fuel flow rate is measured across a cavitating venturi (0.64 mm throat diameter) and verified based on the pressure differential across the injector. For experiments with co-flow of air, the air flow rate is regulated to maintain a ΔP/P of 4% across the injector which is similar in value measured during the combustion experiments. The air co-flow passes through the swirler and the subsonic venturi. The swirler has six helical axial vanes with a lead angle of 60° leading to a geometric swirl number of approximately 0.8. A schematic diagram of the test arrangement is attached below in Figure 4.14.

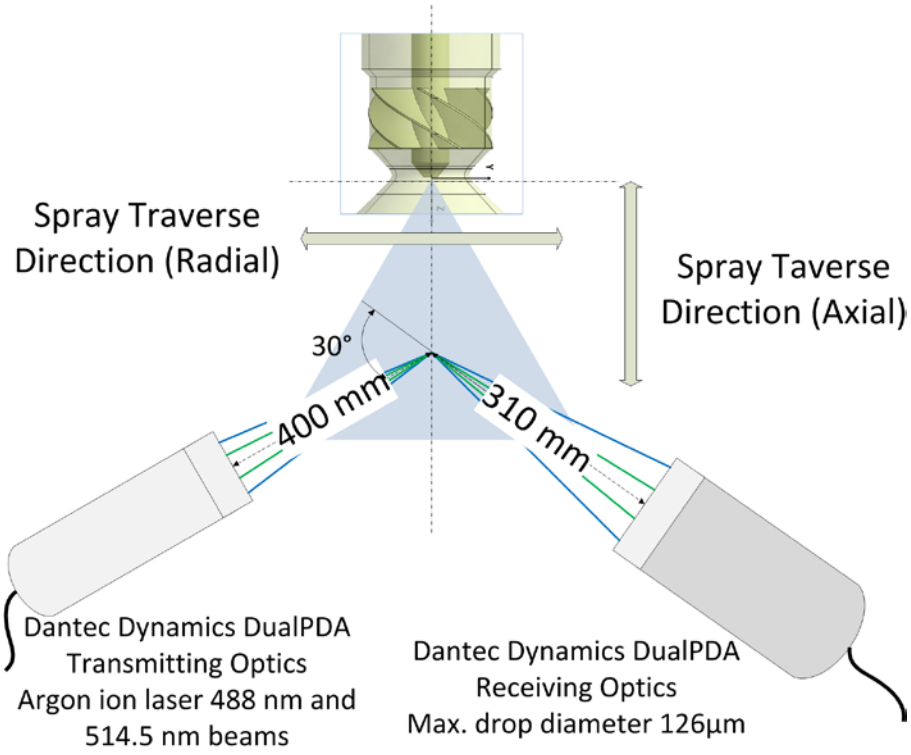

Figure 4.14. Schematic diagram of PDA test arrangement

Drop sizes and velocities were recorded with a phase Doppler anemometer (PDPA). The PDPA determines the velocity of individual particles based on the frequency shift of light which is reflected or refracted by a moving particle. The phase shift between the signal from the detectors at know spatial locations are directly proportional to the drop-sizes. For the results reported here, a Dantec Dynamics Dual-PDPA system was utilized. This system uses an argon-ion laser, beam splitter (514.5 and 488.0 nm wavelengths), and transmitter (400 mm focal length) to create orthogonal measurement volumes for simultaneous recording of two velocity components. The receiver (310 mm focal length) was placed at a scattering angle of 60 degrees, resulting in a theoretical maximum detectable drop diameter of 126 μm, as reported by the PDPA software. To capture the local statistics, 10000 to 20,000 individual drops were recorded based on the measurement location (10000 where data rate was low). Data rates (20–4300 Hz) and spherical validation values (90–100%) varied depending upon the operating conditions and measurement locations.

High speed visible imaging was used to visualize the spray. A high-speed visible camera (Vision Research Phantom v7) with a 105 mm lens was mounted perpendicular to the spray axis, and a 150 W light source and diffuser plate were positioned behind the spray to provide backlighting. The spatial resolution of the visible intensity measurements was 167 μm for each pixel at the center of the spray. For the spray measurements, the uncertainty in measurement location in the spray was approximately ±1 mm for both axial and radial traverses. The two decimal point significant digits on the plots are on account of conversion of units from inches in the physical measurement to SI units. The fuel flow rate was measured across a choked venturi of known co-efficient of discharge. The uncertainty in

measurement in the flow rate of fuel was at most 3%. The flow rate of air was set based on pressure drop across the pressure swirl atomizer. This measurement was made using a differential pressure gauge with an uncertainty of 0.83 kPa (0.12 psid).

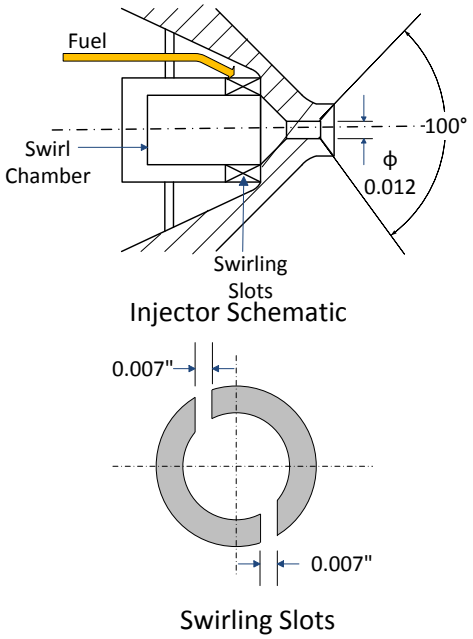

Figure 4.15 Geometrical details of the pressure swirl atomizer used in the study

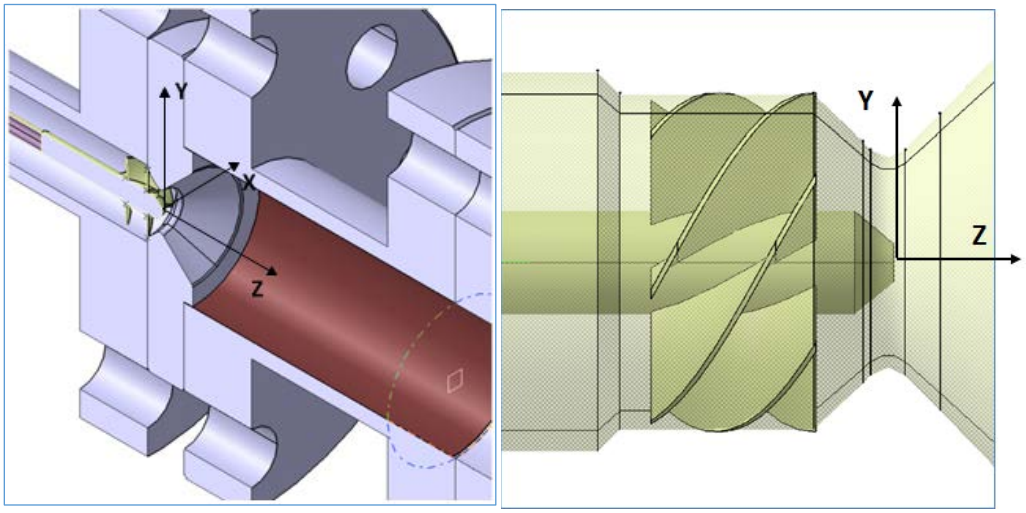

Figure 4.16 Schematic diagram of the fuel-injector-swirler-venturi configuration

4.5.2 Results and Discussion

A brief summary of results from the cold-flow spray characterization experiments in presented below. Results from the tests with no co-flow around the injector are presented first followed by a discussion of results with cold-flow.

4.5.2.1 Spray Measurements without Co-Flow Air

A snapshot from the high speed video taken from the experiment is shown in Figure 4.17. The spray-cone angle determined based on image data shows good agreement (~6%) with computational results. The spray cone angle values measured based on the images are tabulated in Table 4.2 below.

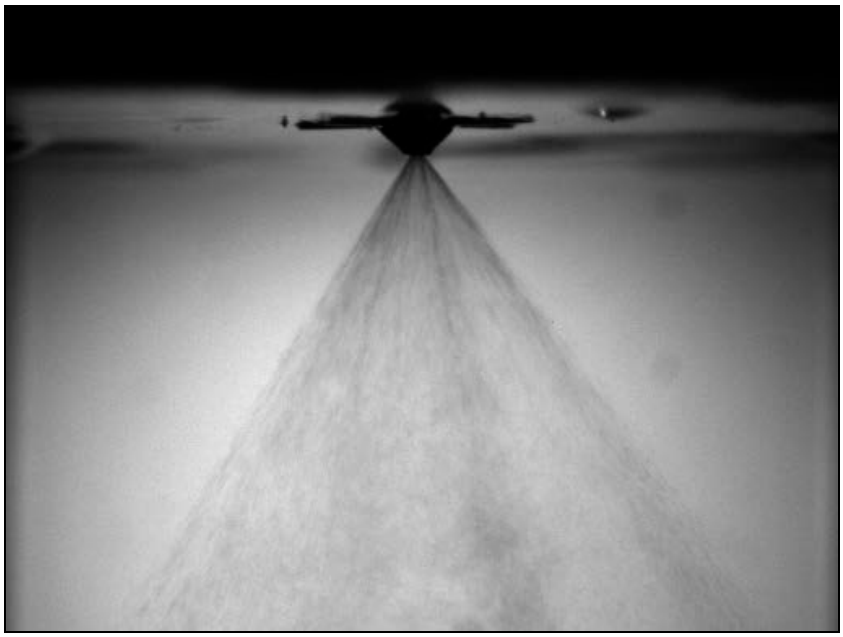

Figure 4.17 High Speed image of spray without co-flow of air. Flow number of the pressure swirl atomizer was 0.072 mm^2

Table.4.2 Spray cone angle determined experimentally based on high speed imaging data (no air co-flow)

$\dot{m}_f$ (g/s)	ϕ	θ (deg)
2.27	0.4	70
2.84	0.5	69
3.35	0.6	68

Drop size distribution and axial velocity profiles based PDA measurements are presented in Figure 4.18. The measurements have been conducted at multiple radial locations in the spray at three axial planes. The z-direction as shown is in the axial direction of the spray with the origin being at the exit tip of the atomizer. The drop-sizes characterized by the Sauter Mean Diameter (SMD, D_{32}) lie between 20-50μm.

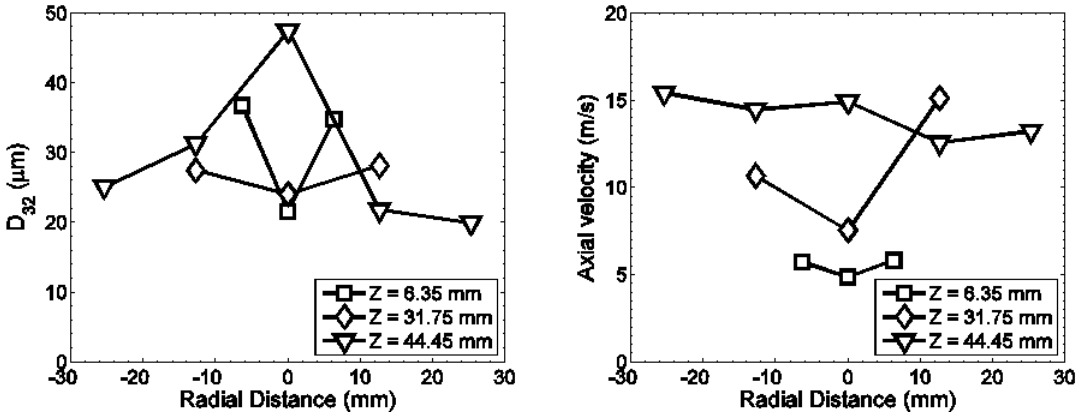

Figure 4.18. D_{32} (SMD) and mean axial velocity for PDA measurements at different locations in the spray. Jet-A flow rate 2.7 g/s

4.5.2.2 Spray Modeling and Measurement with Co-Flow Air

The fuel spray measurements have also been conducted with a co-flow of air around the injector. The spirally distorted and spinning motion of the spray is observed in the experiment. An image from the high speed video of the spray is shown below in Figure 4.19. The fuel injector tip is located approximately 15 mm upstream of the venturi exit which is visible in the image.

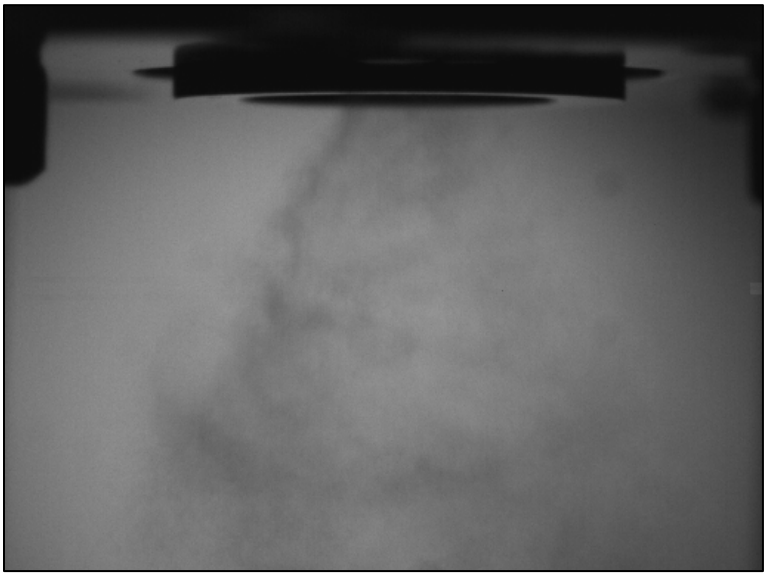

Figure 4.19. High Speed image of spray with co-flow of air

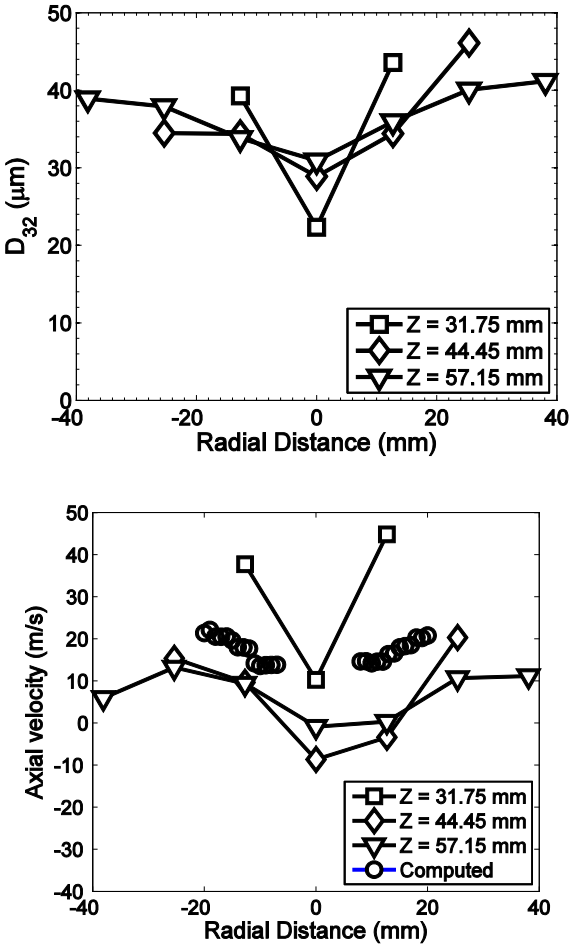

Figure 4.20. D_{32} (SMD) and mean axial velocity for PDA measurements at different locations in the spray. Jet-A flow rate 2.7 g/s. ΔP/P 4%

Drop size distribution and axial velocity profiles for the spray with co-flowing air are presented in Figure 4.20. It is important to note that the axial slices at which measurements were made are different than the case with no co-flow of air because the region covered by the venturi was not accessible. The overall level of drop size for the spray with co-flowing air is between 30–40 μm. The drop-sizes for axial locations 44.8 mm and 57.1 mm are of the same order. The drop-size right downstream of the nozzle is smallest (~20μm). The co-flowing air reduces the relative velocity between the fuel drops and the air so that the larger

drops are produced. As indicated, larger axial velocity profile is shown at the near-nozzle plane, Z = 31.8 mm. It is also noteworthy to observe the backflow in the middle at Z = 44.8 and 57.1 mm. The swirl number of the jet in this experimental set-up is approximately 0.8. For such high swirl numbers, a central toroidal recirculation zone (CTRZ) is commonly observed on account of adverse axial pressure gradients exceeding the inertial forces of droplets leading to reversal in flow. Based on axial velocity distribution, the second plane, Z = 44.4 mm, is the stagnation point and the third plane, Z = 57.1 mm, is located in the CTRZ.

A compilation of spray measurements at other equivalence ratios, with and without a co-flow of air are presented below.

4.5.2.1. Compilation of Spray Characterization Results

Spray Measurements without co-flowing air:

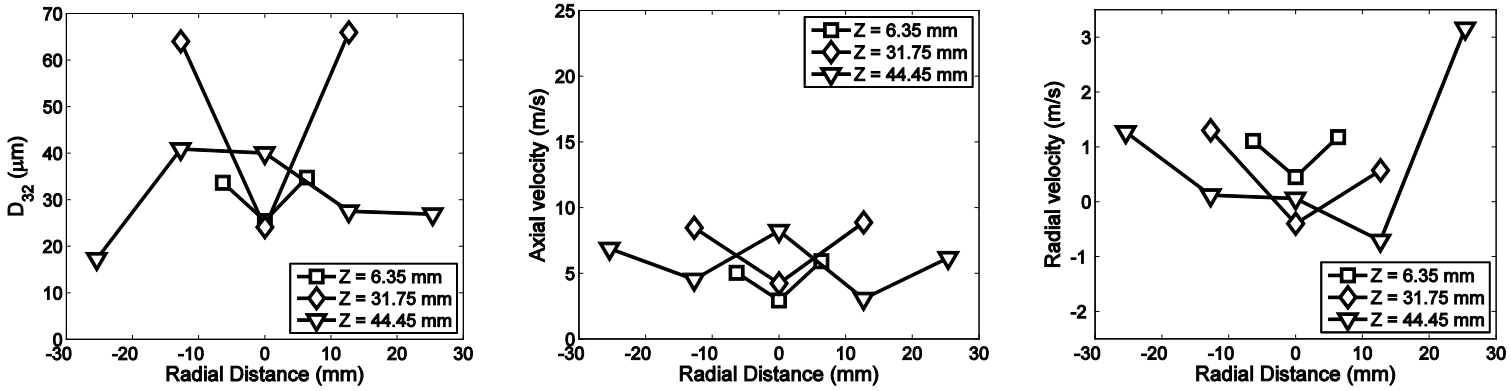

Figure 4.21 D_{32}, axial velocity and radial velocity in spray at equivalence ratio of 0.40 without co-flow of air

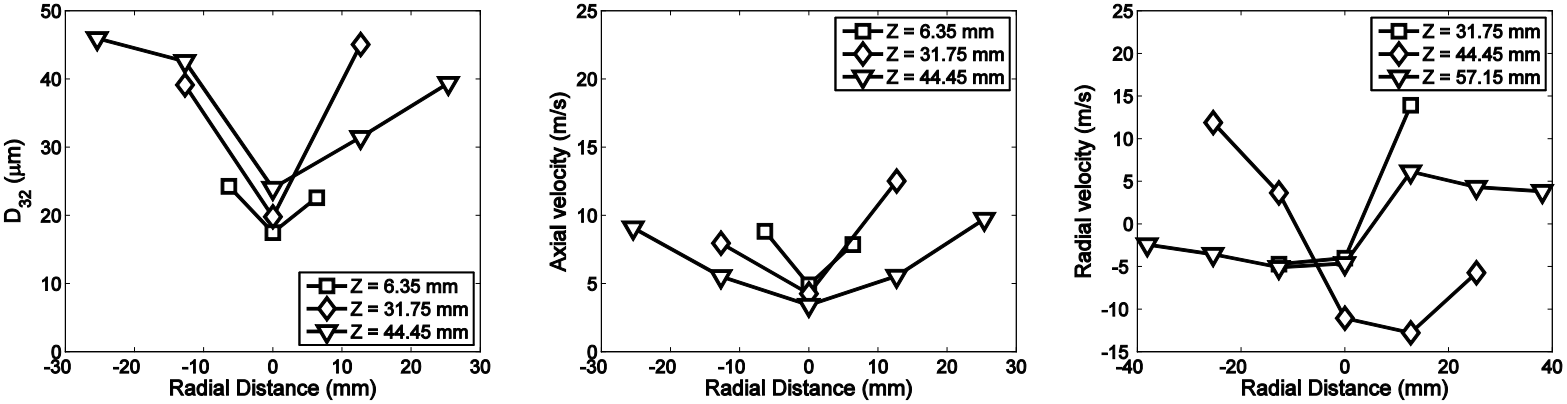

Figure 4.22 D_{32}, axial velocity and radial velocity in spray at equivalence ratio of 0.50 without co-flow of air

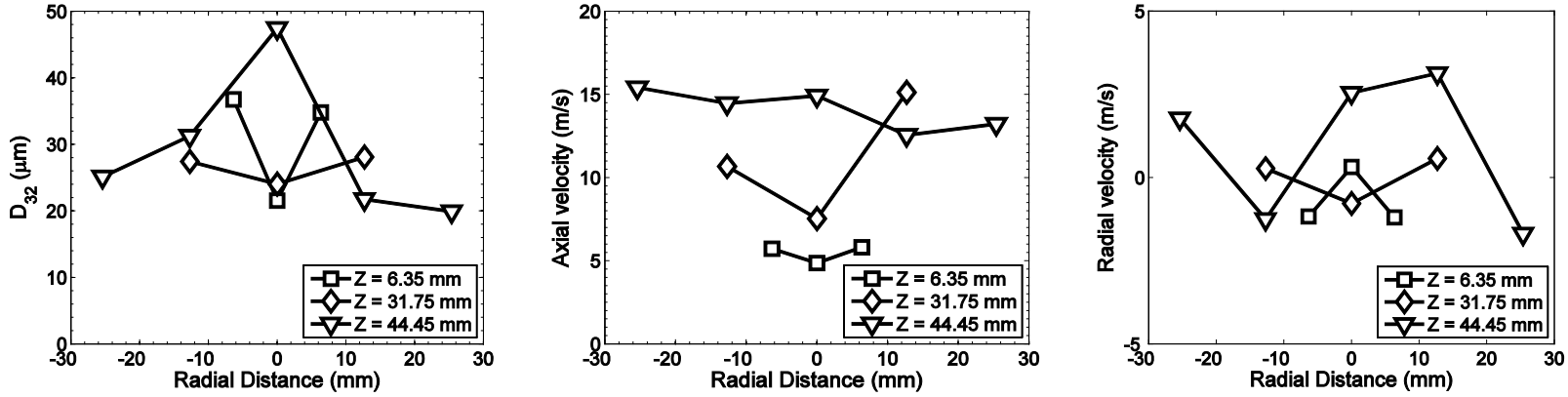

Figure 4.23 D_{32}, axial velocity and radial velocity in spray at equivalence ratio of 0.60 without co-flow of air

Spray Measurements with co-flowing air:

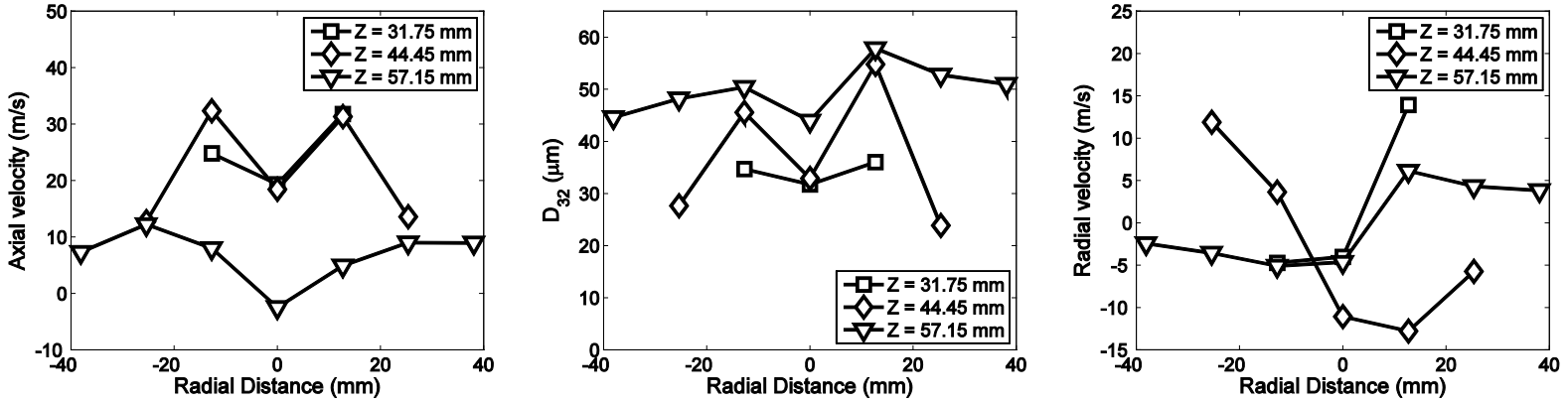

Figure 4.24 D_{32}, axial velocity and radial velocity in spray at equivalence ratio of 0.4 with co-flow of air

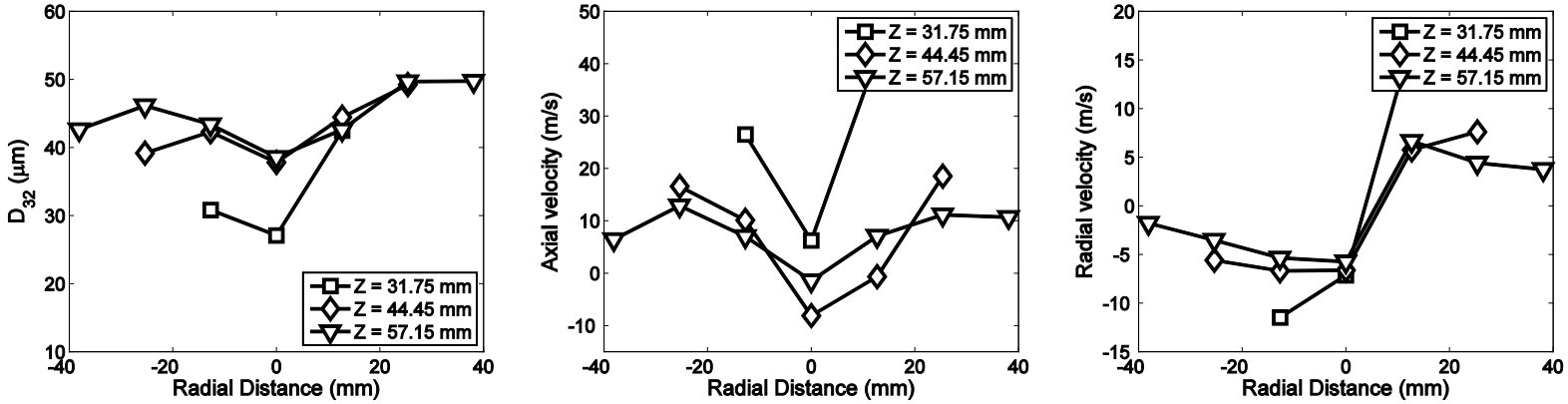

Figure 4.25 D_{32}, axial velocity and radial velocity in spray at equivalence ratio of 0.50 with co-flow of air

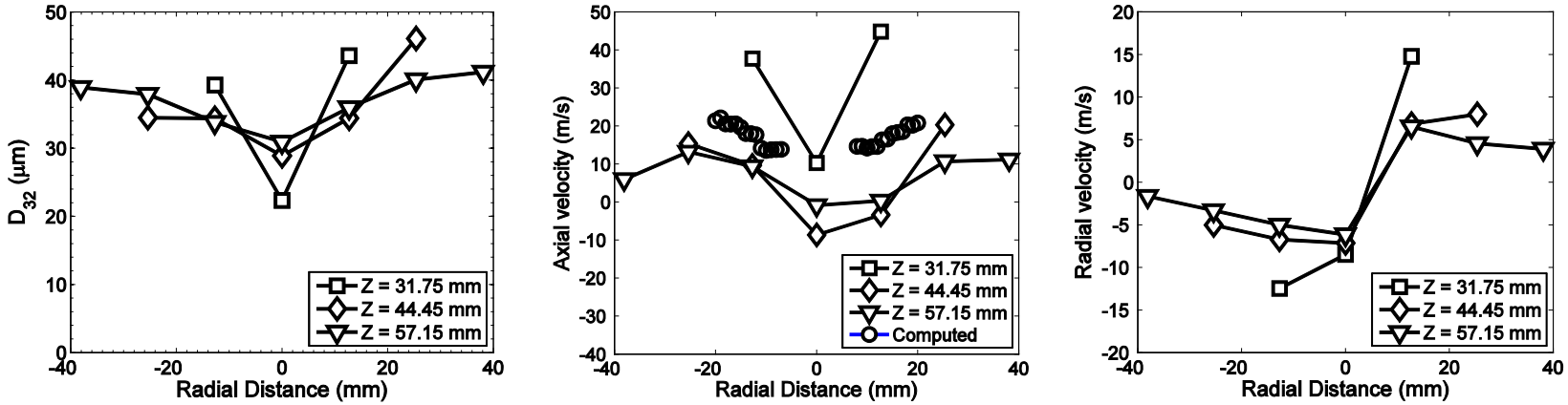

Figure 4.26 D_{32}, axial velocity and radial velocity in spray at equivalence ratio of 0.60 with co-flow of air

4.6 Summary and Conclusions

A parametric investigation of self-excited combustion dynamics behavior of a model high pressure LDI combustor was performed and effects of combustor geometry, inlet air temperature and global equivalence ratio were described. The combustor shows distinct and discriminating instability characteristics with changes in geometry and operating conditions that can be used to test computational models of practical geometries at realistic conditions.

The 1/4 wave air plenum (L_c = 0.2 m) and 1/4 wave combustion chamber (L_c = 0.56 m) was the most unstable combustor configuration with peak-to-peak pressure fluctuations as high as 20% of the mean chamber pressure. Generally, the dominant mode in the combustor was between 1200 -1600 Hz. This corresponded to the 2L mode for the short chamber and 4L mode for the long chamber configurations. Higher frequency modes in the 6-8 kHz range are also observed with high pressure fluctuation amplitudes, comparable to the 2L/4L mode amplitude at high equivalence ratios.

Larger combustion instability amplitudes were observed at higher equivalence ratios with strong fluctuations at the 1200-1600 Hz frequency mode while the lowest amplitudes were observed near lean blow-out conditions where the mode energy was spread across 1L-5L modes. A strong correlation was also observed between the inlet air temperature and instability levels with higher temperature resulting in lower pressure amplitudes. It is speculated that the lower temperatures result in lower droplet evaporation rates, non-uniform fuel distribution and spatio-temporal modification of the burning rate that lead to higher levels of combustion instabilities.

The 3/8 wave air plenum (L_p = 0.46 m) and 1/2 wave combustion chamber (L_c = 1.08 m) length was selected as the baseline configuration that presented combustion instability amplitudes close to the target (1-3% P'/Pc) at high air temperature and low equivalence ratio. Other parameters were run at the baseline configuration including fuel nozzle placement and fuel type.

For this configuration, the combustion instabilities with fuel nozzle at the throat of the venturi throat were stronger than with the configuration with fuel nozzle 2.6 mm upstream of the nozzle. Since the highest velocities of the swirling air flow are present at the throat, any acoustics based oscillations can have a greater effect by small variations of fuel injection location. At higher equivalence ratios, the 4L mode was dominant for both configurations with amplitudes between 40 and 82 kPa. At lower equivalence ratios, the energy was spread across the first five modes in the combustor, with the 1L mode dominant when fuel nozzle was upstream while 5L mode dominant when fuel nozzle was at the throat.

At the low amplitude instability conditions at lower equivalence ratios, a strong modulation in the dynamic pressure is observed. Dynamic pressure energy is distributed across several (1L-5L) low amplitude modes in the combustor. The significant difference in the energy spectrum between the high equivalence ratio cases where a dominant 4L mode is observed versus the low equivalence ratio case indicates possibility of different driving/damping mechanism at the two equivalence ratios ranges.

The parametric study of the self-excited LDI combustor showed distinct and discriminating instability characteristics that point to coupling processes between heat release, acoustics

and multi-phase hydrodynamics. The next chapter looks at the application of advanced laser based diagnostics to the optically accessible version of the chamber at the baseline configuration to further the understanding of the complex coupled physics. The OH-PLIF results at 0.6 and 0.44 equivalence ratios are described in detail along with their comparison with computational results by Huang et al [91].

A phase Doppler particle analyzer (PDPA) was used to measure the drop size distribution and droplet velocities for an unconfined spray at atmospheric pressure. The measurements were performed with and without a co-flow of air around the fuel nozzle. Drop sizes of 15-70 μm, axial droplet velocities up to 15 m/s and a spray cone angle of 68-70° were measured. Use of atmospheric pressure drop size measurements as input to the simulation did not provide the results that matched the high pressure, reacting flow measurements. Good spray measurements for the multi-distillate fuels used in this study at high pressure, reacting flow conditions are needed to provide appropriate data for model validations.

CHAPTER 5. 10 KHZ OH-PLIF MEASUREMENTS FOR STUDY OF COMBUSTION DYNAMICS IN A LEAN DIRECT INJECTION (LDI) COMBUSTOR

5.1 Introduction

In this chapter, combustion instabilities in the LDI chamber for the baseline chamber configuration -3/8 wave air-plenum and ½ wave combustion chamber- identified from the parametric survey detailed in Chapter 4 are further studied using PLIF and PIV measurements in an optically accessible chamber. Details of the optical chamber design and the laser, imaging and optics set-up were previously described at the end of Chapter 3.

A concurrent effort comprising simulations [90, 91] of the LDI combustor have been compared with the experiment to assess the ability of high-fidelity models to predict combustion dynamics. In the first half of the chapter, the comparisons for a representative case, inlet air temperature of 800 K and an equivalence ratio of 0.6, are presented. High frequency pressure and 10 kHz OH-PLIF measurements from experiment are compared with corresponding wall pressure, heat release and OH mass fraction results from hybrid RANS-LES simulations using both 2-step global and a reduced 18-reaction kinetics model. A dominant mode in the 1450-1650 Hz range (corresponding to the 4L chamber mode) is observed in the combustor, both in experiments and simulations, with a pressure fluctuation

amplitude of ~10% P'/Pc. Dynamic Mode Decomposition (DMD) of the OH-PLIF data and the simulation results identify similar dominant unstable modes in the combustor.

The second half of the chapter shows a comparison of OH-PLIF results at two equivalence ratios, 0.6 and 0.44. These cases highlight the distinct discriminating unstable behavior of the chamber as a function of operating condition. At the higher equivalence ratio ($\phi = 0.6$), a V-shaped flame anchored closer to the chamber dump plane with a dominant 4L mode in the combustor. At $\phi = 0.44$, the flame is lifted as much as 10-15 mm from the dump-plane and acoustic mode energy is distributed evenly across 1L-6L modes.

PIV measurements for the 780 K, $\phi = 0.45$ case, performed at 5 kHz are presented at the end of the chapter. Glare of the cylindrical window due to multiple reflections and scattering of light from the 532 nm laser sheet severely restricted good PIV measurements. Hence, only results for a limited field of view at the center of the flow-path are presented with the focus on the identification of location of the swirling flow and the presence of the vortex recirculation bubble (VBB).

5.2 Operating Conditions for OH-PLIF measurements:

The OH-PLIF measurements were performed at a range of equivalence ratios for constant inlet air temperature to the LDI combustor of 800 K. The 3/8 wave air plenum and ½ wave combustor chamber configuration of the combustor was used for all the tests with the fuel injector located 2.6 mm upstream of the venturi throat. Details of the operating conditions are tabulated in Table 5.1 below. Results from the PLIF 22 and PLIF 19 test cases (at

equivalence ratios of 0.6 and 0.44 respectively) have been used throughout the rest of the chapter for comparison with simulation results and then for comparison of physics.

Table 5.1: OH-PLIF Summary of operating conditions

Test ID	T_{air} (K)	ϕ	$\dot{m}_{air}$ (g/s)	Camera and Laser settings			
				Intensifier Gain	Intensifier Gate (ns)	Camera Exposure (µs)	Laser Power (W) (UV)
PLIF 22	795	0.6	81.6	65	100	97	6.7
PLIF 25	795	0.55	81.6	65	100	97	6.7
PLIF 18	800	0.48	81.6	66	100	97	6.7
PLIF 19	800	0.44	81.6	65	100	97	7.0

5.3 Comparison of Measured LDI Dynamics with Computational Results

Detailed treatment of the computational approach has been presented by Huang et al [90]. The simulation results presented here are based on work performed by Dr. Cheng Huang as part of the LDI project and a brief summary is provide here to help guide the comparison of results. The simulations are based on time-accurate solutions of the Navier-Stokes, energy and species equations. The numerical scheme is second order accurate in both time and space and uses an implicit formulation that allows for the use of high-aspect ratio grids near the wall. Turbulence is modeled using a hybrid RANS/LES formulation where the near wall region is modeled using a two-equation *k*-ω model. Combustion is accounted for using two sets of chemical kinetic models with laminar kinetics. In the first set, a simplified

two-step, five species global reduced mechanism prescribed by Westbrook and Dryer [106] is used,

$$2C_{12}H_{23} + 23.5O_2 \rightarrow 24CO + 23H_2O$$

$$2CO + O_2 \leftrightarrow 2CO_2$$

The second set of chemical kinetics consists of 18 step reactions including 15 species with $C_{11}H_{21}$ as a surrogate for Jet-A, and provides a more detailed description of the chemical reactions. This mechanism was proposed by Ajmani et al [107] and has been used in the simulation of single-element and multi-element LDI configurations using the National Combustion Code (NCC) under development at NASA Glenn Research Center.

Table 5.2: 18-step chemistry mechanism [106]

No.	Reaction
1	$C_{11}H_{21} + O2 \rightarrow 11CH + 10H + O_2$
2	$CH + O_2 \rightarrow CO + OH$
3	$CH + O \rightarrow CO + H$
4	$H_2 + O_2 \leftrightarrow H_2O + O$
5	$H_2 + O \leftrightarrow H + OH$
6	$H + O_2 \leftrightarrow O + OH$
7	$H_2O + O_2 \leftrightarrow 2O + H_2O$
8	$CO + OH \leftrightarrow CO_2 + H$
9	$CO + H_2O \leftrightarrow CO_2 + H_2$
10	$CO + H_2 + O_2 \leftrightarrow CO_2 + H_2O$
11	$N + NO \leftrightarrow N_2 + O$
12	$N + O_2 \leftrightarrow NO + O$
13	$N + OH \leftrightarrow NO + H$
14	$N + N + M \leftrightarrow N_2 + M$
15	$H + N_2O \leftrightarrow N_2 + OH$
16	$N_2 + O_2 + O \leftrightarrow N_2O + O_2$
17	$N_2O + O \leftrightarrow 2NO$
18	$N_2O + M \leftrightarrow N_2 + O + M$

Figure 5.1 below shows the computational geometry used for the simulations that exactly matches the experimental configuration with all important details (A, inlet choked slots; B, swirler; and C, choked exit nozzle) to ensure direct comparisons of results. The inlet air flow is choked at the entrance to the air plenum and a uniform mass flow boundary condition is applied. Adiabatic wall boundary condition is used all the walls of the combustor. This leads to an over-prediction of gas temperature, and consequently sound speed and mode frequency when compared with experiments where heat if rejected through the walls to a quiescent ambient environment. The flow is also choked at the exit nozzle of the combustor and sets a mean pressure of 1MPa in the chamber.

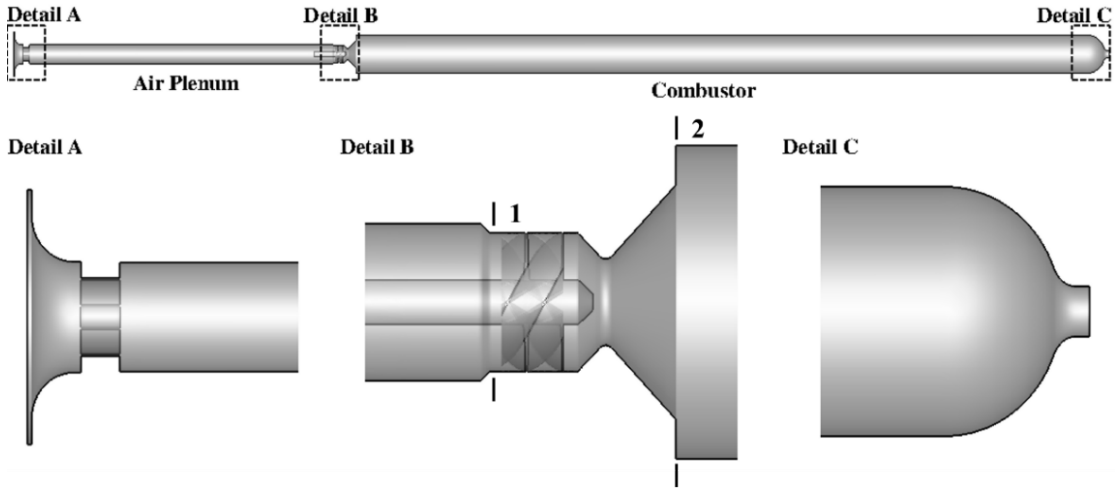

Figure 5.1: Computational geometry of LDI gas turbine combustor.

5.3.1 Pressure Comparison between Experiment and Simulation

Figure 5.2 below shows the comparison of wall pressure signal between measurement and prediction at an inlet air temperature of 800 K and an equivalence ratio of 0.6. The pressure signals have been high-pass filtered and taken at the same location near the head end of the

combustion chamber (~50 mm from combustor dump plane) for both experiment and simulation. The simulations results presented are from both 2-step and 18-step chemistry mechanism.

A peak-to-peak pressure fluctuation amplitude around 100 kPa can be seen in both experiment and simulation. The computed predictions using the more detailed kinetic model do not show a large difference, either in amplitude or dominant acoustic modes, from the one using a simplified mechanism. The 4L and 8L acoustic modes can be clearly identified in the power spectral density plots. The simulations capture most of the 6-8 kHz modes even with the detailed chemical model. It must be noted that the mode frequencies from the simulations are higher than the experimental measured frequencies, for example, the 4L frequency in the experiment is 1459 Hz while that in the simulation is 1650 Hz. This discrepancy is presumed to be on account of the adiabatic wall boundary condition applied in the simulation that leads to overall higher temperatures in the chamber, consequently leading to higher sound speeds and acoustic frequency. The combustor has thermal barrier coated walls for the first 100 mm downstream of the fuel injection location to minimize heat loss and provide close to an adiabatic boundary condition. Thereafter, the combustion products lose heat through a 6.35 mm (1/4”) thick carbon steel wall.

Overall, the simulations predict reasonable pressure amplitudes and captures the dominant acoustic frequencies measured in the experiments for both high and low equivalence ratios, but do not capture the high frequency modes between 6 and 8 kHz.

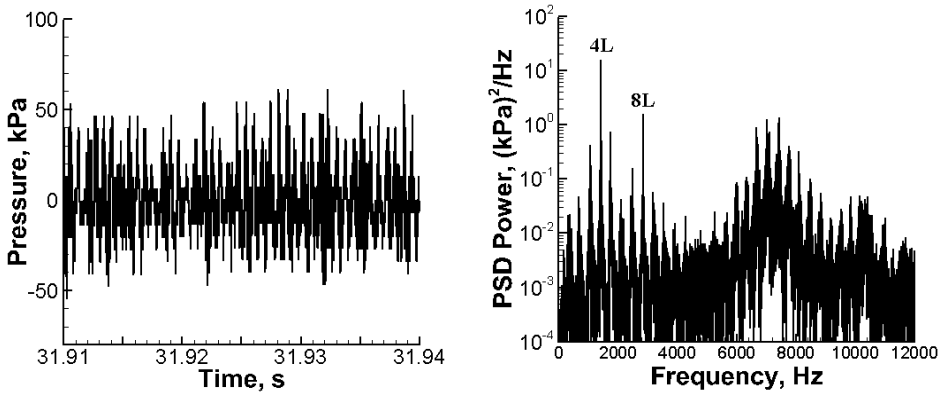

Experiment

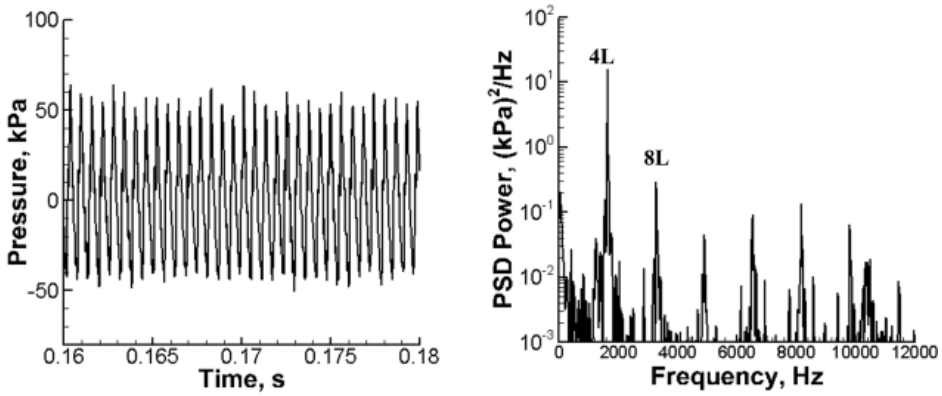

Simulation (2-step chemistry)

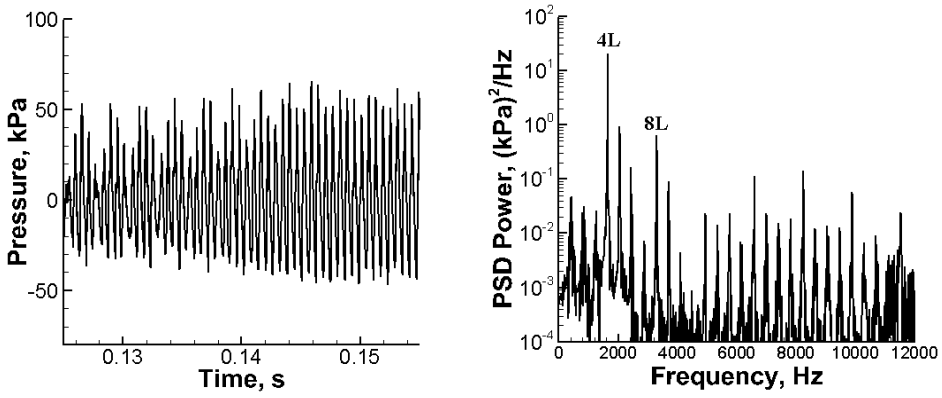

Simulation (18-step chemistry)

Figure 5.2: Experiment and simulation comparison at Tair: 800 K and ϕ: 0.6

5.3.2 Flame Front Extraction

For the study of the combustion response to chamber acoustics and hydrodynamics, a key parameter of interest is the location of the flamefront. A comparison of the flame front extracted from both experiments and simulation results can help in direct comparison of the spatial location of the combustion zone in the combustor. The method used for flame extraction from the OH-PLIF data and the simulations is briefly discussed below.

5.3.2.1 Experiment:

The OH radical persists in the combustion zone for a longer time than the heat-releasing reactions, it cannot be directly used as a flame marker. However, the sharp spatial gradient in intensity of the OH-PLIF signal has been used as a marker of the reaction zone in lean premixed flames. The high intensity in the OH-PLIF signal was used to demarcate the super-equilibrium OH formation based on an arbitrarily chosen threshold while the low intensity regions were considered to be the lower temperature unburnt gases or combustion products. It must be noted that this method is highly sensitive to SNR (mean SNR: 6.47 for the $\phi = 0.6$ case presented below) and can be challenging in high thermal power, high pressure flames. The three dimensional nature of swirl stabilized flames further makes the understanding of the extracted flamefront a challenge.

Figure 5.3 below shows instantaneous images of the OH-PLIF image taken in the LDI combustor. Figure 5.3 (a) shows the raw OH-PLIF signal that was corrected for spatial distortion and Figure 5.3 (b) shows the extracted flame front (yellow contour) overlaid on the PLIF image. The flame front extraction procedure prescribed by Slabaugh et al. [104] was followed. Good agreement is observed between the spatial location of the extracted

contour and outer periphery of the corresponding regions of high OH signal intensity. The small breaks in the detected flame surface in regions where the spatial gradient in the OH-PLIF signal remain high. These can be artifacts of filtering operations, which were required for suppression of false-flame edges in the low SNR images. The three dimensional nature of the swirling flame can also move in and out of the measurement plane, leading to a perceived 'break' in the flame front. The flame front contour is extracted as a mathematical function that denotes the spatial location of the flame front.

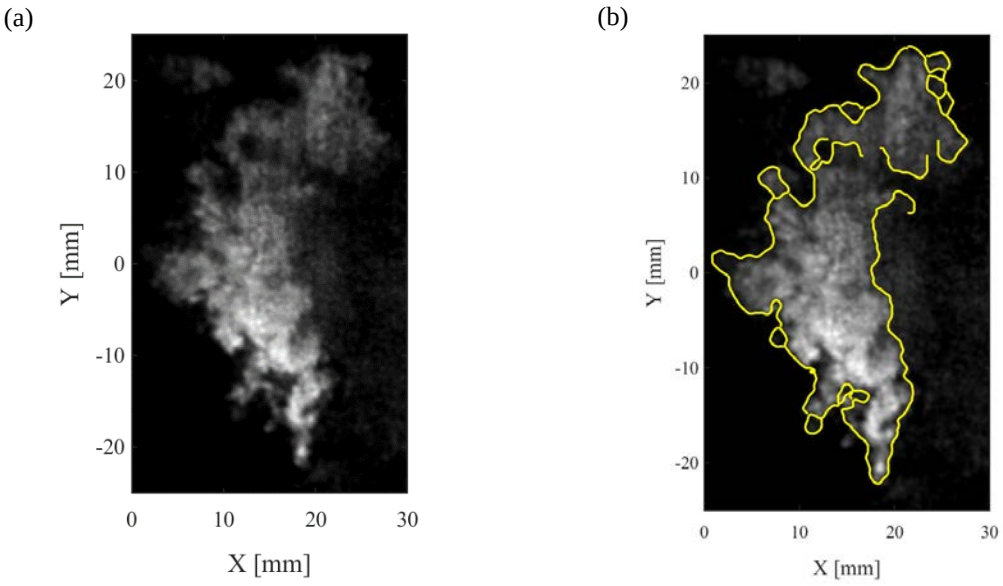

Figure 5.3: Instantaneous snapshots of the OH-PLIF measurements (a) corrected image and (b) corrected image overlaid with extracted flame-front

5.3.2.2 Simulation:

For the simulations with 2-step global chemistry mechanism, the flame front is extracted as the contour with mixture fraction, $Z=Z_{st}$. For simulations with the more detailed 18- step chemistry mechanism, the flame front is extracted based on both, computed heat release and OH-mass fraction. For heat release, the flame front is extracted as the contour with

mixture fraction, Z = Z_{st}. For the OH mass fraction, the contour where $|\nabla OH| = 1$ is denoted as the flame front.

Representative images of the extracted flame front from the computations are shown in Figure 5.4 below. Figure 5.4 (a) shows the flame front extracted based on the heat release distribution (grayscale) from the 2-step chemistry. The green line denotes the flame front. Similarly, Figure 5.4 (b) shows the extracted flame front (green line) based on heat release (grayscale) from the 18-step chemistry simulation while Figure 5.4 (c) shows the flame front extracted based on the OH-mass fraction distribution in the combustor. A high OH mass fraction that corresponds to warm combustion products is seen in the inner recirculation zone in Figure 5.4 (c). The transport of these warm combustion products (<1500 K) to the flame anchor upstream of the VBB is essential for ignition of incoming reactant mixture and consequently for flame holding and stabilization.

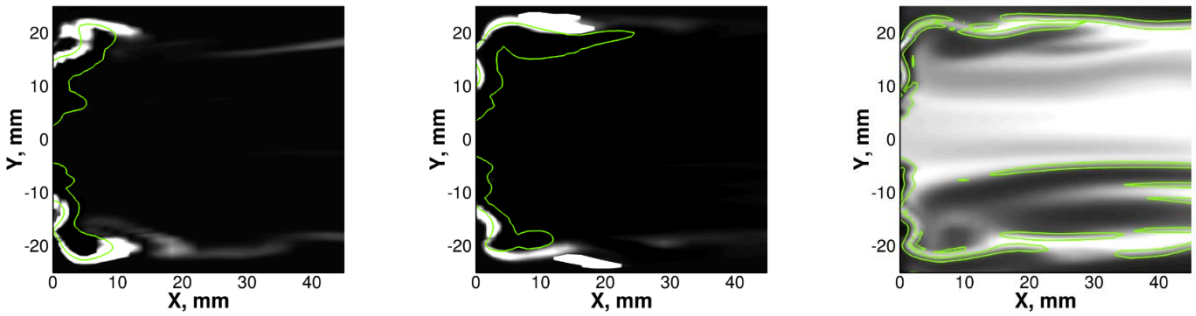

(a) 2-step global mechanism

(b) 18-step mechanism (heat release)

(c) 18-step mechanism (OH-mass fraction)

Figure 5.4: Flame front extracted from simulation results for (a) 2-step global mechanism, (b) 18-step mechanism- heat release distribution and (c) 18-step mechanism- the OH-mass fraction distribution.

The length of the flame front is tracked over 4000 images and a power spectrum of the flame front length is presented alongside the pressure power spectral density- both from

experimental data- in Figure 5.5 below. The flame spectrum shows a strong response at the frequency corresponding to the 4L mode in the combustor, and significant responses at the 1005 Hz and 8L mode frequencies. The 1005 Hz frequency lies between the 3L (1160 Hz) and 4L mode frequency (1459 Hz). This frequency is observed in the OH-PLIF data (flame front as well as DMD analysis presented later) but is not observed in the pressure spectrum. This indicates that the mode corresponds to the combustion response to other physics in the combustor that are not directly coupled to the chamber acoustics, e.g. hydrodynamics.

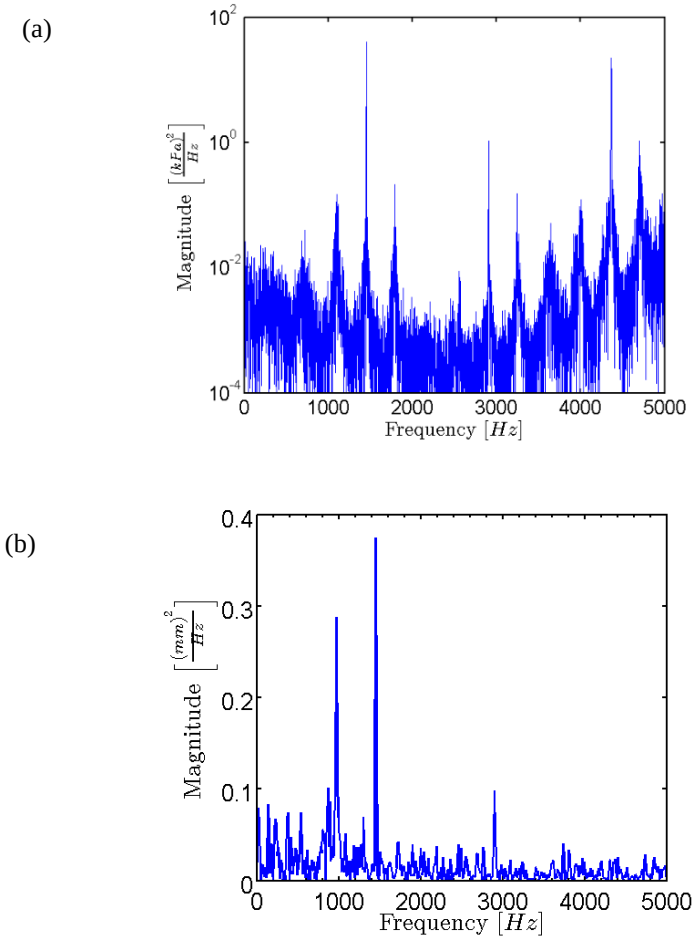

Figure 5.5: PSD of (a) pressure and (b) extracted flame front length

5.3.3 Flame Surface Density:

For the experiment, a planar analog of flame surface density commonly used in simulations to denote the reaction rate was calculated from the flame front extracted from the experimental data. The planar flame surface density is given by,

$$\Sigma = \frac{\partial A_f}{\partial V} \tag{5.1}$$

where, A_f is the flame surface area defined over volume V. The domain was divided into 1 mm^2 domains and the total flame front length in each domain was calculated over a range of 4000 OH-PLIF images and summed.

For the simulation results, the flame surface density was calculated for a 2D slice of the data extracted at the center slice of the combustor to enable direct comparison with the experimental measurements. The flame surface density for the computations was calculated as,

$$\Sigma = |\nabla Z| \delta(Z - Z_{st}) \tag{5.2}$$

where, Z is the mixture fraction and Z_{st} is the stoichiometric mixture fraction.

Instead of calculating the flame surface density based on the mixture fraction as shown in this study, the average flame length and flame surface area based on the progress variable in turbulent premixed flames has also been used to calculate flame surface density previously [110]. In this method, the turbulent flame zone is viewed as an ensemble of laminar flamelets and the local flame curvature and strain rate is used to determine the local burning rate, which is a function of the unburned gas density, ρ_u, a modified laminar flame

I_0 length based on the local stretch rate of the flamelet and the ratio of local flame surface are to volume ratio, Σ.

$$\overline{w} = \rho_u S_L I_o \Sigma \tag{5.3}$$

An algebraic expression for Σ is obtained as a function of the progress variable *c*, which is varies from zero to 1 from the reactants to the products respectively. L_y is the scalar integral length scale.

$$\Sigma = \frac{g\bar{c}(1-\bar{c})}{L_y} \left\langle \left| {}^{1}/_{\sigma_y} \right| \right\rangle \tag{5.4}$$

The flame surface density (FSD) for experiment and simulations is presented in Figure 5.6 below. The flame contour shows a symmetric distribution across the central axis of the combustor that extends up to 40 mm from the combustor plane for both set of simulations as well as the experiment. For the simulations, the FSD shows good agreement between the 2-step mechanism and the 18-step mechanism. Previous studies by Huang et al. [109] identified formation of a recirculation zone in the center of the combustor that is typical of swirl stabilized flames. The mode corresponding to the formation and periodic oscillation of a central recirculation zone, identified as a vortex bubble breakdown (VBB) and its harmonic frequency multiples, were observed to be present at frequencies close to the strong acoustic mode frequency in the combustor, namely the 4L mode. The FSD computed from the simulations clearly identify the VBB as the lower flame surface density in a V shaped zone that extends upstream beyond the dump plane of the combustor (at x=0 mm). The flame surface density is highest in the shear layer region where maximum heat release occurs outside the VBB and extends up to 30 mm from the dump plane. In the FSD

calculated based on the OH-PLIF images (Figure 61 (a)), a V-shaped pocket of high flame surface density is seen about the central axis with a lower flame surface density inside the V. This lower amplitude region may correspond to the VBB clearly seen in the simulations. Overall, the FSD comparison between experiment and simulations shows qualitative similarities but quantitatively the simulations shows significant difference to the experimental data with most of the heat release isolated in the region in the shear layer region outside the VBB.

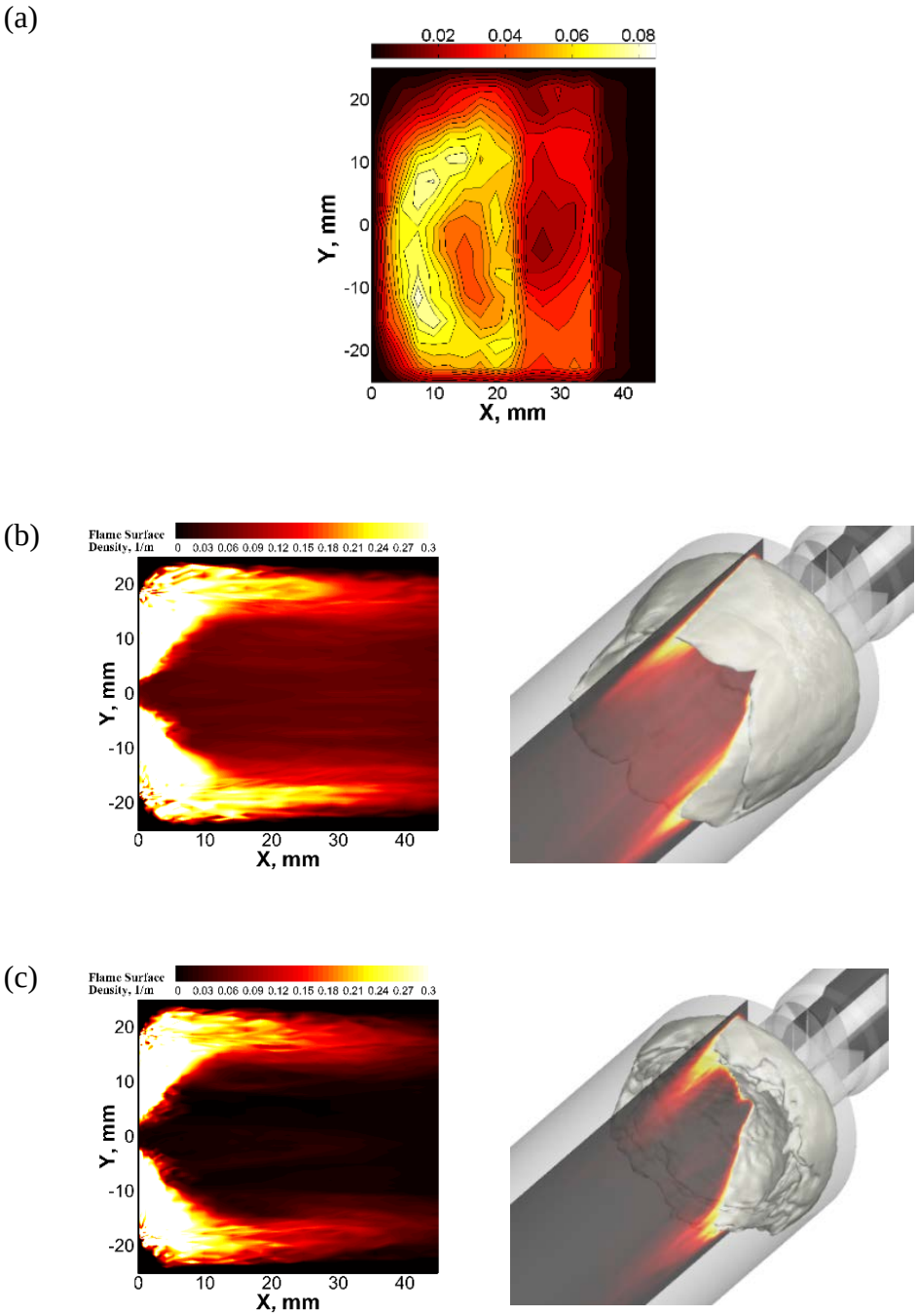

Figure 5.6: Flame Surface Density (a) experimental OH-PLIF measurements, (b) 2-step global chemistry simulations (2D slide center slice-left and 3D-right) (c) 18-step chemistry simulation (2D center slice slide-left and 3D-right)

5.3.4 Dynamic Mode Decomposition Analysis

The use of Dynamic Mode Decomposition (DMD) [108] provides insight into the dynamic patterns of the quantities of interest such as heat release, OH-signal intensity, velocity field, and species concentrations in a combustor. The DMD procedure is similar to Proper Orthogonal Decomposition (POD) that is widely used for the decomposition of large data-sets, but whereas POD modes typically contain multiple frequencies, each DMD mode consists of a single frequency. Comparisons between the DMD and POD analyses applied to longitudinal mode combustion instabilities by Huang et al. [109] led to the conclusion that the underlying physics can be more efficiently understood with DMD, especially when there are high amplitude instabilities present that control the unsteady flame behavior.

Figure 5.7 below shows the DMD mode spectrum calculated using 1000 OH-PLIF images with a time separation of 0.1 ms between each for the case at an inlet air temperature of 800 K and an equivalence ratio of 0.6. The spectrum is compared with that obtained from a similar DMD analysis of the simulation results with both the 2-step and 18-step chemistry mechanisms at the same operating conditions. Strong peaks at 1005 Hz and at the 4L (1459 Hz) and 8L (2909 Hz) mode frequencies and lower amplitude modes at 480 Hz and the 1L (340 Hz) are observed. The spatial mode-shape at the ~500 Hz, ~1 kHz and at the 4L mode frequency which show the highest DMD mode power in the experiment are shown in Figure 5.7. The DMD modes for the 4L and 8L modes align well with the strongest frequencies present in the pressure spectrum shown in Figure 5.2. Other acoustic modes that are less than <5 kHz do not show up on the DMD spectrum in the experiment. The modes >5 kHz are not resolved as the OH-PLIF measurements are performed at 10 kHz repetition rate.

The ~1 kHz mode response is strong but is not present in the acoustic spectrum in either experiment or simulation. Also, this mode has a higher amplitude when DMD is performed for a 2D-center slice of the simulation data (Figure 5.7 (b)) than when it is performed for the entire 3D domain in the 2-step chemistry simulation. The ~1 kHz mode amplitude is highly damped in the 18-step chemistry simulation. This mode shows a strong swirling behavior as seen in the next section and its absence from the acoustic spectrum may be on account of a two dimensional representation of the OH-PLIF data/ simulation result of an inherently 3D phenomenon. This highlights the point that though 2-D experimental measurements such as OH-PLIF and PIV are highly valuable as the validation data for simulations, the results obtained can easily be misrepresented, especially for inherently 3D flow structures observed like swirl stabilized combustion. It also highlights the need for running 3-D simulations and not relying on 2D axisymmetric simplifications of highly swirled flames.

Comparison between the OH and heat release (Q) DMD spectrums in Figure 5.7 (c) shows that the 18-step chemistry simulations identify multiple peaks in the <1 kHz range in the OH spectrum that are not in the heat release spectrum.

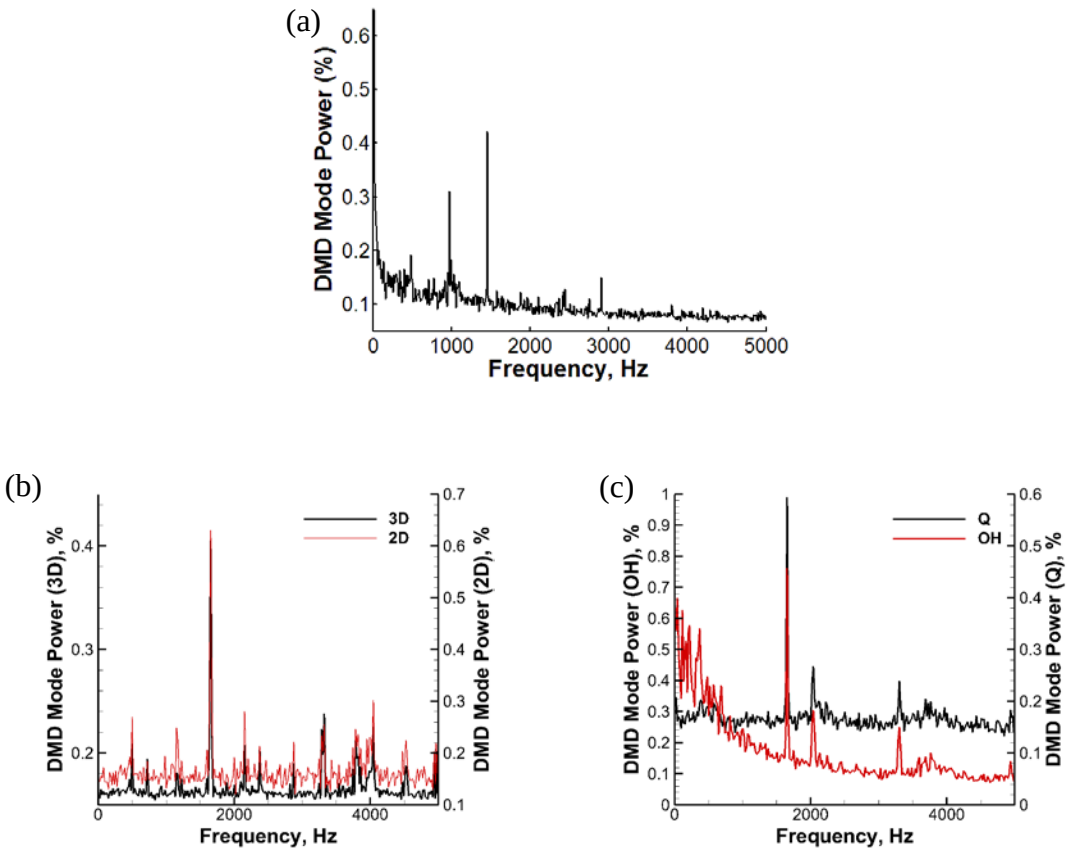

Figure 5.7: DMD Mode Spectrum for Tair: 800 K and ϕ = 0.6: (a) experimental OH-PLIF measurements, (b) center slice 2-step global chemistry simulations (c) center-slice 18-step chemistry simulation

5.3.4.1 DMD Spatial Mode Shapes

The spatial mode shapes for the dominant DMD modes are presented in Figure 5.8 -Figure 5.10 for frequencies of 480 Hz (500 Hz simulation), 1005 Hz (1150 Hz simulation) and 4L mode (1459 Hz-experiment and 1650 Hz-simulation). The DMD analysis is performed using mean subtracted images so only the fluctuations in the OH-PLIF signal (for experiment) and computed heat release rate is visible. For the 18-step chemistry the spatial mode-shape based on calculated heat release is presented. The major difference between the OH-PLIF and simulation mode-shapes is that the response is distributed across the

cross-section in the experimental data whereas the heat release response is concentrated in the shear layer region outside the VBB in the simulations. Nonetheless, qualitative similarities can be observed between the two and is highlighted below for each of the three modes.

For the 481 Hz mode, the signal is symmetric about the center axis of the combustor with a high intensity region in one half and a low intensity region in the other half of the combustor that alternates through its cycle. This response indicates a swirling mode in the combustor. The 481 Hz mode is absent from the pressure spectrum but is clearly present on the DMD spectrum, suggesting combustion response to a purely hydrodynamic mode. The 1005 Hz mode-shape is similar to the 480/500 Hz mode with a distinct bulk swirling motion observed. The swirling mode, observed especially in the OH-PLIF data is structured in a V-shape along the VBB in contrast with the 480 Hz mode which more uniform in the axial direction.

The 1459 Hz (4L) mode corresponds to the strongest acoustic mode in the combustor. The spatial mode shape shows a symmetric high intensity region about the central axis of the combustor with two lobes on either side of it that are exactly opposite in intensity. The simulation results show a similar structure qualitatively. The high intensity region observed near the dump plane extends into the diverging section of the venturi for the simulations but has not been shown here. The experiment does not have optical access upstream of the dump plane yet instantaneous OH-PLIF images show evidence of the flame extending upstream past the dump plane intermittently. The 4L mode is discussed in further detail in the next section.

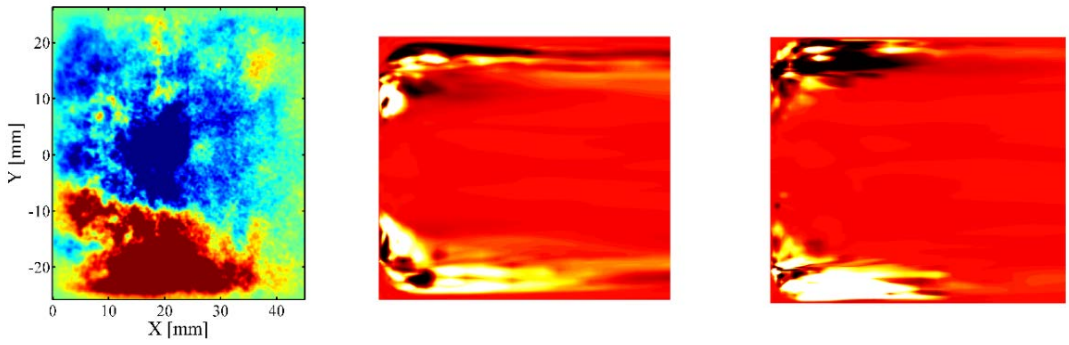

Figure 5.8: DMD spatial mode for Tair: 800 K and ϕ: 0.6 at *f:* 480 Hz from OH-PLIF signal (left), at *f*: 500 Hz from the 2-step chemistry simulations (center) and *f*: 480 Hz from the 18-step chemistry mechanism

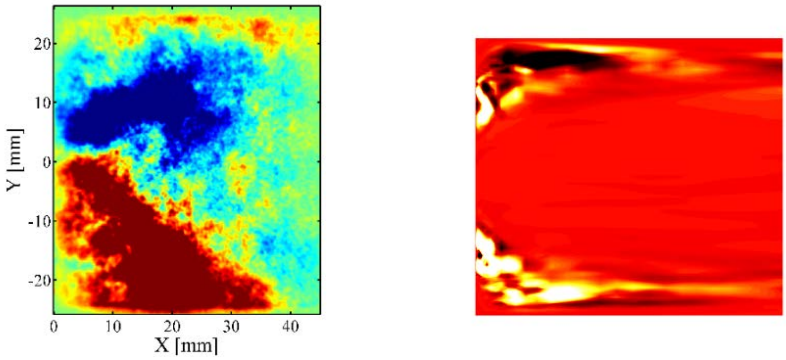

Figure 5.9: DMD spatial mode for Tair: 800 K and ϕ: 0.6 at *f:* 1005 Hz from OH-PLIF signal (left) and at *f:* 1150 Hz from 2-step chemistry simulations (right)

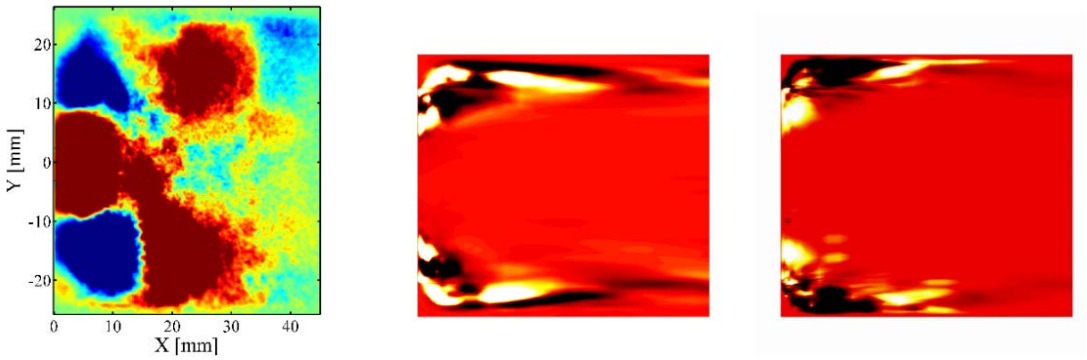

Figure 5.10: DMD spatial mode for Tair: 800 K and ϕ: 0.6 at *f:* 1459 Hz from OH-PLIF signal (left), at *f:* 1650 Hz from 2-step chemistry simulations (center) and *f*: 1650 Hz from the 18-step chemistry mechanism

5.3.4.2 Cycle Analysis

Images representing one cycle (0 to T s) of the DMD mode at the 4L acoustic frequency in the combustor are shown in Figure 67 below. The images are shown for the OH-PLIF signal (1459 Hz), OH mass fraction and computed heat release (1650 Hz) for the 18-step chemistry simulation, and for the computed heat release from the 2-step chemistry simulation (1650 Hz). The cycle is extracted based on the temporal signal of the DMD mode in the experiment. As shown in Figure 5.11 below, the band-pass filtered (at 1459 Hz) wall pressure measurement in the experiment near the exit nozzle is in phase with the DMD temporal signal. For the 4L mode, the pressure near the exit nozzle is in phase with the pressure near the head end of the chamber. The acoustic compression and expansion processes are in phase with the OH-signal intensity where the PLIF signal is measured in the combustor. Snapshots for closely corresponding points in the 1650 Hz 4L acoustic cycle for heat release and OH mass fraction are extracted from the simulations to allow direct comparison with the experiment. The separation in the time between snapshots is 1 ms, or 1/7T for the experiment. The simulation results are down-sampled to match the experimental data rate.

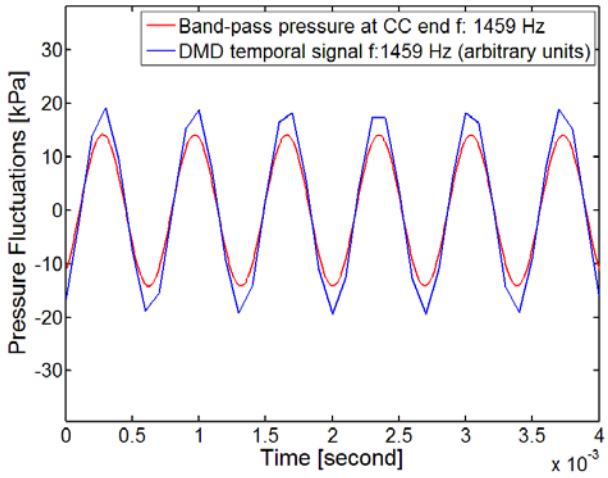

Figure 5.11: DMD temporal signal and band-pass filtered pressure signal at 1459 Hz for PLIF22 test case (Tair: 800 K and ϕ: 0.6)

The cycle (at t=0) represented in Figure 5.12 starts at the minimum value of the OH-PLIF signal, heat release generation and the OH mass fraction. This also corresponds to the minimum in the acoustic pressure amplitude (expansion process) at the head end of the combustion chamber for the 4L mode. At this time instant, the expansion wave of the acoustic cycle leads to a high pressure differential across the injector that draws fresh reactants into the chamber. At the same time, warm combustion products are entrained in the central recirculation region (VBB) and are transported towards the dump plane helping in the ignition of incoming reactant mixture. Most of the field of view is at a relatively low intensity at this time. This is portrayed with good agreement in the OH-PLIF signal and the OH mass fraction images. The heat release is negligible immediately downstream of the dump plane at t=0 as well.

At t=T/7, high intensity pockets are observed close to the dump plane which indicate ignition of the reactant mixture and corresponding increase in the heat release. The overall

heat release is still significantly lower near the dump plane but the OH signal from the experiment and OH mass fraction show an increasing trend. From t=2T/7 through to 4T/7, the OH-signal, OH mass fraction and heat release are all at their highest intensity near the combustor dump plane. This coincides with a peak in the pressure fluctuation amplitude for the 4L cycle (acoustic compression wave) near the dump plane. The compression wave promotes premixing of the reactant mixture which coupled with presence of warm combustion products leads to high heat release and increased production of OH across the field of view. At t=4T/7, as the pressure fluctuation amplitude begins to decrease, the OH distribution shifts both downstream of the dump plane as well as radially outward into the outer recirculation zones near the chamber wall. For the simulation with the 2-step chemistry model, the heat release signal near the dump plane peaks later and lasts longer in the cycle than the 18-step chemistry simulation, from t=4T/7 to 5T/7.

From t=5T/7 to 6T/7, the location of the region with maximum heat release moves downstream of the dump plane. The OH-PLIF signal as well as the OH mass fraction are low in the field of view with small pockets of high intensity near the chamber wall. At this time, the pressure fluctuation amplitude approaches its minimum that corresponds to an acoustic expansion wave near the dump plane drawing fresh reactant mixture into the chamber. The entire cycle repeats starting from t=T.

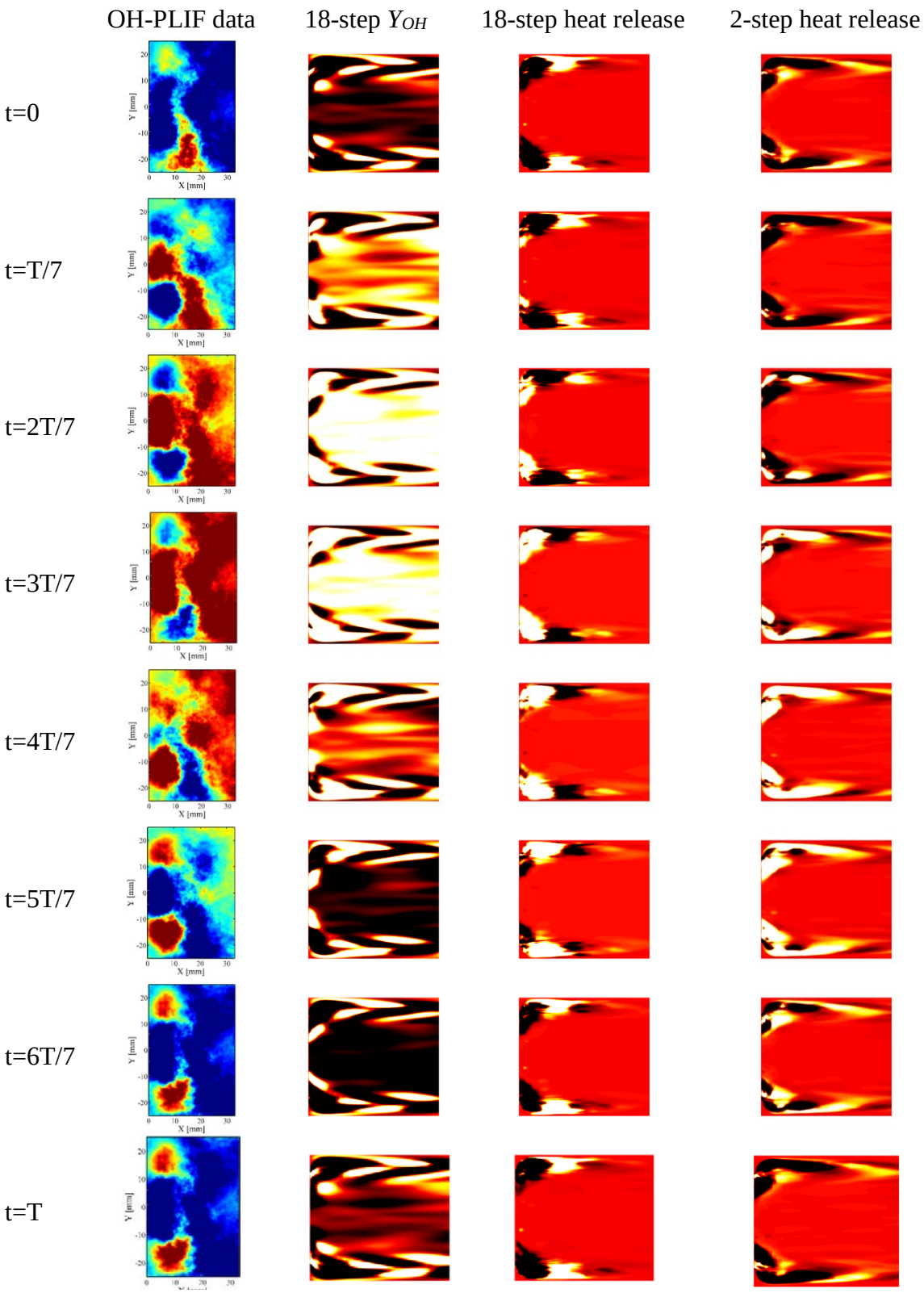

Figure 5.12: Cycle analysis of DMD mode at the 4L frequency for the Tair: 800 K and ϕ: 0.6 test

5.4 Effect of Equivalence Ratio on Combustion Instabilities in LDI Combustor

5.4.1 Pressure and OH-PLIF Time History

The OH-PLIF measurements were conducted at varying equivalence ratios as highlighted by the operating conditions tabulated in Table 5.1. Two of the cases that showed discriminating behavior in terms of pressure fluctuation amplitudes as well as dominant modes are compared on the basis of OH-PLIF measurements. A comparison of pressure results for test cases equivalence ratios of 0.6 and 0.44 (PLIF22 and PLIF19 respectively) is repeated from Chapter 4 to help guide the comparison. The PLIF22 case (ϕ=0.6) presents high amplitude instabilities between 80-150 kPa with the dominant pressure instability at the 4L mode at 1450 Hz. The harmonics of this mode are also strong in amplitude. The high frequency range between 5-7 kHz shows instabilities as high as the 4L mode in some cases. The lower modes 1L-3L are present, but at lower amplitudes. These become stronger in amplitude as the equivalence ratio is reduced while the higher frequency modes drop in amplitude. The PLIF19 case (ϕ=0.44) is more stable than PLIF22 and shows pressure fluctuation amplitudes of 30-40 kPa. The instability does not reach a limit cycle and large modulation in pressure, from 5-40 kPa, is seen over the course of the test. The mode-energy is spread evenly over 1L-6L modes at ϕ = 0.44 and the pressure spectrum is quite distinct compared to the ϕ = 0.6. The significant change in the unstable behavior of the chamber from ϕ=0.6 to 0.44 is important as this range represents cases within the operation envelope of an aviation gas turbine from take-off to cruise and can have a strong bearing on the engine design. The discriminating behavior observed at the two equivalence ratio cases in

the experiment is also important as validation cases for the development of predictive capability in high fidelity simulations to combustion instabilities.

Figure 5.13 below shows the high pass filtered pressure data for a time-slice when the OH-PLIF images were obtained for PLIF 22 and PLIF19 test cases. The pressure-time history shows a near limit cycle like behavior with near constant pressure oscillation amplitude from cycle to cycle for PLIF 22 while lower amplitudes and more modulation in pressure amplitude for the PLIF19 case. A magnified image of the pressure data for a shorter time-slice is presented on the right of the figure. The pressure signal shows an overarching 4L cycle with multiple pressure peaks enveloped under it. These shorter pressure cycles correspond to the higher frequency peaks in the 5-7 kHz frequency range, which are not resolved by the OH-PLIF measurement which is limited to a repetition rate of 10 kHz. The power spectral density plot of pressure measured near the exit nozzle of the combustor is presented in Figure 68 (a) (note PSD plots presented earlier were of data at the combustor head end, and had a somewhat different appearance). Possible, related sources for the large number of modes indicated by the PSD include the numerous couplings between the strong thermo-acoustics in a highly-confined combustion zone, hydrodynamic modes related to the high swirl number (S~1) flow entering the combustor, the continually changing cross-section area in the diverging section of the venturi that could lead to wave dispersion and complex interactions with heat release, and nonlinear coupling between hydrodynamics, heat release, and acoustics.

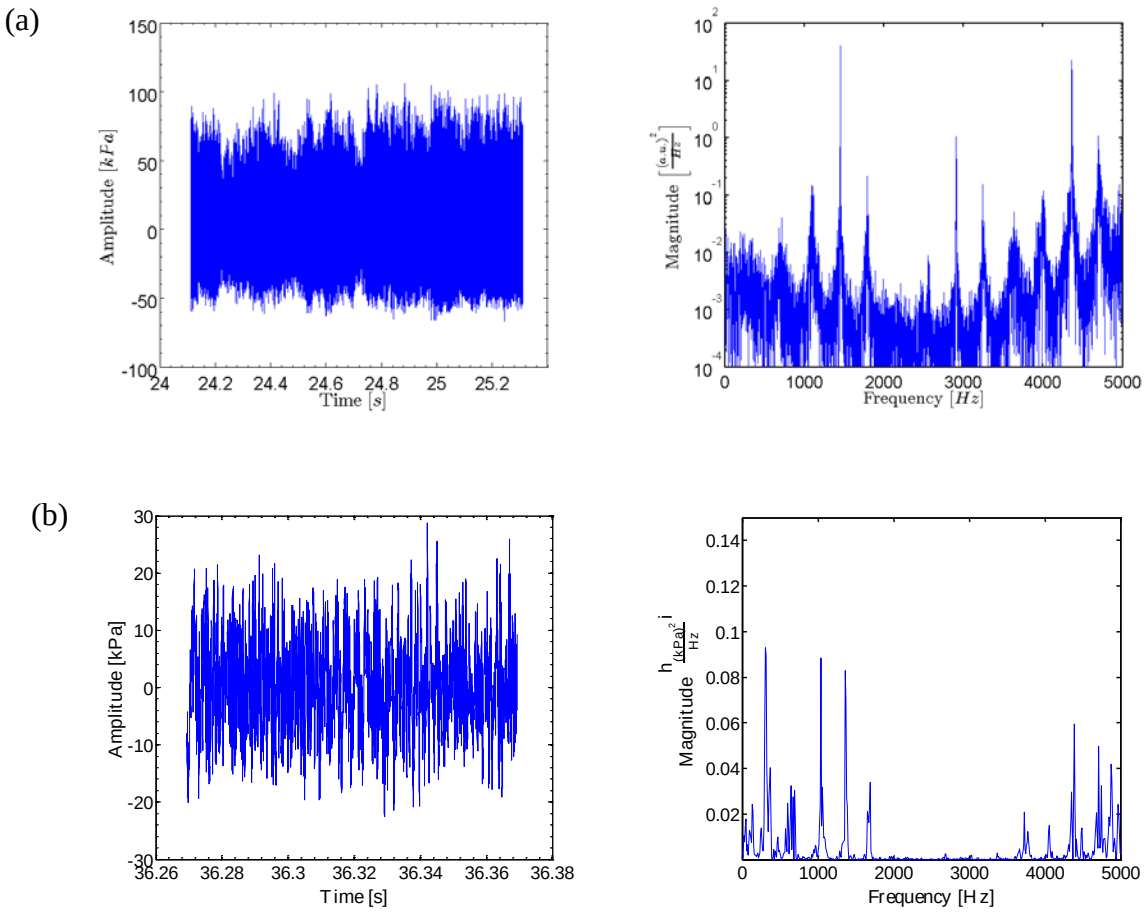

Figure 5.13: High pass filtered pressure data (left) and pressure power spectrum power (right) for the (a) $\phi = 0.6$ test case and (b) $\phi = 0.44$ test case over the time slice selected for the OH-PLIF image analysis

5.4.2 Flame Front Extraction

The length of the flame front is tracked through time and a power spectrum of the flame front length is presented Figure 5.14 below for $\phi = 0.6$ and $\phi = 0.44$ test cases. The flame spectrum shows a strong response at the frequency corresponding to the 4L mode in the combustor, and significant responses at the 3L and 8L mode frequencies for the higher equivalence ratio case and mirrors the dominant modes identified in the pressure power

spectrum in Figure 5.13. At the lower equivalence ratio (ϕ = 0.44), the pressure spectrum shows low amplitude pressure modes from 1L – 5L with amplitudes that are comparable to each other. The flame front spectrum indicates a dominant mode near the frequency of the 3L acoustic mode, with a few weaker modes. The power spectral density plots are plotted on a linear scale for clarity.

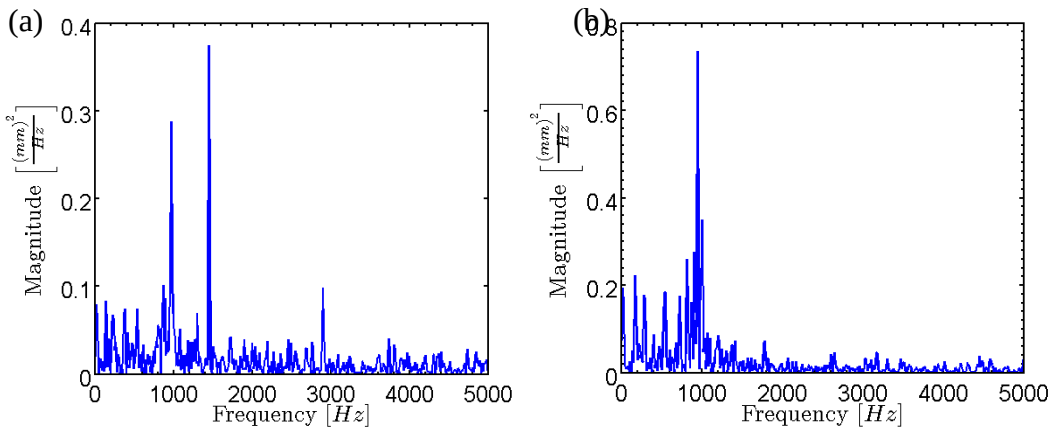

Figure 5.14: PSD of flame front length for (a) ϕ = 0.6 and (b) ϕ = 0.44 test cases

5.4.3 Flame Surface Density

Figure 5.15 below shows the flame surface density contour for ϕ = 0.6 and ϕ = 0.44 test cases. The flame contour shows a fairly symmetric distribution across the central axis of the combustor. A C-shaped pocket of higher amplitude flame surface density is seen about the central axis with a lower amplitude region located inside the C. This lower amplitude region includes the transport of combustion products through reversal of flow from the vortex breakdown bubble (VBB) region towards the flame front. The flame is stabilized

approximately 3-4mm from the dump plane at the leading edge of the VBB at $\phi = 0.6$. At the low equivalence ratio, the contour plot shows higher intensity regions further away from the dump plane centered within the lower intensity regions. The flame is still symmetric about the axis of the combustor. The flame is also spread across a longer area in the combustor extending approximately 35 mm from the dump plane. The spread was limited to approximately 20 mm for ϕ: 0.6. This shows that at a lower equivalence ratio the flame shape is less compressed and the thermal power is distributed over a large area leading to weaker spatial interactions with the combustor acoustics than at higher equivalence ratio where the flame is shorter and the thermal power is concentrated in a smaller volume.

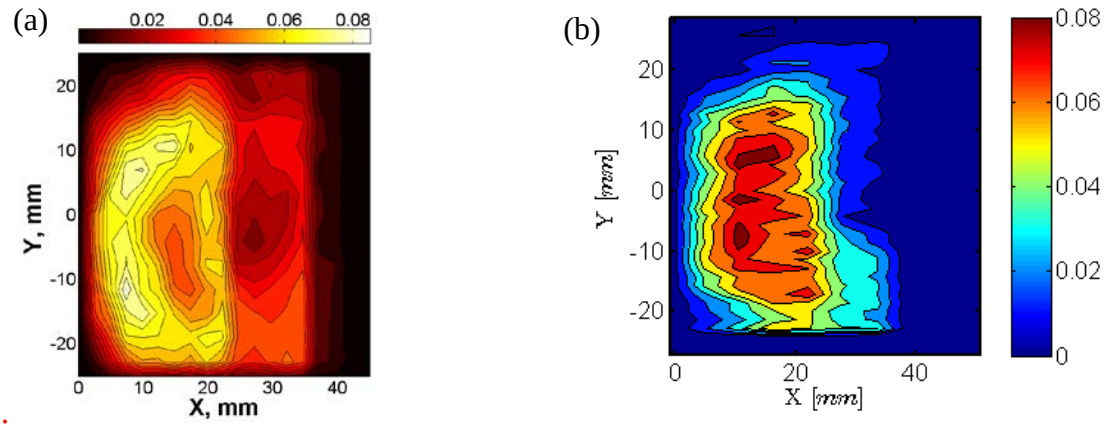

Figure 5.15: Flame Surface Density for (a) ϕ = 0.6 and (b) ϕ = 0.44 test cases

5.4.4 Dynamic Mode Decomposition (DMD) Analysis

Figure 5.16 shows the DMD mode spectrum calculated using 1000 images with a time separation of 0.1 ms between each for ϕ = 0.6 and ϕ = 0.44 test cases. At the higher equivalence ratio, strong peaks at 973 Hz and at the 4L (1459 Hz) and 8L (2909 Hz) mode frequencies and lower amplitude modes at 480 Hz and the 1L (340 Hz) are observed. The spatial mode-shape for some these modes is presented in the next section. The DMD modes for the 4L and 8L modes align well with the strongest frequencies present in the pressure spectrum shown in Figure 5.13. Other acoustic modes do not show up on the DMD spectrum. The 973 Hz mode response is strong but is not present in the acoustic spectrum. This mode shows a strong swirling behavior as seen in the next section and its absence from the acoustic spectrum may be on account of 2D representation using OH-PLIF signal of a 3D phenomenon. It is important to note that these DMD modes of OH are limited to window downstream of the dump plane, and that the flame extends in to the diverging section of the venturi that is inaccessible to optical measurements. At the lower equivalence ratio (PLIF19), a strong peak is identified at a frequency of 1012 Hz which corresponds to the 3L acoustic mode in the combustor. The same frequency is identified in the pressure and the flame front spectra shown in Figure 5.13. A large number of peaks are present around the strong 3L frequency that show similar behavior to the 3L peak. These can also be an artifact of a two dimensional view of a highly three dimensional flow-field with a high swirl number.

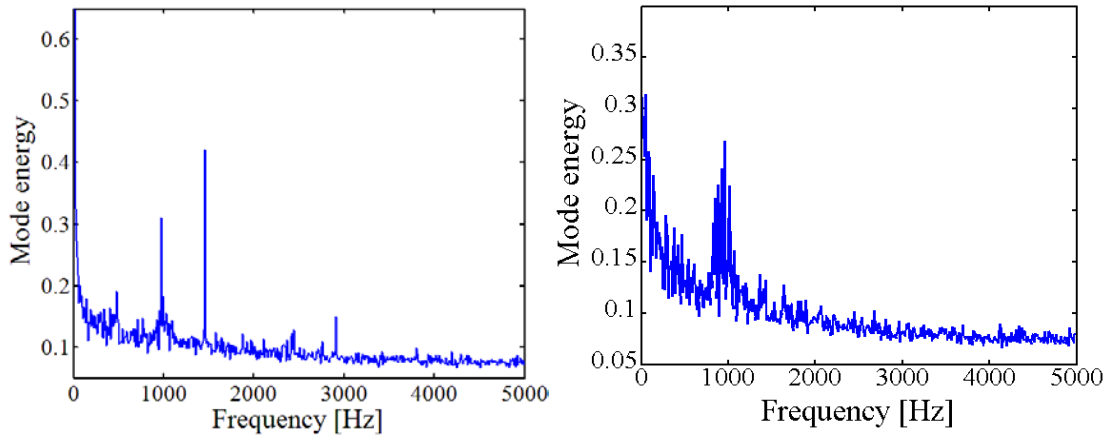

Figure 5.16: DMD Mode Spectrum based on OH-PLIF images for (a) $\phi = 0.6$ and (b) $\phi = 0.44$ test cases

5.4.5 DMD Spatial Mode Shapes:

Snapshots representing one cycle (0 to T s) of the 4L (1459 Hz) DMD mode of the OH signal at the higher equivalence ratio of 0.6 are presented in Figure 5.17. The cycle is extracted based on the temporal signal of the DMD mode. As discussed earlier for Figure 66, the band-pass filtered (at 1459 Hz) wall pressure measurement near the exit nozzle is in phase with the DMD temporal signal. For the 4L mode, the pressure near the exit nozzle is in phase with the pressure near the head end of the chamber. The acoustic compression and expansion processes are in phase with the OH-signal intensity where the PLIF signal is measured in the combustor. The separation in the time between snapshots is 1 ms, or 1/7T. At the start of the cycle, defined as a minimum in the OH signal, two high intensity axisymmetric lobes are observed near the combustor wall close to the dump plane. These high intensity zones may correspond to leftover pockets of hot combustion products in the outer recirculation zones. As the OH-signal increases, the high intensity lobes are replaced

with a fresh mixture of fuel and air (low intensity lobes). When the OH-signal is at its maximum point in the cycle (at t= 4T/7), the signal intensity is high across the PLIF sheet (except for the two low intensity lobes) and a V-shaped structure can be seen along the edges of possible a vortex breakdown bubble. This may suggest a reaction flame front along the shear layer of vortex recirculation bubble (VBB) that is anchored near the dump plane near its stagnation point. The stagnation point of the VBB is along the central axis of the combustor and at the upstream edge of the VBB. Due to the low velocity in the VBB and the pressure differential between the VBB and the surrounding shear layer, some of the combustion products may be transported back into the VBB and flow upstream towards the dump plane to pre-heat the incoming fuel and air. After this point in the cycle, the intensity across the PLIF sheet is lower, and high intensity lobes start forming close to the combustor wall near the dump plane. This may correspond to an acoustic expansion wave near the dump plane which draws in more fuel and air into the combustion chamber from t= 5T/7 and t=6T/7. The entire cycle repeats starting from t=T.

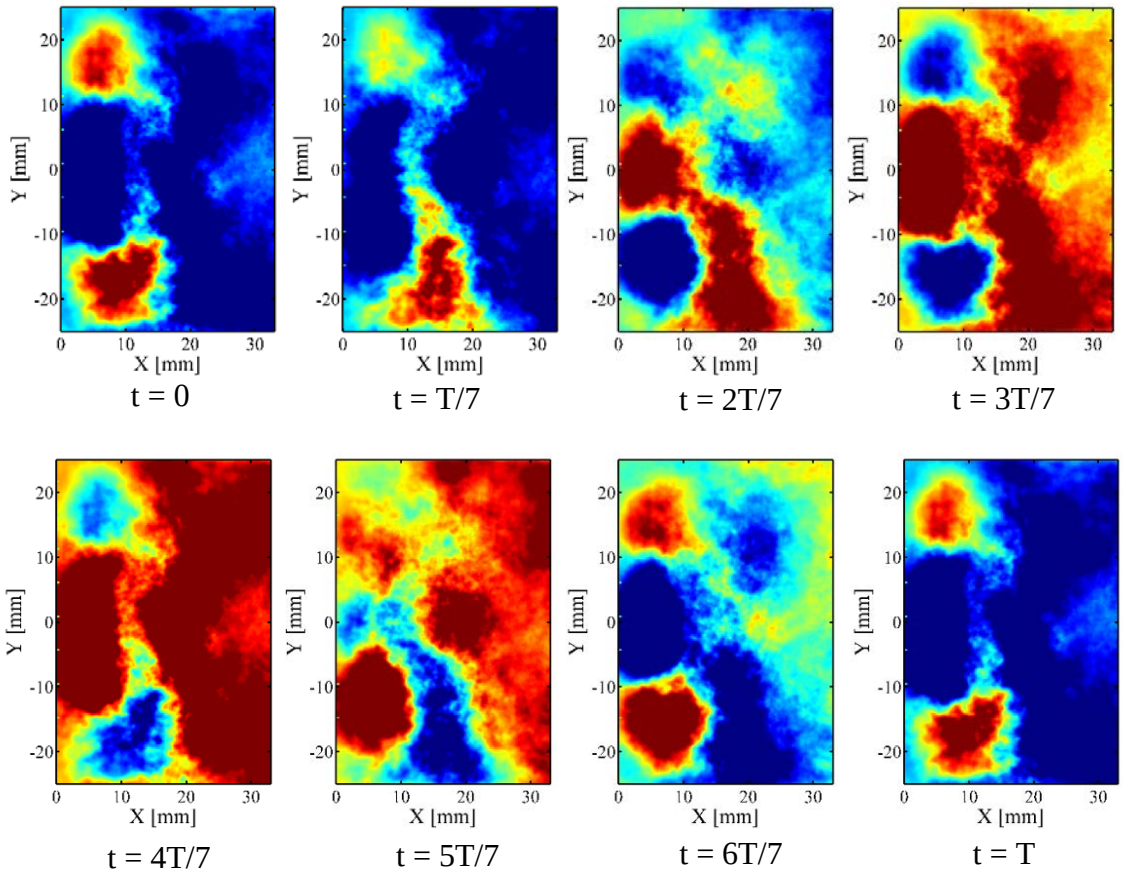

Figure 5.17: OH-PLIF images reconstructed from the DMD mode for an acoustic cycle at the 4L frequency of 1459 Hz (Tair = 800 K, ϕ = 0.6)

Figure 5.18 shows snapshots representing one acoustic cycle (0 to T s) for ϕ = 0.44 case, starting from maximum of the OH signal at t = 0 to a local minimum of the OH-signal at t = T/2 and back to a maximum OH-signal at the end of the cycle for the 1012 Hz DMD spatial mode. The separation in time between snapshots is 1 ms. At t=0, the OH-signal is at its maximum and the high intensity regions are present near the periphery of the combustor. Two smaller lobes of lower intensity are concurrently present more than 10 mm removed from the dump plane near the central axis of the combustor inside the higher intensity regions. As the cycle progresses, these lobes are pushed out towards the periphery and higher intensity regions from the flame are transported towards the center of the

combustor from t= 2T/10 through t=T/2. At t=T/2, the OH-signal is at its minimum near the dump plane. At this instant the local expansion draws more fuel and air into the combustor near the central axis of the combustor while the burnt gases travel back towards the periphery preheating the reactants. At t=9T/10 the OH-signal is almost at its highest point again and the cycle is repeated thereafter.

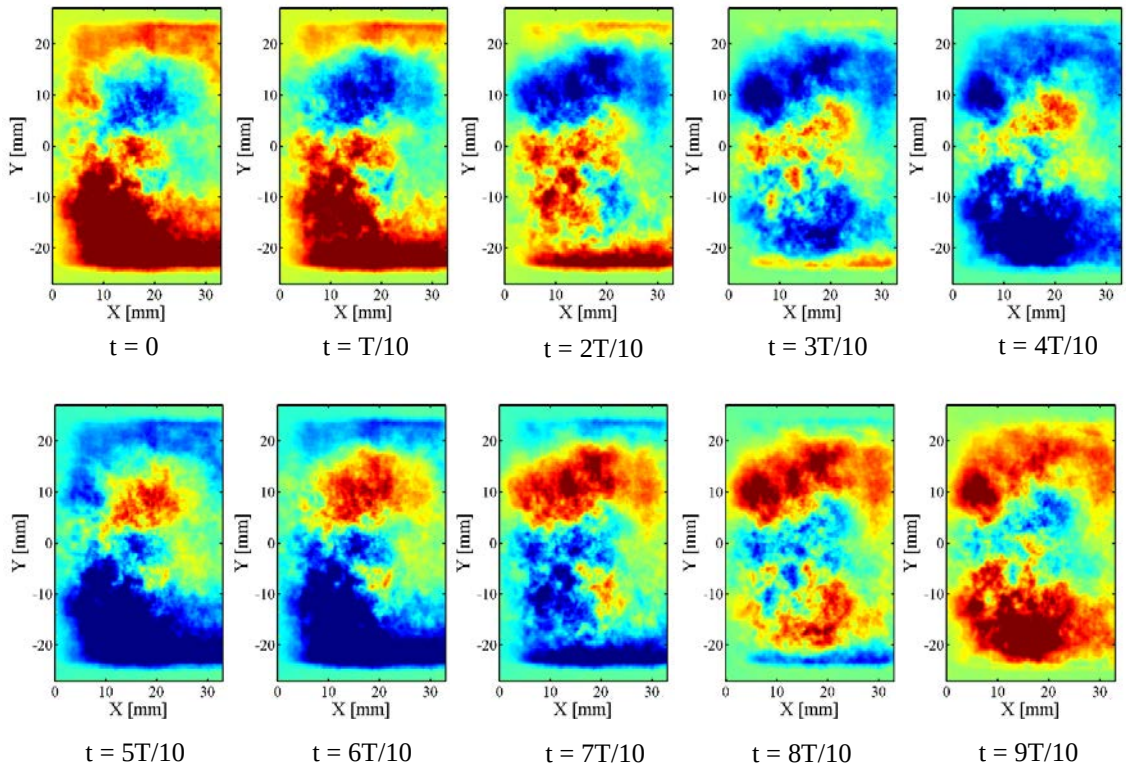

Figure 5.18: OH-PLIF images reconstructed from the DMD mode for an acoustic cycle at the 3L frequency of 1012 Hz (Tair = 800 K, ϕ = 0.6)

5.4.5.1 Analysis of Raw Corrected Images:

Corrected OH-PLIF images over a course of 2.4 ms (one cycle at the 4L mode is 4 frames) are shown in Figure 5.19 and Figure 75 below for ϕ = 0.6 and ϕ = 0.44 cases respectively. For ϕ = 0.6, the images show a V-shaped flame that is anchored close to the dump plane of the combustor. The presence of multiple modes, from ~300 Hz to 7 kHz makes tracking

distinct flame structures from snapshot to snapshot difficult. As such tracking of flow structures without use of decomposition techniques such as DMD is difficult in such flows with large number of unsteady modes.

For the $\phi = 0.44$ test case, the significant modulation in the pressure fluctuation amplitude across the 1L-5L modes and consequently the flame shape makes it difficult to track a particular mode or structure through the image sequence. The main conclusion that can be drawn from the sequence of images is that the flame is always lifted off 5-10 mm from the dump plane of the combustor.

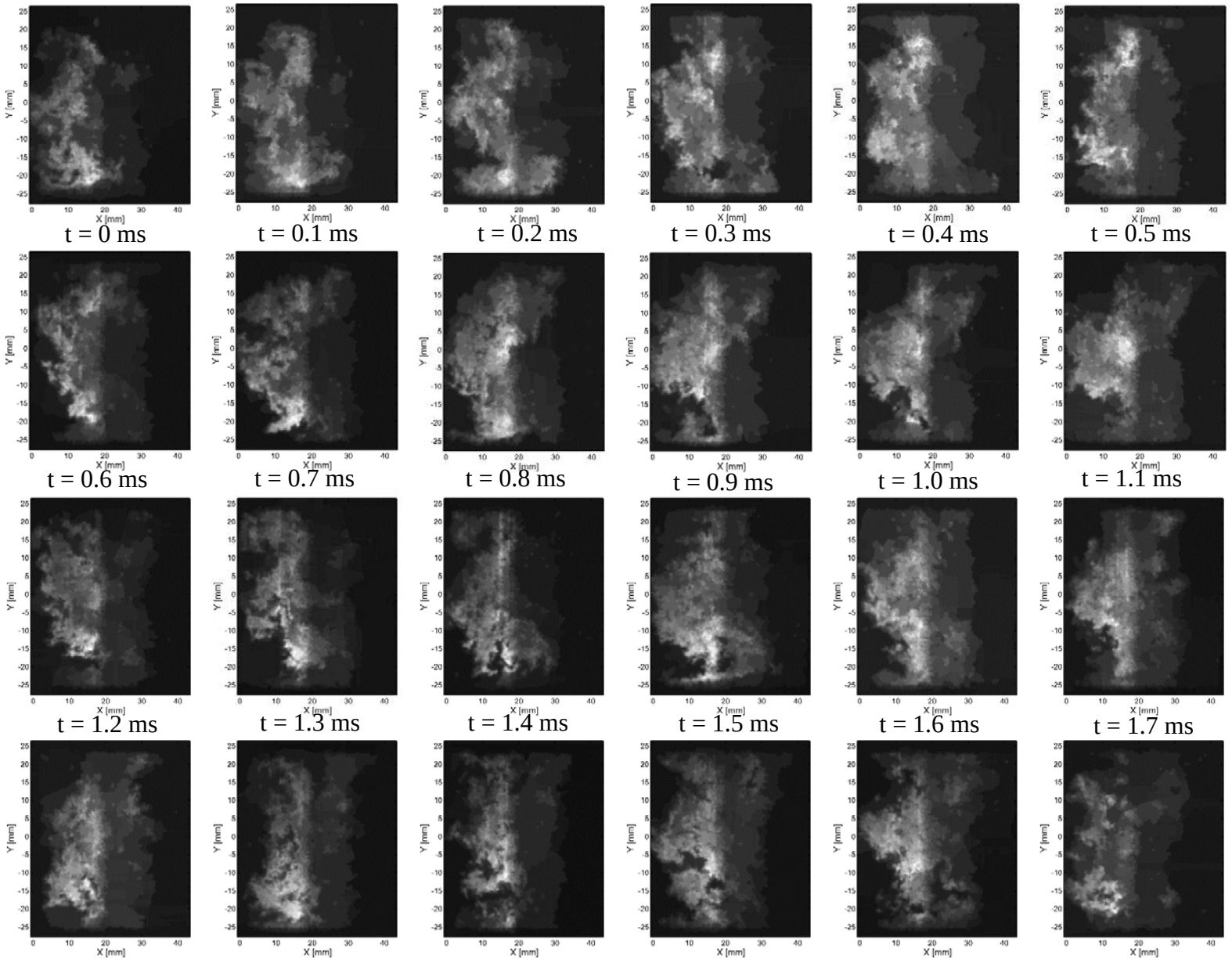

Figure 5.19: Instantaneous snapshots of the OH-PLIF signal over a 2.4 ms time period (Tair = 800 K, ϕ = 0.6)

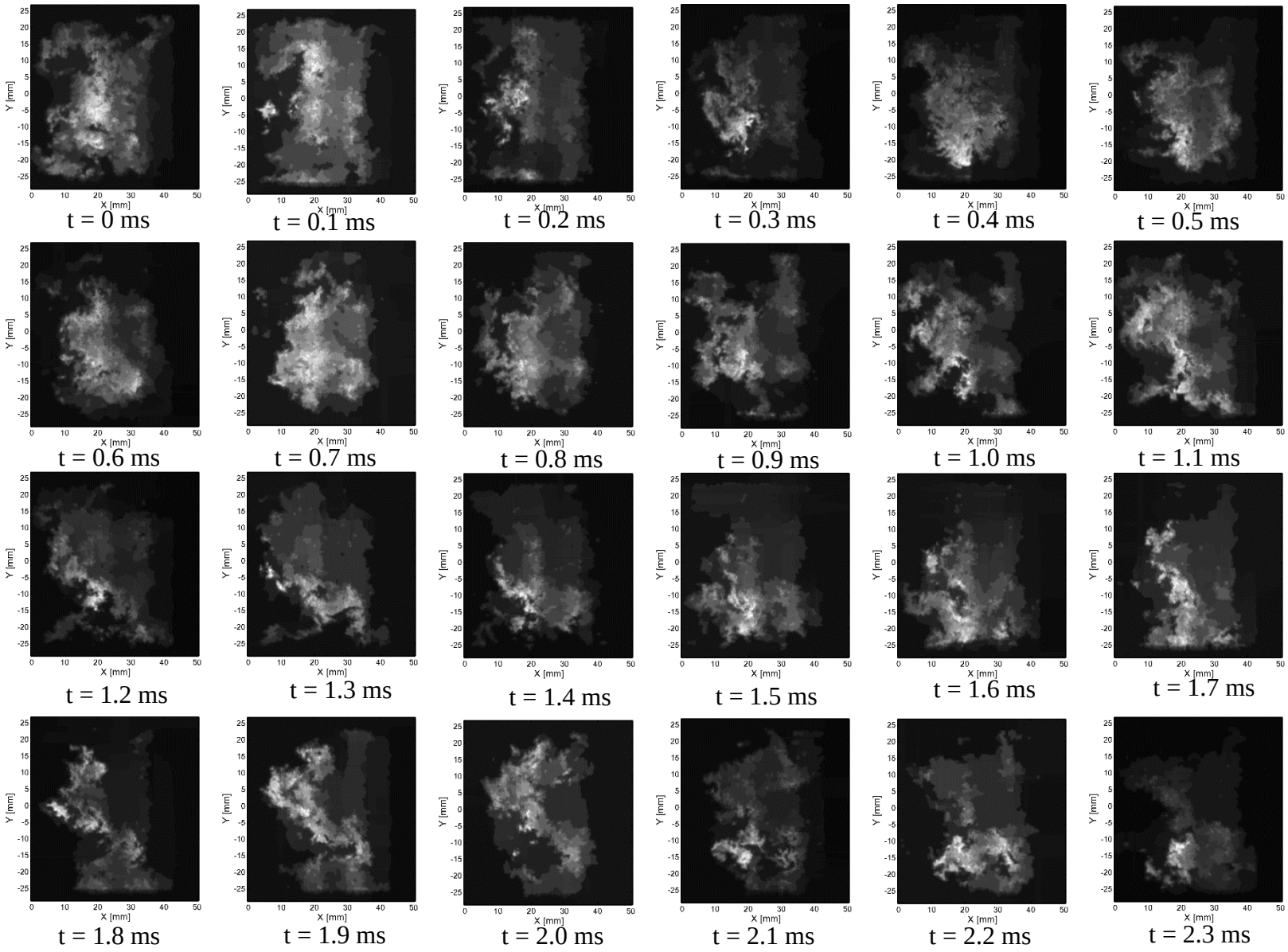

Figure 5.20: Instantaneous snapshots of the OH-PLIF signal over 2.4 ms (Tair = 800 K, ϕ = 0.44)

5.5 PIV Measurements:

The inherent limitations of the OH-PLIF and chemiluminescence based techniques, making quantitative conclusions of heat release of species concentrations in the reacting flow difficult. PIV remains the most promising technique for direct and spatio-temporally quantitative technique for comparison with simulations. Two-dimensional PIV does introduce a degree of uncertainty in the results when a highly three dimensional swirling flow present in the LDI combustor is diagnosed.

Non-reacting and reacting flow tests were attempted using particle imaging velocimetry at 5 kHz in the LDI combustor. As reported in Chapter 3, the PIV measurements were challenging on account of a fairly small diameter quartz tube, that promoted multiple reflections of the 532 nm laser sheet of them leading to a glare that contaminated the scattered light signal off the TiO_2 seed particles. The condition at which the tests were performed and the field of view are presented below.

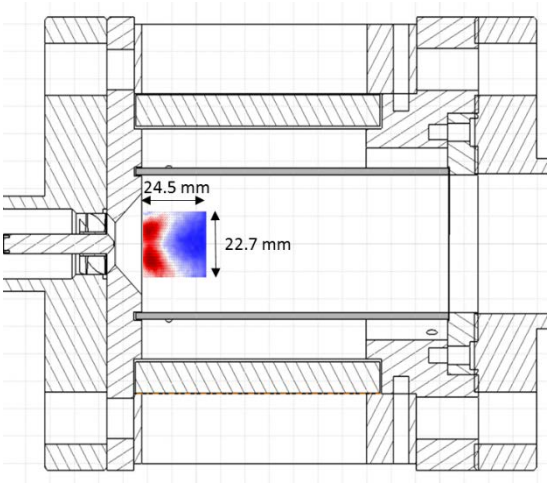

Figure 5.21. Field of view for the PIV tests. Limited viewing area to avoid regions where glare from the window affected test results.

Table 5.3. Operating conditions for the PIV tests

Test Case	Air temperature (K)	Equivalence Ratio (ϕ)	Laser energy per pulse (mJ)	Pulse separation (μs)
Non-reacting tests	600,640,750,770	NA	4	2, 4
Reacting cases	780	0.45, 0.48, 0.52	6	2, 4

The results for the test near lean blow-out at an equivalence ratio of 0.45 and an air temperature of 780 K are shown below. The pulse separation for the test case for 4 μs. Only mean axial velocity field and the vorticity in the z-direction are presented. The axial velocity field shows jets issuing out of the CD nozzle in a V-shape and a lower velocity region downstream of it representative of the vortex breakdown bubble. The vorticity field shows the swirling motion of the flow-field. The -10 mm location on the x-axis is the location of the combustor dump-plane and the -5 mm location on the y-axis is the location of the combustor center-line. The flow is from left to right in the images. The axial velocity is shown on the left and the vorticity on the right in Figure 5.22. The quantitative results are not presented in detail because the seeding density and the time separation between pules was not suitable for the flow-field in this case. The end of the project duration and request for test hardware by NASA Glenn precluded further tests to obtain better PIV and simultaneous PLIF-PIV data.

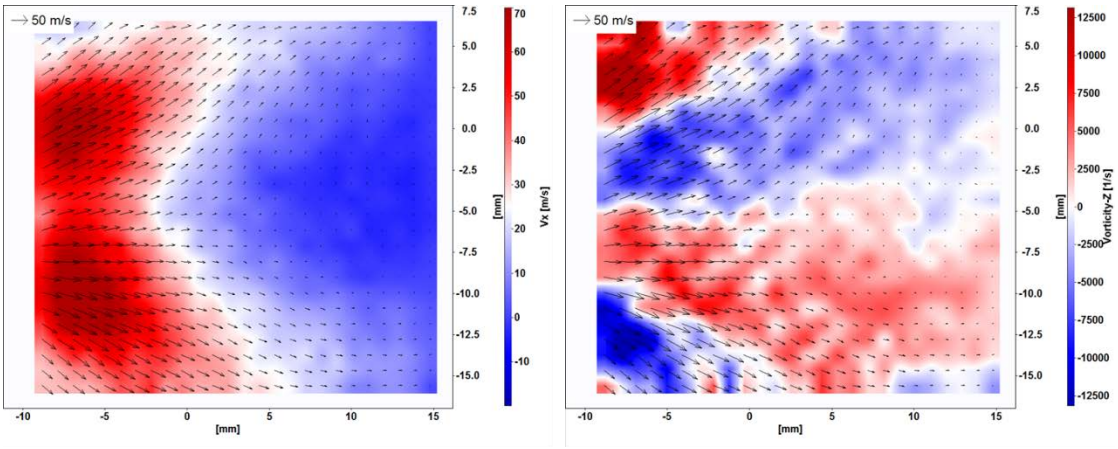

Figure 5.22. Mean axial velocity field (m/s) (left) and vorticity field (1/s) (right) in the LDI chamber for reacting test case with an inlet air temperature of 780 K and an equivalence ratio of 0.45. The test was conducted in the baseline configuration of the combustor.

5.6 Summary

A good qualitative agreement in macroscopic parameters such as measured pressure instability amplitudes, a quantitative agreement in dominant modes identified and a temporal agreement between OH-PLIF intensity and OH-mass fraction between experiments and simulations is observed which provides confidence in the high-fidelity measurements. The comparison of spatial mode-shapes at this stage are only qualitative and experimental measurements do not show detailed flame features and hydrodynamic structures to the same degree of detail as the simulations. A necessity of 3D simulations to accurately depict the physics of an inherently 3D swirl stabilized flame was also established through the comparison presented above. The amplitude and presence of modes between a selected 2D slice of data and a 3D dataset showed similarities at the 1 kHz mode frequency

in the 2-step chemistry simulations while the 1 kHz mode was seen to be damped in the 18-step simulations.

A gradient-based edge detection routine was used to extract the flame-front location from the OH-PLIF images. Planar flame surface density calculated using the extracted flame-front showed a compact flame (L_f ~ 25 mm) at ϕ=0.6 and a more diffuse flame (L_f ~ 35 mm) at ϕ=0.44. Dynamic mode decomposition (DMD) analysis of the flame front shows a strong flame response at the 4L and 8L acoustic mode frequencies for ϕ=0.6 and at the 3L frequency for ϕ=0.44, while a response at the other acoustic mode frequencies is not captured. PIV measurements were performed at 5 kHz for non-reacting flow but glare from the cylindrical quartz chamber limited the field of view to a small region in the combustor.

CHAPTER 6. SUMMARY, CONCLUSIONS AND RECOMMENDATIONS FOR FUTURE WORK

6.1 Summary and Conclusions

The thesis presented an experimental study of self-excited longitudinal mode combustion instabilities in a single element Lean Direct Injection (LDI) combustor. The primary objective of the study was to generate validation data to assess the ability of high-fidelity models to predict combustion dynamics in lean-burning systems, and use it to further the physical understanding of the complex flame-acoustic-hydrodynamic interactions in the multi-phase, unsteady, turbulent flow-field of the LDI chamber. Initial experiment goals included generation of pressure oscillation levels of about 1% of mean pressure, and at a frequency of about 400 Hz. Strict requirements were placed on self-excitation, boundary conditions, measurement accuracy, and optical access to the combustion zone to allow generated data to be directly comparable to concurrent simulations efforts. A prototypical lean-direct-inject combustor was designed in a modular configuration so that a suitable geometry could be found by test. The combustor comprised a variable length air plenum and combustion chamber, air swirler, and fuel nozzle located inside a subsonic venturi. The venturi cross section and the fuel nozzle were consistent with previous studies.

Mean test pressure was 1 MPa and variables included geometry and acoustic resonance, inlet temperatures, equivalence ratio, and type of liquid fuel. High-frequency pressure measurements in a well-instrumented metal chamber yielded frequencies and mode shapes as a function of inlet air temperature, equivalence ratio, fuel nozzle placement, and combustor acoustic resonances. The parametric survey was a significant effort, with over 105 tests on eight geometric configurations. This survey of the self-excited LDI combustor showed distinct and discriminating instability characteristics that point to coupling processes between heat release, acoustics and multi-phase hydrodynamics.

Results showed a strong dependence of instability amplitude on the geometric configuration of the combustor, i.e., its acoustic resonance characteristics, with measured pressure fluctuation amplitudes ranged from 5 kPa (0.5% of mean pressure) to 200 kPa (~20% of mean pressure) depending on combustor geometry. Larger combustion instability amplitudes were observed at higher equivalence ratios with strong fluctuations at the 4L mode frequency while the lowest amplitudes were observed near lean blow-out conditions where the mode energy was spread across 1L-5L modes. A strong correlation was also observed between the inlet air temperature and instability levels with higher temperature resulting in lower pressure amplitudes. It is speculated that the lower temperatures result in lower droplet evaporation rates, non-uniform fuel distribution and spatio-temporal modification of the burning rate that lead to higher levels of combustion instabilities.

The 1/4 wave air plenum (L_c = 0.2 m) and 1/4 wave combustion chamber (L_c = 0.56 m) was the most unstable combustor configuration with peak-to-peak pressure fluctuations as

high as 20% of the mean chamber pressure. Generally, the dominant mode in the combustor was between 1200 -1600 Hz corresponding to the 4L mode in the combustor. Higher frequency modes in the 6-8 kHz range are also observed with high pressure fluctuation amplitudes, comparable to the 4L mode amplitude at high equivalence ratios.

The 3/8 wave air plenum (L_p = 0.46 m) and 1/2 wave combustion chamber (L_c = 1.08 m) length was selected as the base configuration that presented combustion instability amplitudes close to the target (1-3% P'/Pc) at high air temperature and low equivalence ratio. For the base configuration, the combustion instabilities with fuel nozzle at the throat of the venturi throat were stronger than with the configuration with fuel nozzle 2.6 mm upstream of the nozzle. Since the highest velocities of the swirling air flow are present at the throat, any acoustics based oscillations can have a greater effect by small variations of fuel injection location. At higher equivalence ratios, the 4L mode was dominant for both configurations with amplitudes between 40 and 82 kPa. At lower equivalence ratios, the energy was spread across the first five modes in the combustor, with the 1L mode dominant when fuel nozzle was upstream while 5L mode dominant when fuel nozzle was at the throat.

At the low amplitude instability conditions at lower equivalence ratios, a strong modulation in the dynamic pressure is observed. Dynamic pressure energy is distributed across several (1L-5L) low amplitude modes in the combustor. The significant difference in the energy spectrum between the high equivalence ratio cases where a dominant 4L mode is observed versus the low equivalence ratio case indicates possibility of different driving/damping mechanism at the two equivalence ratios ranges.

At higher equivalence ratio, where the combustor was relatively unstable, bands of modes around 1400 Hz and 6 kHz were prevalent, with the 4L mode typically being the most dominant mode. At the most stable conditions, near lean blow-out, acoustic energy was distributed across several (1L-5L) low amplitude modes. An increase in the 1L mode amplitude coincided with the reduction in strength of the other modes. A strong modulation in the dynamic pressure is present, with oscillations ranging from 0.5% to 2% of mean pressure. The difference in the energy spectrum between the high-equivalence-ratio cases, with a dominant 4L mode, and the low equivalence ratio case with more dispersed modal energy provided a good test for the simulation. A pronounced effect of fuel nozzle location on the combustion dynamics was also observed. Combustion instabilities with the fuel nozzle at the throat of the venturi throat were stronger than in the configuration with fuel nozzle 2.6 mm upstream of the nozzle.

A phase Doppler particle analyzer (PDPA) was used to measure the drop size distribution and droplet velocities for an unconfined spray at atmospheric pressure. The measurements were performed with and without a co-flow of air around the fuel nozzle. Drop sizes of 15-70 μm, axial droplet velocities up to 15 m/s and a spray cone angle of 68-70° were measured. Simulations at the conditions of the spray experiment were performed in which the measured spray cone angle and drop sizes were input to the model. Use of atmospheric pressure drop size measurements as input to the simulation did not provide the results that matched the high pressure, reacting flow measurements. Good spray measurements for the multi-distillate fuels used in this study at high pressure, reacting flow conditions are needed to provide appropriate data for model validations.

A second set of dynamics data was based on high-response-rate laser-based combustion diagnostics using an optically accessible combustor section. High-frequency measurements of OH*-chemiluminescence and OH-PLIF and velocity fields using PIV were obtained at a relatively stable, low equivalence ratio case and a less stable case at higher ϕ. A gradient-based edge detection routine was used to extract the flame-front location from the OH-PLIF images. Planar flame surface density calculated using the extracted flame-front showed a compact flame (L_f ~ 25 mm) at ϕ=0.6 and a more diffuse flame (L_f ~ 35 mm) at ϕ=0.44. Dynamic mode decomposition analysis of the flame front shows a strong flame response at the 4L and 8L acoustic mode frequencies for ϕ=0.6 and at the 3L frequency for ϕ=0.44, while a response at the other acoustic mode frequencies was not captured. PIV measurements were performed at 5 kHz for non-reacting and reacting flow experiments but glare from the cylindrical quartz chamber limited the field of view to a small region in the combustor. The limited PIV data did show indications of a V-shaped flame and a vortex breakdown bubble downstream of it.

Quantitative and qualitative comparisons were made for five different combinations of geometry and operating condition that yielded discriminating stability behavior in the experiment with simulations that were carried out concurrently. Comparisons were made on the basis of trends and pressure mode data as well as with OH-PLIF measurements for the baseline geometry at ϕ=0.44 and 0.6 equivalence ratios. Overall, the ability of the simulation to match experimental data and trends was encouraging. Dynamic Mode Decomposition (DMD) analysis was performed on two sets of computations - a global 2-step chemistry mechanism and an 18-step chemistry mechanism - and the OH-PLIF images to allow comparison of dynamic patterns of heat release and OH distribution in the

combustion zone. The DMD analysis was able to identify similar dominant unstable modes in the combustor. The 4L acoustic mode showed highest amplitude in the pressure signal as well as heat release and OH signal intensity in both experiment and simulations. The DMD spatial mode-shapes at 480 Hz, ~ 1 kHz and at the 4L mode were qualitatively similar in the experiment and simulations.

A qualitative agreement between the OH-PLIF measurements and the simulations in terms of the flame surface density, spatial mode-shapes and good agreement in measured pressure instability amplitudes was observed and provides confidence in the high-fidelity measurements. The necessity of 3D simulations to accurately depict the physics of an inherently 3D swirl stabilized flame was established. The amplitude and presence of modes between a selected 2D slice of data and a 3D dataset showed similarities at the 1 kHz mode frequency in the 2-step chemistry simulations while the 1 kHz mode was seen to be damped in the 18-step simulations.

6.2 Recommendations for Future Work

The present study is part of a long-term effort at Purdue University comprising a hierarchy of experiments, analysis, and simulations that are combined to produce accurate and reliable predictions of combustion dynamics in full-scale systems. Development of an accurate and robust predictive capability for combustion dynamics is critically dependent on the availability of relevant experimental data for validation at multiple levels ranging from unit physics to the system level. Though a fair amount of work has been done to investigate the unit-physics that lead to self-excited instabilities in a high pressure single-element LDI combustor and generate high-fidelity data for validation efforts, there still remain several areas where the further investigation is necessary. Based on the results presented, it is clear that experimental resources need to be invested in gathering quantitative, spatio-temporally resolved data over a large band-width covering mixing, kinetic, acoustic and geometric scales of the combustor to allow direct comparison with models. Recommendations based on the experience of combustor design, data generation and analysis and notable work carried out across the research community, at Purdue and otherwise is listed below.

1. Complex nonlinear coupling processes between heat release, acoustics, and hydrodynamics have been shown to exist in premixed-gas, sudden-expansion combustors with swirl. The swirling, expanding flows in the diverging venturi section with complicated acoustic reflections can introduce physics that are not easy to detect or understand. A systematic variation in geometry and swirl number that includes the

sudden expansion used in most canonical rear-ward facing step configurations may lead to a better understanding of these effects in the LDI configuration.

2. A gaseous fuel should be used to eliminate the complicated and complex behavior that comes from atomization, vaporization, and drop transport. Selection of the gaseous fuel can also be used to effectively modulate the degree of partial pre-mixing in the venturi to alter the flame stabilization location in the combustion chamber. This study can provide guidance to optimize the LDI configuration for both, low-NOx emissions as well as flame stability.

3. Future experiments should use test hardware designed for adiabatic operation so that the conditions in the simulations are better matched. Conversely, the heat loss through the combustor wall can also be measured as an input to the simulations to further approach a representation of real combustor configurations and used as input to models. The effect of chamber heat loss and its effect on combustion dynamics by using an adiabatic and a water-cooled wall can be performed.

4. OH-PLIF measurements at 10 kHz repetition rates were presented Chapter 5 along with a brief discussion of PIV results for a single test case at ϕ = 0.6. The PIV measurements remain the most encouraging quantitative measurements for a direct comparison with simulation results. The current PIV measurements were challenging on account of using a circular window as discussed previously in Chapter 5. A repetition of these measurements with anti-reflection (AR) coated quartz tube and

precise micrometer translation stages to align the laser sheet propagation through the window to eradicate any reflections (and glare) is recommended. The availability of pulse-burst laser with repetition rates up to 100 kHz provides the opportunity to diagnose the flow-field with high temporal and spatial resolution, even for the higher frequency modes in the 6-8 kHz range which was previously inaccessible at the 10 kHz measurements. This would further improve quantitative comparisons with the experiment.

5. The laser based diagnostics in this study, both OH-PLIF and PIV, were two-dimensional planar measurements applied to a three-dimensional flow-field with dominant swirling dynamics. T can lead to erroneous representation of data and physics in the chamber. Even when the computational data is processed to provide a direct comparison with the experiment, a slight mismatch in the results, which would generally be acceptable as uncertainty, can be outright wrong because of the 2-D measurement versus the 3-D flow-field. Future work should be extended to stereographic or tomographic measurements to alleviate these issues. While, expensive, a single test case comparison with computational results can build confidence in the planar measurements and ensure correct interpretation.

6. For the LDI configuration, a portion of the flame is present in the diverging section of the venturi, which was not accessible in this study. Fiber-optic-based emission measurements at key locations in the diverging section should be considered to

confirm the precessing vortex core instability that was conjectured to be the source of the 6-8 kHz instabilities.

7. The success of LDI as a concept for low dry-NOx combustors relies on multiple elements, individually and collectively distributed to ensure rapid and uniform mixing and combustion, to enable short flame zone and residence times. Consequently, along with intra-element dynamics, inter-element interaction can not only affect NOx formation but combustion dynamics over a large band-width of acoustic time-scales including high frequency dynamics, the kind that were observed in the single element study here. Design and study of a multi-element sub-scale combustor operating at relevant engine conditions and capable of generating self-excited combustion dynamics would aid in the understanding of the inter-element interactions and their role in combustion stability of the LDI concept.

LIST OF REFERENCES

LIST OF REFERENCES

[1] ICAO, *Report of the independent experts on the LTTG NOx review and medium and long term technology goals for NOx.* ICAO Document 9887, 2008.

[2] Correa, S.M., *A Review of NOx Formation Under Gas-Turbine Combustion Conditions.* Combustion Science and Technology, 1993. **87**(1-6): p. 329-362.

[3] Turns, S.R., *An Introduction to Combustion: Concepts and Applications*. 2000: McGraw-Hill Higher Education.

[4] Bowman, C.T., *Control of combustion-generated nitrogen oxide emissions: Technology driven by regulation.* Symposium (International) on Combustion, 1992. **24**(1): p. 859-878.

[5] Fenimore, C.P. and G.W. Jones, *Rate of the reaction, $O+N2O \rightarrow 2NO$.* Symposium (International) on Combustion, 1961. **8**(1): p. 127-133.

[6] Fenimore, C.P., *Formation of nitric oxide in premixed hydrocarbon flames.* Symposium (International) on Combustion, 1971. **13**(1): p. 373-380.

[7] Kim, K.T., et al., *Spatially distributed flame transfer functions for predicting combustion dynamics in lean premixed gas turbine combustors.* Combustion and Flame, 2010. **157**(9): p. 1718-1730.

[8] Rayleigh, L., *Theory of Sound: V. 2*. 1900: Dover Publications.

[9] Lieuwen, T., Yang, V., *Combustion Instabilities: Basic Concepts*, in *Combustion Instabilities In Gas Turbine Engines: Operational Experience, Fundamental Mechanisms, and Modeling*. 2006, American Institute of Aeronautics and Astronautics. p. 3-26.

[10] Nicoud, F. and T. Poinsot, *Thermoacoustic instabilities: Should the Rayleigh criterion be extended to include entropy changes?* Combustion and Flame, 2005. **142**(1–2): p. 153-159.

[11] Durox, D., et al., *Rayleigh criterion and acoustic energy balance in unconfined self-sustained oscillating flames.* Combustion and Flame, 2009. **156**(1): p. 106-119.

[12] Alkabie, H., G. Andrews, and N. Ahmad. *Lean Low NOx Primary Zones Using Radial Swirlers, paper ASME 88-GT-245*. in *ASME Gas Turbine and Aero Engine Congress and Exposition*. 1988.

[13] Hussain, U.S.A., G.E. Andrews, and W.G.S. Cheung, A.R., *Low NOx primary zones using jet mixing shear layer combustion*. 1988. Medium: X; Size: Pages: (11 p).

[14] Andrews, G.E., et al., *High-Intensity Burners with Low Nox Emissions.* Proceedings of the Institution of Mechanical Engineers, Part A: Journal of Power and Energy, 1992. **206**(1): p. 3-17.

[15] Gerhold, B.W., C.P. Fenimore, and P.K. Dederick, *Two-stage combustion of plain and N doped oil.* Symposium (International) on Combustion, 1979. **17**(1): p. 703-713.

[16] Rizk, N. and M. Mongia, *NO(x) model for lean combustion concept*, in *28th Joint Propulsion Conference and Exhibit*. 1992, American Institute of Aeronautics and Astronautics.

[17] Mongia, H., *Correlations for Gaseous Emissions of Aero-Propulsion Engines from Sea-Level to Cruise Operation*, in *48th AIAA Aerospace Sciences Meeting Including the New Horizons Forum and Aerospace Exposition*. 2010, American Institute of Aeronautics and Astronautics.

[18] McDonell, V., *Chapter 5 - Lean Combustion in Gas Turbines*, in *Lean Combustion*, D.-R. Derek, Editor. 2008, Academic Press: Burlington. p. 121-IV.

[19] Clayton, C., and N.M. Laurendeau, *Quantitative measurements of nitric oxide in high-pressure (2–5 atm), swirl-stabilized spray flames via laser-induced fluorescence.* Combustion and Flame, 2000. **123**(1–2): p. 175-188.

[20] Tacina, R., *Low NO(x) potential of gas turbine engines*, in *28th Aerospace Sciences Meeting*. 1990, American Institute of Aeronautics and Astronautics.

[21] Anderson, D. *Ultra Lean Combustion at High Inlet Temperatures, ASME Paper 81-GT-44*. in *Gas Turbine Conference & Products Show*. 1981.

[22] Tacina, R., Mao, Chien-Pei, and Wey, C., *Experimental Investigation of a Multiplex Fuel Injector Module with Discrete Jet Swirlers for Low Emission Combustors*, in *42nd AIAA Aerospace Sciences Meeting and Exhibit*. 2004, American Institute of Aeronautics and Astronautics.

[23] Tacina, R., Mao, Chien-Pei, and Wey, C., *Experimental Investigation of a Multiplex Fuel Injector Module for Low Emission Combustors*, in *41st Aerospace Sciences Meeting and Exhibit*. 2003, American Institute of Aeronautics and Astronautics.

[24] Locke, R.J., et al., *OH imaging in a lean burning high-pressure combustor*. AIAA Journal, 2010. **34**(3): p. 622-624.

[25] Thariyan, M.P., et al., *Dual-Pump CARS Temperature and Major Species Concentration Measurements in a Gas Turbine Combustor Facility*, in *45th AIAA/ASME/SAE/ASEE Joint Propulsion Conference & Exhibit*. 2009, American Institute of Aeronautics and Astronautics.

[26] Thariyan, M.P., et al., *Dual-Pump CARS Measurements in a Gas Turbine Combustor Facility Using the NASA 9-Point Lean Direct Injector*, in *48th AIAA Aerospace Sciences Meeting Including the New Horizons Forum and Aerospace Exposition*. 2010, American Institute of Aeronautics and Astronautics.

[27] Thariyan, M.P., et al., *DP-CARS and OH-PLIF Measurements at Elevated Pressures in a Gas Turbine Combustor Facility (Invited)*, in *27th AIAA Aerodynamic Measurement Technology and Ground Testing Conference*. 2010, American Institute of Aeronautics and Astronautics.

[28] Thariyan, M.P., *Coherent anti-Stokes Raman scattering for quantitative temperature and concentration measurements in a high-pressure gas turbine combustor rig*. 2010, Purdue University: West Lafayette, IN. p. 339.

[29] Thariyan, M.P., et al., *Dual-pump CARS temperature and major species concentration measurements in counter-flow methane flames using narrowband pump and broadband Stokes lasers*. Combustion and Flame, 2010. **157**(7): p. 1390-1399.

[30] Gore, J., *NOx reduction using lean direct injection in naval engines*, in *31st Joint Propulsion Conference and Exhibit*. 1995, American Institute of Aeronautics and Astronautics.

[31] Dewanji, D. and A.G. Rao, *Spray Combustion Modeling in Lean Direct Injection Combustors, Part I: Single-Element LDI.* Combustion Science and Technology, 2014. **187**(4): p. 537-557.

[32] Dewanji, D., and A.G. Rao, *Spray Combustion Modeling in Lean Direct Injection Combustors, Part II: Multi-Point LDI.* Combustion Science and Technology, 2014. **187**(4): p. 558-576.

[33] Yi, T., and Santavicca, D., *Flame Spectra of a Turbulent Liquid-Fueled Swirl-Stabilized LDI Combustor*, in *47th AIAA Aerospace Sciences Meeting including The New Horizons Forum and Aerospace Exposition*. 2009, American Institute of Aeronautics and Astronautics.

[34] Yi, T., and Santavicca, D., *Combustion Instability in a Turbulent Liquid-Fueled Swirl-Stabilized LDI Combustor*, in *45th AIAA/ASME/SAE/ASEE Joint Propulsion Conference & Exhibit*. 2009, American Institute of Aeronautics and Astronautics.

[35] Yi, T. and D.A. Santavicca, *Flame Spectra of a Turbulent Liquid-Fueled Swirl-Stabilized Lean-Direct Injection Combustor*. Journal of Propulsion and Power, 2012. **25**(5): p. 1058-1067.

[36] Meadows, J.W. and A.K. Agrawal, *Porous Inserts for Passive Control of Noise and Thermo-Acoustic Instabilities in LDI Combustion.* Combustion Science and Technology, 2014: p. null-null.

[37] Meadows, J. and A.K. Agrawal, *Time-resolved PIV of lean premixed combustion without and with porous inert media for acoustic control.* Combustion and Flame, 2015. **162**(4): p. 1063-1077.

[38] de la Cruz García, M., E. Mastorakos, and A.P. Dowling, *Investigations on the self-excited oscillations in a kerosene spray flame.* Combustion and Flame, 2009. **156**(2): p. 374-384.

[39] Kim, K.T. and D.A. Santavicca, *Interference mechanisms of acoustic/convective disturbances in a swirl-stabilized lean-premixed combustor.* Combustion and Flame, 2013. **160**(8): p. 1441-1457.

[40] Tachibana, S., et al., *Experimental and numerical investigation of thermo-acoustic instability in a liquid-fuel aero-engine combustor at elevated pressure: Validity of large-eddy simulation of spray combustion.* Combustion and Flame, 2015. **162**(6): p. 2621-2637.

[41] Anderson, A., and Winter, M., *Measurements of the effect of acoustic disturbances on droplet vaporization rates,* in *30th Aerospace Sciences Meeting and Exhibit*. 1992, American Institute of Aeronautics and Astronautics.

[42] Anderson, T., Kendrick, D., and Cohen, J., *Measurement of spray/acoustic coupling in gas turbine fuel injectors,* in *36th AIAA Aerospace Sciences Meeting and Exhibit*. 1998, American Institute of Aeronautics and Astronautics.

[43] Lee, D., and Anderson, T.,, *Measurements of fuel/air-acoustic coupling in lean premixed combustion systems,* in *37th Aerospace Sciences Meeting and Exhibit*. 1999, American Institute of Aeronautics and Astronautics.

[44] Anderson, W.E., et al., *Effects of Periodic Atomization on Combustion Instability in Liquid-Fueled Propulsion Systems*. Journal of Propulsion and Power, 2005. **14**(5): p. 818-825.

[45] Chishty, W.A., et al. *Effects of Combustor Acoustics on Fuel Spray Dynamics*. in *Proceedings of the 2004 ASME International Mechanical Engineering Congress and Exposition*. 2004.

[46] Chishty, W.A., *Effects of thermoacoustic oscillations on spray combustion dynamics with implications for lean direct injection systems*. 2005, NASA.

[47] Jun, C., Jeng, San-Mou, and Tacina, R., *The Structure of a Swirl-Stabilized Reacting Spray Issued from an Axial Swirler*, in *43rd AIAA Aerospace Sciences Meeting and Exhibit*. 2005, American Institute of Aeronautics and Astronautics.

[48] Yongqiang, F., J. San-Mou, and Tacina, R., *Confinement Effects on the Swirling Flow Generated by a Helical Axial Swirler*, in *44th AIAA Aerospace Sciences Meeting and Exhibit*. 2006, American Institute of Aeronautics and Astronautics.

[49] Yongqiang, F. and Jeng, San-Mou, *Experimental Investigation of Swirling Air Flows in a Multipoint LDI Combustor*, in *43rd AIAA/ASME/SAE/ASEE Joint Propulsion Conference & Exhibit*. 2007, American Institute of Aeronautics and Astronautics.

[50] Yongqiang, F., Jeng, San-Mou, and Tacina, R., *Characteristics of the Swirling Flow in a Multipoint LDI Combustor*, in *45th AIAA Aerospace Sciences Meeting and Exhibit*. 2007, American Institute of Aeronautics and Astronautics.

[51] Stöhr, M., et al., *Dynamics of lean blowout of a swirl-stabilized flame in a gas turbine model combustor*. Proceedings of the Combustion Institute, 2011. **33**(2): p. 2953-2960.

[52] Paschereit, C.O., E. Gutmark, and W. Weisenstein, *Excitation of Thermoacoustic Instabilities by Interaction of Acoustics and Unstable Swirling Flow*. AIAA Journal, 2000. **38**(6): p. 1025-1034.

[53] Sé, et al., *Combustion Dynamics and Instabilities: Elementary Coupling and Driving Mechanisms.* Journal of Propulsion and Power, 2003. **19**(5): p. 722-734.

[54] Stöhr, M., R. Sadanandan, and W. Meier, *Experimental study of unsteady flame structures of an oscillating swirl flame in a gas turbine model combustor*. Proceedings of the Combustion Institute, 2009. **32**(2): p. 2925-2932.

[55] Boxx, I., et al., *Temporally resolved planar measurements of transient phenomena in a partially pre-mixed swirl flame in a gas turbine model combustor*. Combustion and Flame, 2010. **157**(8): p. 1510-1525.

[56] Palies, P., et al., *The combined dynamics of swirler and turbulent premixed swirling flames.* Combustion and Flame, 2010. **157**(9): p. 1698-1717.

[57] Steinberg, A.M., et al., *Flow–flame interactions causing acoustically coupled heat release fluctuations in a thermo-acoustically unstable gas turbine model combustor*. Combustion and Flame, 2010. **157**(12): p. 2250-2266.

[58] Stopper, U., et al., *PIV, 2D-LIF and 1D-Raman measurements of flow field, composition and temperature in premixed gas turbine flames.* Experimental Thermal and Fluid Science, 2010. **34**(3): p. 396-403.

[59] Galley, D., et al., *Mixing and stabilization study of a partially premixed swirling flame using laser induced fluorescence.* Combustion and Flame, 2011. **158**(1): p. 155-171.

[60] Oberleithner, K., et al., *Three-dimensional coherent structures in a swirling jet undergoing vortex breakdown: stability analysis and empirical mode construction.* Journal of Fluid Mechanics, 2011. **679**: p. 383-414.

[61] Stöhr, M., R. Sadanandan, and W. Meier, *Phase-resolved characterization of vortex–flame interaction in a turbulent swirl flame.* Experiments in Fluids, 2011. **51**(4): p. 1153-1167.

[62] Candel, S., et al., *Progress and challenges in swirling flame dynamics.* Comptes Rendus Mécanique, 2012. **340**(11–12): p. 758-768.

[63] Moeck, J.P., et al., *Nonlinear interaction between a precessing vortex core and acoustic oscillations in a turbulent swirling flame.* Combustion and Flame, 2012. **159**(8): p. 2650-2668.

[64] Stöhr, M., et al., *Experimental study of vortex-flame interaction in a gas turbine model combustor.* Combustion and Flame, 2012. **159**(8): p. 2636-2649.

[65] Bourgouin, J.-F., et al., *Sensitivity of swirling flows to small changes in the swirler geometry.* Comptes Rendus Mécanique, 2013. **341**(1–2): p. 211-219.

[66] Durox, D., et al., *Flame dynamics of a variable swirl number system and instability control.* Combustion and Flame, 2013. **160**(9): p. 1729-1742.

[67] Hermeth, S., et al., *Bistable swirled flames and influence on flame transfer functions.* Combustion and Flame, 2013(0).

[68] Steinberg, A.M., C.M. Arndt, and W. Meier, *Parametric study of vortex structures and their dynamics in swirl-stabilized combustion.* Proceedings of the Combustion Institute, 2013. **34**(2): p. 3117-3125.

[69] Stöhr, M., C.M. Arndt, and W. Meier, *Effects of Damköhler number on vortex–flame interaction in a gas turbine model combustor*. Proceedings of the Combustion Institute, 2013. **34**(2): p. 3107-3115.

[70] Caux-Brisebois, V., et al., *Thermo-acoustic velocity coupling in a swirl stabilized gas turbine model combustor.* Combustion and Flame, 2014. **161**(12): p. 3166-3180.

[71] Stöhr, M., C.M. Arndt, and W. Meier, *Transient effects of fuel–air mixing in a partially-premixed turbulent swirl flame.* Proceedings of the Combustion Institute, 2015. **35**(3): p. 3327-3335.

[72] Syred, N., *A review of oscillation mechanisms and the role of the precessing vortex core (PVC) in swirl combustion systems.* Progress in Energy and Combustion Science, 2006. **32**(2): p. 93-161.

[73] Palies, P., et al., *Dynamics of premixed confined swirling flames.* Comptes Rendus Mécanique, 2009. **337**(6–7): p. 395-405.

[74] Palies, P., et al., *Nonlinear combustion instability analysis based on the flame describing function applied to turbulent premixed swirling flames.* Combustion and Flame, 2011. **158**(10): p. 1980-1991.

[75] Yi, T. and D. Santavicca, *Combustion Instability and Flame Structure of Turbulent Swirl-Stabilized Liquid-Fueled Combustion.* Journal of Propulsion and Power, 2003. **28**(5): p. 1000-1014.

[76] Roux, S., et al., *Studies of mean and unsteady flow in a swirled combustor using experiments, acoustic analysis, and large eddy simulations.* Combustion and Flame, 2005. **141**(1–2): p. 40-54.

[77] Franzelli, B., et al., *Large Eddy Simulation of combustion instabilities in a lean partially premixed swirled flame.* Combustion and Flame, 2012. **159**(2): p. 621-637.

[78] Patel, N., et al., *Simulation of spray combustion in a lean-direct injection combustor.* Proceedings of the Combustion Institute, 2007. **31**(2): p. 2327-2334.

[79] Patel, N. and S. Menon, *Simulation of spray–turbulence–flame interactions in a lean direct injection combustor*. Combustion and Flame, 2008. **153**(1–2): p. 228-257.

[80] Takeno, T. and M. Nishioka, *Species conservation and emission indices for flames described by similarity solutions.* Combustion and Flame, 1993. **92**(4): p. 465-468.

[81] Moeck, J., et al., *Tomographic reconstruction of heat release rate perturbations induced by helical modes in turbulent swirl flames.* Experiments in Fluids, 2013. **54**(4): p. 1-17.

[82] Eckbreth, A.C., *Laser diagnostics for combustion temperature and species*. Vol. 3. 1996: CRC Press.

[83] Raffel, M., et al., *Particle Image Velocimetry: A Practical Guide*. 2007.

[84] Coriton, B., A.M. Steinberg, and J.H. Frank, *High-speed tomographic PIV and OH PLIF measurements in turbulent reactive flows.* Experiments in Fluids, 2014. **55**(6): p. 1-20.

[85] Schmidt, J., et al., *kHz-rate particle-image velocimetry of induced instability in premixed propane/air flame by millisecond pulsed current–voltage.* Combustion and Flame, 2013. **160**(2): p. 276-284.

[86] Yoon, C., et al., *Computational Investigation of Combustion Instabilities in a Laboratory-Scale LDI Gas Turbine Engine*, in *49th AIAA/ASME/SAE/ASEE Joint PropulsionConference*. 2013, American Institute of Aeronautics and Astronautics.

[87] Yoon, C., Gejji, R., and Anderson, W., *Computational Investigation of Combustion Dynamics in a Lean Direct Injection Gas Turbine Combustor*, in *51st AIAA Aerospace Sciences Meeting including the New Horizons Forum and Aerospace Exposition*. 2013, American Institute of Aeronautics and Astronautics.

[88] Huang, C., et al., *Computational Study of Combustion Dynamics in a Single-Element Lean Direct Injection Gas Turbine Combustor*, in *52nd Aerospace Sciences Meeting*. 2014, American Institute of Aeronautics and Astronautics.

[89] Huang, C., et al., *Combustion Dynamics Behavior in a Single-Element Lean Direct Injection (LDI) Gas Turbine Combustor*, in *50th AIAA/ASME/SAE/ASEE Joint Propulsion Conference*. 2014, American Institute of Aeronautics and Astronautics.

[90] Huang, C., Gejji, R., and Anderson, W., *Effects of Physical Modeling on Combustion Instability Predictions in a Single-Element Lean Direct Injection Gas Turbine Combustor*, in *53rd AIAA Aerospace Sciences Meeting*. 2015, American Institute of Aeronautics and Astronautics.

[91] Gejji, R., et al., *Concurrent Experimental and Computational Study of Combustion Dynamics in a Single-Element Lean Direct Injection (LDI) Gas Turbine Combustor*, in *51st AIAA/SAE/ASEE Joint Propulsion Conference*. 2015, American Institute of Aeronautics and Astronautics.

[92] Anderson, W., and Meyer, S., *Propulsion Test Facilities at Purdue University*, in *38th AIAA/ASME/SAE/ASEE Joint Propulsion Conference & Exhibit*. 2002, American Institute of Aeronautics and Astronautics.

[93] Meyer, S., and Pourpoint, T., *Development of the Purdue University Integrated Gas Turbine Combustion Facility*, in *41st AIAA/ASME/SAE/ASEE Joint Propulsion Conference & Exhibit*. 2005, American Institute of Aeronautics and Astronautics.

[94] Pourpoint, T., Meyer, S., and Ehresman, C., *Propulsion Test Facilities at the Purdue University Maurice J. Zucrow Laboratories*, in *43rd AIAA/ASME/SAE/ASEE Joint Propulsion Conference & Exhibit*. 2007, American Institute of Aeronautics and Astronautics.

[95] Portillo, J., et al., *Application of a Generalized Instability Model to a Longitudinal Mode Combustion Instability*, in *43rd AIAA/ASME/SAE/ASEE Joint Propulsion Conference & Exhibit*. 2007, American Institute of Aeronautics and Astronautics.

[96] Yen, Y., et al., *Examination of Spatial Mode Shapes and Resonant Frequencies Using Linearized Euler Solutions*, in *37th AIAA Fluid Dynamics Conference and Exhibit*. 2007, American Institute of Aeronautics and Astronautics.

[97] Yen, Y., et al., *Effects of Mean Flow, Entropy Waves, and Boundary Conditions on Longitudinal Combustion Instability.* Combustion Science and Technology, 2010. **182**(7): p. 739-776.

[98] Gordon, S. and B.J. McBride, *Computer Program for Calculation of Complex Chemical Equilibrium Compositions and Applications,* in *NASA Reference Publication*. 1996.

[99] Stopper, U., et al., *Experimental study of industrial gas turbine flames including quantification of pressure influence on flow field, fuel/air premixing and flame shape.* Combustion and Flame, 2013. **160**(10): p. 2103-2118.

[100] Sadanandan, R., W. Meier, and J. Heinze, *Experimental study of signal trapping of OH laser induced fluorescence and chemiluminescence in flames.* Applied Physics B, 2012. **106**(3): p. 717-724.

[101] Delphine, S., et al., *Shear and Swirl Coaxial Injector Studies of LOX/GCH4 Rocket Combustion Using Non-Intrusive Laser Diagnostics,* in *44th AIAA Aerospace Sciences Meeting and Exhibit*. 2006, American Institute of Aeronautics and Astronautics.

[102] Frank, J., Miller, M., and Allen, M., *Imaging of laser-induced fluorescence in a high-pressure combustor,* in *37th Aerospace Sciences Meeting and Exhibit*. 1999, American Institute of Aeronautics and Astronautics.

[103] Weber, V., et al., *Pixel-based characterisation of CMOS high-speed camera systems.* Applied Physics B, 2011. **103**(2): p. 421-433.

[104] Slabaugh, C., A. Pratt, and R. Lucht, *Simultaneous 5 kHz OH-PLIF/PIV for the study of turbulent combustion at engine conditions.* Applied Physics B, 2014: p. 1-22.

[105] Boxx, I., et al., *3 kHz PIV/OH-PLIF measurements in a gas turbine combustor at elevated pressure.* Proceedings of the Combustion Institute, (0).

[106] Westbrook, C.K. and F.L. Dryer, *Simplified Reaction Mechanisms for the Oxidation of Hydrocarbon Fuels in Flames.* Combustion Science and Technology, 1981. **27**(1-2): p. 31-43.

[107] Kumud, A., Kundu, K., and Penko, P., *A Study on Detonation of Jet-A Using a Reduced Mechanism,* in *48th AIAA Aerospace Sciences Meeting Including the New Horizons Forum and Aerospace Exposition*. 2010, American Institute of Aeronautics and Astronautics.

[108] Schmid, P.J., *Dynamic mode decomposition of numerical and experimental data.* Journal of Fluid Mechanics, 2010. **656**: p. 5-28.

[109] Huang, C., et al., Analysis of Self-Excited Combustion Instabilities Using Decomposition Techniques. AIAA Journal, 2016: p. 1-17

[110] Shepherd, I.G., *Flame Surface Density and Burning Rate in Premixed Turbulent Flames,* Symposium (International) on Combustion, 1996: p. 373-379

VITA

VITA

Rohan M. Gejji was born in Pune, India in 1984. He graduated from University of Pune, Pune, India with a Bachelor's degree in Mechanical Engineering. After working in the automotive industry for a year, he joined Purdue University in Fall 2008 and completed his Master of Science in Mechanical Engineering degree in August 2011. Since then, he has been conducting research on the study of combustion dynamics in gas turbine and rocket combustion experiments under the guidance of Prof. William Anderson in the School of Aeronautics and Astronautics towards the completion of his doctoral degree.

After graduation, Rohan will continue his work on high-power turbulent combustion systems as a post-doctoral researcher at Purdue University.

.

PUBLICATIONS

PUBLICATIONS

Gejji, R., C. Huang, C. Yoon, C. Fugger, and W. Anderson (2016). Parametric Investigation of Combustion Instabilities in a Single Element Lean Direct Injection (LDI) Combustor. Combustion Science and Technology: *Under Review.*

Fugger, C., R. Gejji, J. Portillo, Y. Matsutomi, R. Lucht, and W. Anderson (2016). A model combustor for studying a reacting jet in an oscillating crossflow. Review of Scientific Instruments: *Under Review*.

Gejji, R., C. Huang, C. Slabaugh, R. Lucht, and W. Anderson. Comparative Experimental and Computational Evaluation of Combustion Dynamics Beahvior of a LDI Combustor. Combustion and Flame: *In Preparation*

Huang C., R. Gejji, W. Anderson, C. Yoon, V. Sankaran. Combustion Dynamic Behaviors in a Single-Element Lean Direct Injection (LDI) Gas Turbine Combustor. Combustion and Flame: *In Preparation*

Gejji, R., B. Austin and W. Anderson. Experimental Investigation of Transverse Combustion Instabilities in a High Pressure Multi-Element Combustor. 52nd AIAA/SAE/ASEE Joint Propulsion Conference, AIAA Propulsion and Energy Forum and Exposition 2016. Paper Accepted

Gejji, R., C. Huang, R. Lucht and W. Anderson (2015). Concurrent Experimental and Computational Study of Combustion Dynamics in a Single-Element Lean Direct Injection (LDI) Gas Turbine Combustor. 51st AIAA/SAE/ASEE Joint Propulsion Conference: 4227.

Gejji, R., C. Huang, C. Yoon and W. Anderson (2014). "A parametric study of combustion dynamics in a single-element lean direct injection (LDI) gas turbine combustor." 52nd Aerospace Sciences Meeting: 13-17.

Buschhagen, T., R. Z. Zhang, A. J. Bokhart, R. Gejji, S. V. Naik, R. P. Lucht, J. P. Gore, P. E. Sojka, C. D. Slabaugh and S. E. Meyer (2016). Effect of Aviation Fuel Type and Fuel Injection Conditions on Non-reacting Spray Characteristics of Hybrid Air Blast Fuel Injector. 54th AIAA Aerospace Sciences Meeting: 1154.

D'Entremont, J. H., R. Gejji, P. B. Venkatesh and S. P. Bane (2014). "Plasma control of combustion instability in a lean direct injection gas turbine combustor." Proc. 52nd Aerosp. Sci. Meeting: 2014-0622.

Huang, C., R. Gejji, W. E. Anderson and V. Sankaran (2014). Effects of Fuel Spray Modeling on Combustion Instability Predictions in a Single-Element Lean Direct Injection (LDI) Gas Turbine Combustor, 53rd AIAA Aerospace Sciences Meeting, AIAA SciTech.

Huang, C., R. Gejji, W. E. Anderson, C. Yoon and V. Sankaran (2014). Combustion Dynamics Behavior in a Single-Element Lean Direct Injection (LDI) Gas Turbine Combustor. 50th AIAA/ASME/SAE/ASEE Joint Propulsion Conference: 3433.

Huang, C., C. Yoon, R. Gejji, W. Anderson and V. Sankaran (2014). "Computational study of combustion dynamics in a single-element lean direct injection gas turbine combustor." 52nd Aerospace Sciences Meeting: 13-17.

Yoon, C., R. Gejji, W. Anderson and V. Sankaran (2013). "Effects of fuel spray modeling on the combustion dynamics of lean direct injection model combustor." ILASS-Americas 25th Annual Conference on Liquid Atomization and Spray Systems, Pittsburgh, PA.

Yoon, C., R. Gejji, W. E. Anderson and V. Sankaran (2013). Comprehensive Fuel Spray Modeling and Impacts on Chamber Acoustics in Combustion Dynamics Simulations, DTIC Document.

Yoon, C., R. Gejji, W. E. Anderson and V. Sankaran (2013). "Computational investigation of combustion dynamics in a lean direct injection gas turbine combustor." 51st Aerospace Sciences Meeting including the New Horizons Forum and Aerospace Exposition.

Yoon, C., C. Huang, R. Gejji, W. E. Anderson and V. Sankaran (2013). Computational investigation of combustion instabilities in a laboratory-scale ldi gas turbine engine. 49th AIAA/ASME/SAE/ASEE Joint PropulsionConference: 3648.